

# Technical Report

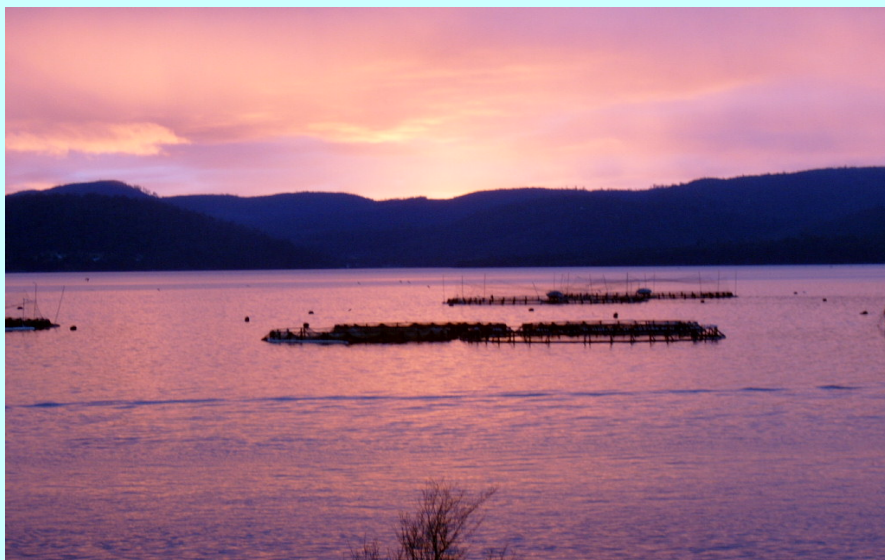


## **Numerical Hydrodynamic Modelling of the D'Entrecasteaux Channel and Huon Estuary**

Mike Herzfeld, John Parslow, Pavel Sakov and John Andrewartha  
CSIRO Marine and Atmospheric Research

*July 2005*

*Aquafin CRC Project 4.2  
(FRDC Project No. 2001/097)*



© Copyright Aquafin Cooperative Research Centre, Fisheries Research and Development Corporation,  
Commonwealth Scientific and Industrial Research Organisation

**This work is copyright. Except as permitted under the Copyright Act 1968 (Cth), no part of this publication may be reproduced by any process, electronic or otherwise, without the specific written permission of the copyright owners. Neither may information be stored electronically in any form whatsoever without such permission.**

**Every attempt has been made to provide accurate information in this document. However, no liability attaches to Aquafin CRC, its participant organisations or any other organisation or individual concerned with the supply of information or preparation of this document for any consequences of using the information contained in the document.**

*Published by CSIRO Marine and Atmospheric Research*



## Numerical Hydrodynamic Modelling of the D'Entrecasteaux Channel and Huon Estuary

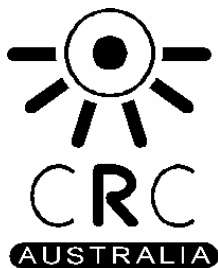
Mike Herzfeld, John Parslow, Pavel Sakov and John Andrewartha  
CSIRO Marine and Atmospheric Research

*July 2005*

*Aquafin CRC Project 4.2  
(FRDC Project No. 2001/097)*



**Australian Government**  
**Fisheries Research and  
Development Corporation**



## Contents

<b>1 Introduction.</b>	<b>5</b>
<b>2 The Hydrodynamic Model.</b>	<b>6</b>
<b>3 Model Domain.</b>	<b>8</b>
<b>4 Field Measurements</b>	<b>9</b>
<b>5 Input Data.</b>	<b>15</b>
<b>5.1 Wind Forcing.</b>	<b>15</b>
<b>5.2 Surface Elevation.</b>	<b>17</b>
<b>5.3 Temperature and Salinity.</b>	<b>19</b>
<b>5.4 River Flow.</b>	<b>21</b>
5.4.1 Huon River Flow	21
5.4.2 Derwent River Flow	21
<b>6 Modelling Strategy.</b>	<b>22</b>
<b>6.1 Local Domain Grid</b>	<b>22</b>
<b>6.2 Thermodynamic Effects</b>	<b>24</b>
<b>6.3 Nesting Procedure</b>	<b>30</b>
<b>7 Model Output.</b>	<b>34</b>
<b>7.1 Model Calibration</b>	<b>34</b>
<b>7.2 Sensitivity</b>	<b>367</b>
<b>7.3 General Model Solutions</b>	<b>41</b>
<b>7.4 Momentum Balance</b>	<b>44</b>
<b>7.5 Flushing Times</b>	<b>578</b>
<b>7.6 Residual Flow</b>	<b>76</b>
<b>7.7 Point Source Releases</b>	<b>80</b>
<b>7.8 Particle Tracking</b>	<b>88</b>
<b>7.9 Coarse Model</b>	<b>96</b>
<b>8. Conclusions</b>	<b>978</b>
<b>9. References</b>	<b>100</b>

# 1 Introduction

The D'Entrecasteaux Channel comprises the water body between the Tasmanian mainland and Bruny Island. The Huon Estuary joins the D'Entrecasteaux Channel near the southern limit of the channel, having fresh water input from the Huon River some 60 km upstream from the mouth of the estuary (Fig. 1). The Huon River is a significant source of fresh water where it enters the head of the Huon Estuary at Huonville. Saline water enters the Channel from the open ocean and propagates up the estuary as a salt wedge creating a classic salt wedge type estuary. These estuaries are characterised by high stratification and a stable water column; the water column only becoming well mixed during times of high flow when the salt wedge is pushed back downstream. The Huon/D'Entrecasteaux region is also characterised by complex geography, making modelling of the region challenging.

The Huon Estuary and D'Entrecasteaux Channel support a growing salmon aquaculture industry. Over the last decade there have been significant increases in aquaculture activity in the Estuary and Channel, raising concerns about the impact of these activities on the health of the ecosystem and ultimately the ecological sustainability of the industry. Specifically, information is needed regarding the number of farm sites that the estuary and channel can accommodate. The potential impact on the ecosystem is primarily that of eutrophication and low oxygen concentrations (which may ultimately lead to anoxia). Nutrients from fish farming enter the environment through direct release from the fish or degradation of detritus and uneaten feed pellets on the sea floor directly below aquaculture cages.

At the start of our project there was uncertainty as to whether the cumulative effect of nutrient sources due to aquaculture cages has an impact on the ecosystem overall. Furthermore, the stable water column, or relative lack of mixing, in the upper estuary means that bottom waters have no contact with overlying water and hence may become anoxic. This may have implications on nutrient release from the sediment and thus the nutrient cycling in the whole system. The presence of additional nutrient sources in bottom waters may complicate nutrient cycling in these regions.

In order to project trends in ecosystem health a series of numerical models were implemented to provide predictive capacity. These consisted of a hydrodynamic model to predict water transports, mixing regimes and temperature/salinity distributions and a biogeochemical model to predict primary productivity and nutrient cycling. This chapter outlines the development of the hydrodynamic model.

Long period simulations are required (>1 year) to assess the impact of aquaculture on the aquatic environment, and these simulations required acceptable run time ratios of greater than 100:1 (i.e. 100 model days in 1 day real time). The model was forced with river flow from various sources (the largest being the head of the Huon Estuary) wind stress and surface elevations, temperature & salinity on the northern and southern limits of the channel. These northern and southern boundary conditions were derived from a larger scale model of the region. The hydrodynamic model is introduced in 2 and the model grid

used described in 3. Data collected for calibration purposes is presented in 4 followed by presentation of data used to force the model in 5. Finally the modeling approach is described in 6, followed by presentation and analysis of model output in 7.

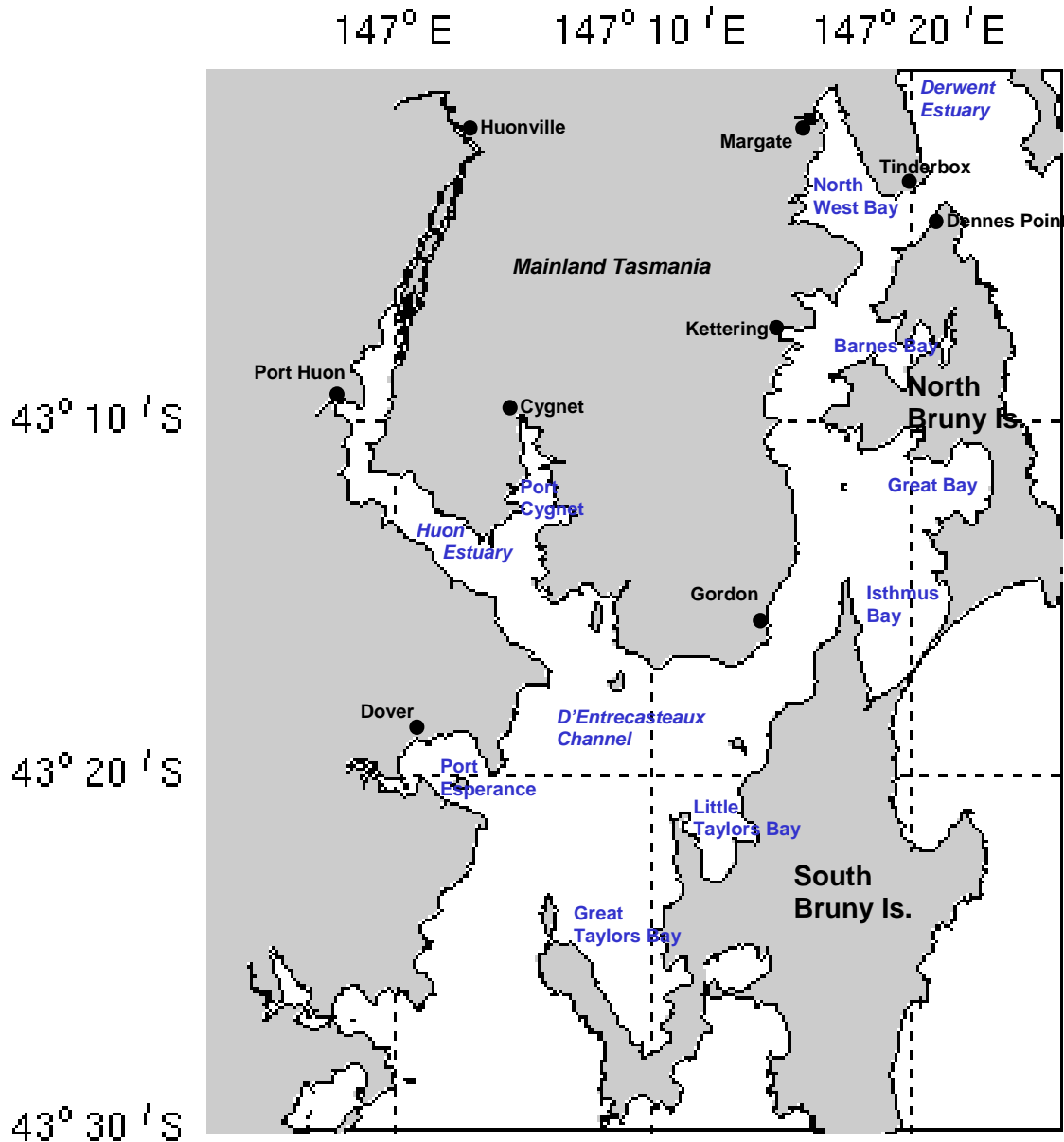


**Fig. 1. Geography of the D'Entrecasteaux Channel / Huon Estuary Region**

## 2 The Hydrodynamic Model

We used the MECO (Model for Estuaries and Coastal Ocean; Walker and Waring, 1998) hydrodynamic model to simulate the physics of the D'Entrecasteaux Channel and Huon Estuary. This model was developed by the Environmental Modelling group at CSIRO

Marine Research over the last decade. MECO is intended to be a general purpose model applicable to scales ranging from estuaries to regional ocean domains, and has been successfully applied to a variety of applications encompassing these scales to date. MECO is a three-dimensional finite difference hydrodynamic model based on the primitive equations. Outputs from the model include three-dimensional distributions of velocity, temperature, salinity, density, passive tracers, mixing coefficients and sea level. Inputs required by the model include forcing due to wind, atmospheric pressure gradients, surface heat and water fluxes and open boundary conditions (e.g. tides). MECO is based on the three dimensional equations of momentum, continuity and conservation of heat and salt, employing the hydrostatic and Boussinesq assumptions. The equations of motion are discretised on a finite difference stencil corresponding to the Arakawa C grid.

The model uses a curvilinear orthogonal grid in the horizontal and a choice of fixed 'z' coordinates or terrain-following  $\sigma$  coordinates in the vertical. The curvilinear horizontal grid was particularly useful in this application since it enabled high resolution to be specified in areas of the study region where small scale motions were present and larger resolution where they were not. The 'z' vertical system allows for wetting and drying of surface cells, which is useful for resolving the surface layer in the presence of moderate tides. MECO has a free surface and uses mode splitting to separate the two dimensional (2D) mode from the three dimensional (3D) mode. This allows fast moving gravity waves to be solved independently from the slower moving internal waves allowing the 2D and 3D modes to operate on different time-steps, resulting in a considerable contribution to computational efficiency. Computation efficiency was an important issue in this study into which considerable effort was devoted, since long period simulations were to be attempted (greater than one year). The model uses explicit time-stepping throughout except for the vertical diffusion scheme which is implicit. This implicit scheme guarantees unconditional stability in regions of high vertical resolution. A Laplacian diffusion scheme is employed in the horizontal on geopotential surfaces. Smagorinsky mixing coefficients may be utilised in the horizontal.

MECO can invoke several turbulence closure schemes, including k- $\epsilon$ , Mellor-Yamada 2.0 and Csanady type parameterisations. A variety of advection schemes may be used on tracers and 1<sup>st</sup> or 2<sup>nd</sup> order can be used for momentum. This study used the QUICKEST advection scheme for tracers (Leonard, 1979) in conjunction with the ULTIMATE limiter (Leonard, 1991). This scheme is characterised by very low numerical diffusion and dispersion, and yielded excellent performance when resolving frontal features, which often occurred in the salinity distribution during times of high flow of the Huon River. MECO also contains a suite of radiation, extrapolation, sponge and direct data forcing open boundary conditions. Input and output is handled through netCDF data formatted files, with the option of submitting ascii text files for simple time-series forcing. The netCDF format allows input of spatially and temporally varying forcing and initialization data in a grid and time-step independent manner. MECO is capable of performing particle tracking and may be directly coupled to ecological and sediment transport models.

### 3 Model Domain

A common problem encountered when modelling water bodies is the accurate prescription of data along any open boundaries. Open boundaries are the limits of the domain beyond which no information is available for the model, and hence for which data must be explicitly supplied. In the absence of field-derived temperature, salinity and surface elevation measurements to apply to the open boundaries, a common solution to this problem is the practice of successive nesting, where small scale models are nested within larger scale models until the region of interest can be adequately resolved. The simulation of the physics of the D'Entrecasteaux Channel and Huon Estuary required the construction of three nested model grids. A large scale regional grid was made which acted to supply the initial and open boundary conditions for an intermediate scale grid, which in turn supplied boundary forcing for the local grid of the study region. The regional domain is illustrated in Fig. 2 and the nested domain in Fig. 3. The nesting procedure is discussed in more detail in 6.3.

Note that the bathymetries are included in these Figures, which show that the channel domain is relatively shallow, with maximum depths less than 60 m. The Huon Estuary is generally less than half this depth, with a narrow channel creating a connection between the estuary mouth and the main body of the channel. Also, the regional domain includes three open boundaries; two cross-shore and one offshore beyond the shelf break. The channel domain only uses two open boundaries at the northern and southern limits of Bruny Island.

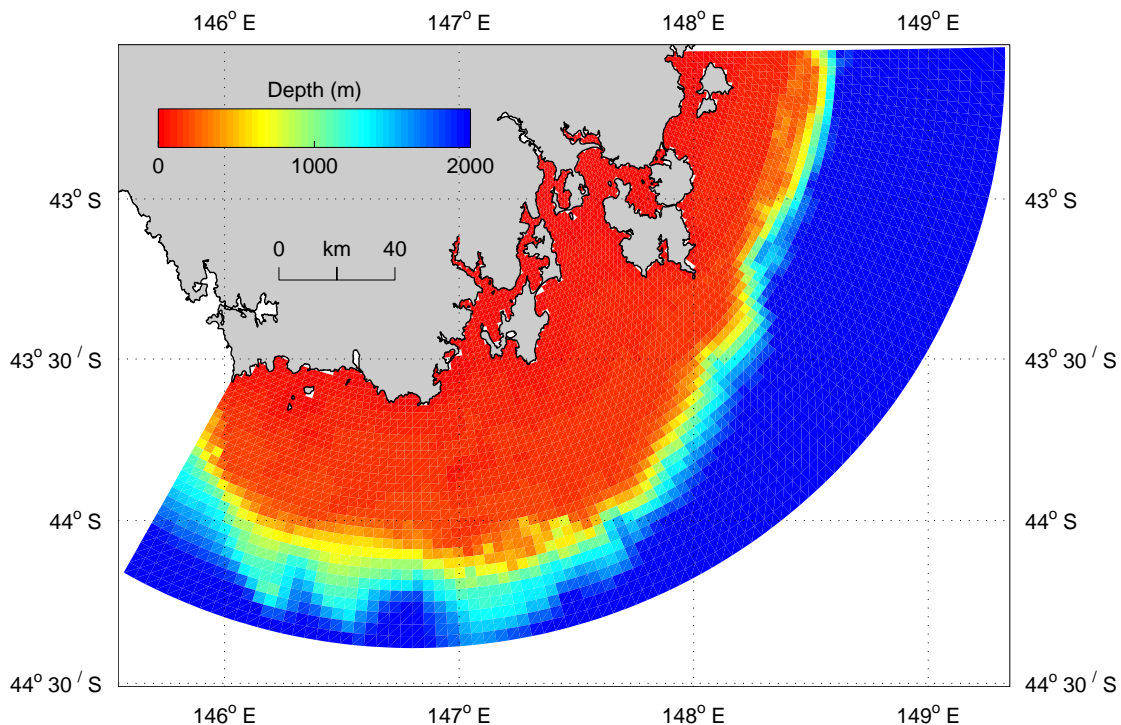


**Fig. 2. Regional Model Domain**

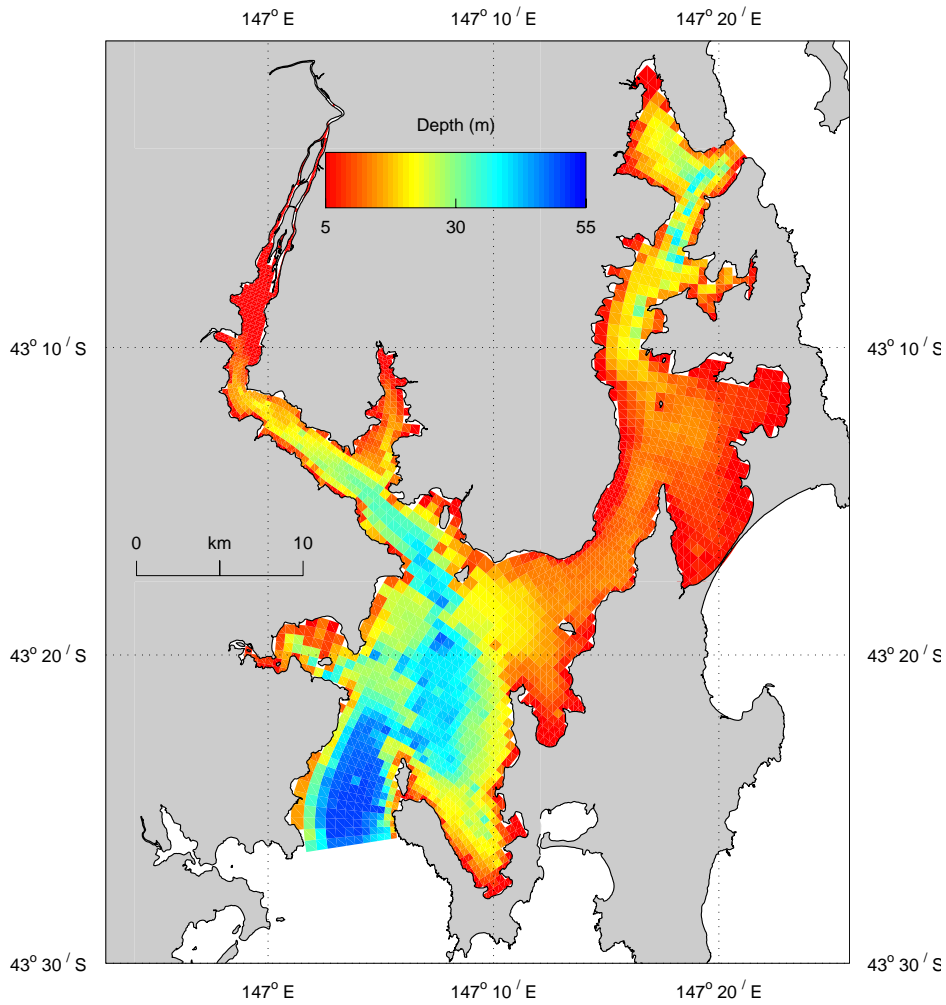


**Fig. 3. The Huon/D'Entrecasteaux Domain**

## 4 Field Measurements

Included in the Environment Program of the Aquafin CRC was a Broad-Scale Monitoring Program. This program collected temperature, salinity, nutrients and phytoplankton samples on a monthly basis from throughout 2002 along a transect down the D'Entrecasteaux Channel and at specific sites in the side bays. Numbered CTD sampling sites in the D'Entrecasteaux Channel relevant to this study are depicted in Fig. 4. Temperature and salinity sections interpolated from data collected at these sites are displayed in Figs 5 to 13. Both the downcast and upcast of the CTD cast were measured, but only the downcast is displayed since it is more reliable due to the steady sinking rate and undisturbed surrounding water.

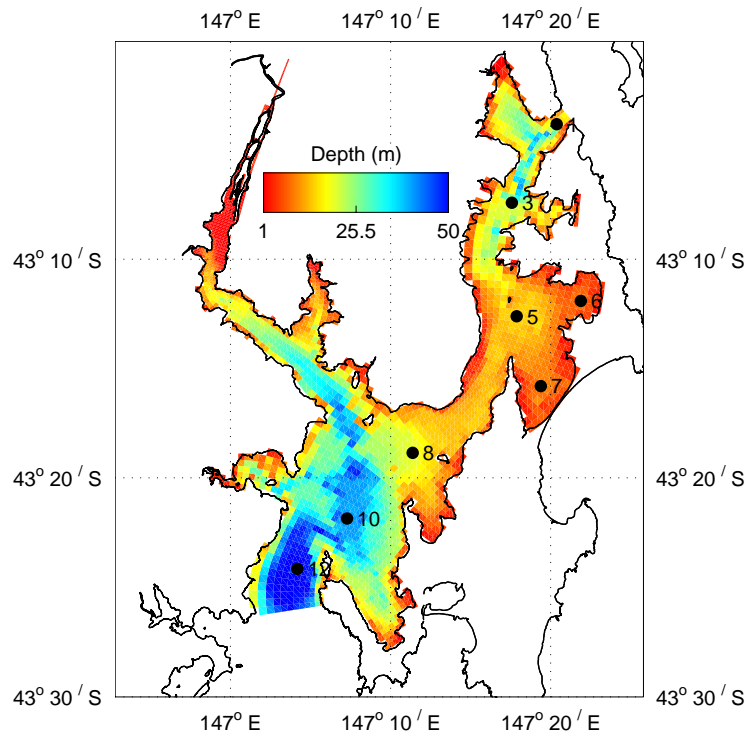


**Fig. 4. D'Entrecasteaux Channel station locations.**

**Fig. 2.5: OBSERVED (downcast) 10 Jan 2002**

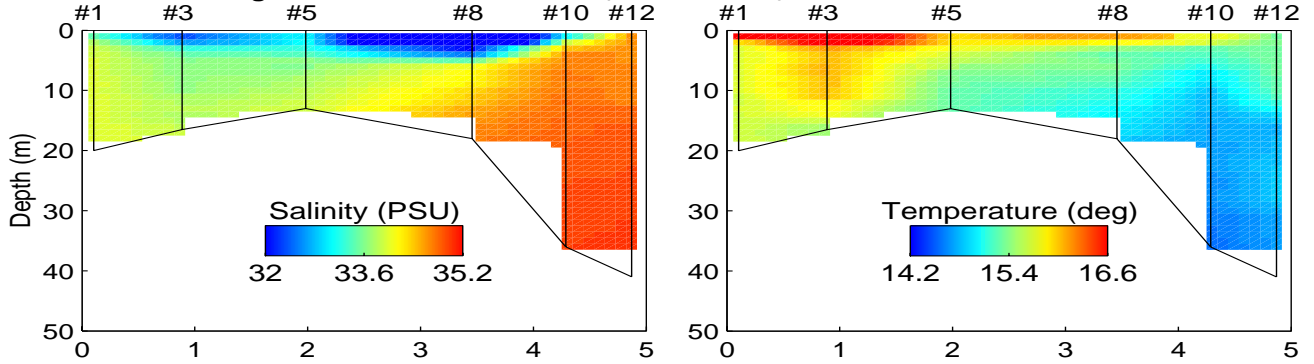


**Fig. 4.6: OBSERVED (downcast) 06 Feb 2002**

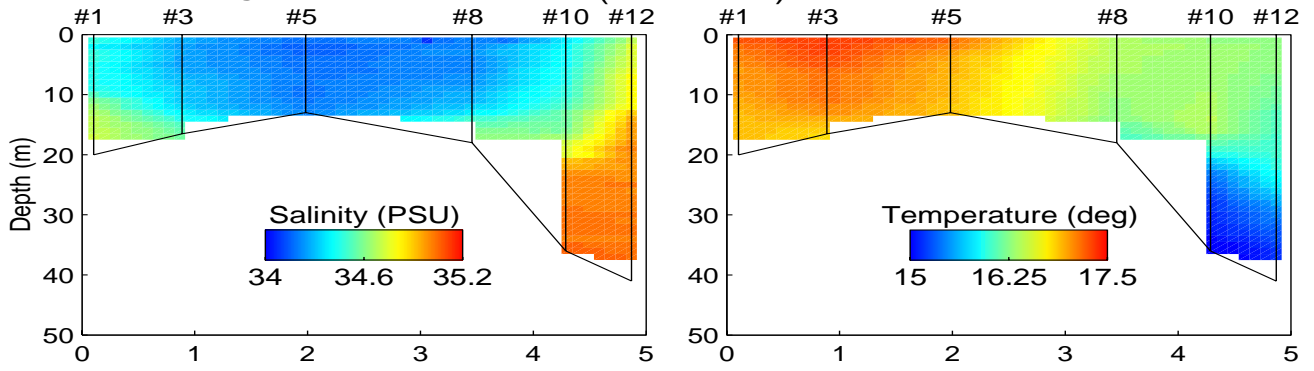


**Fig. 2.7: OBSERVED (downcast) 04 Mar 2002**

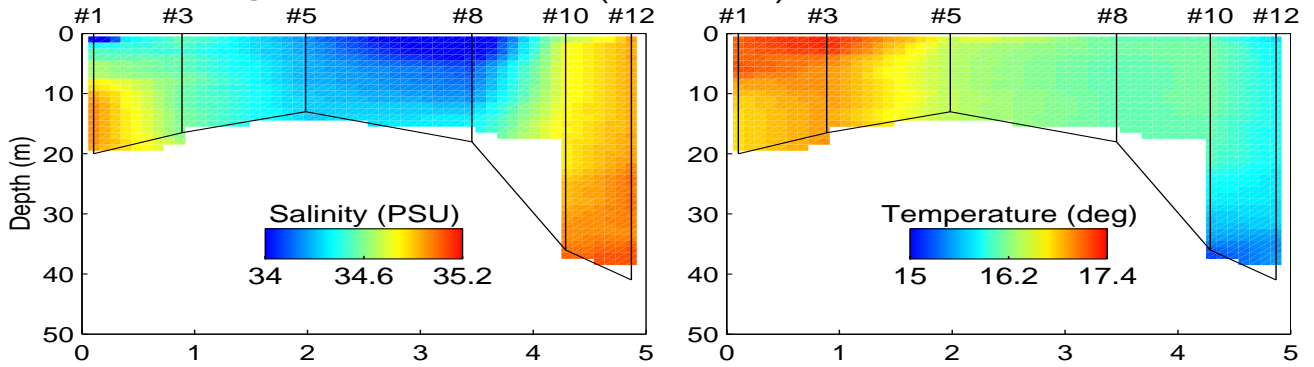


**Fig. 2.8: OBSERVED (downcast) 05 Apr 2002**

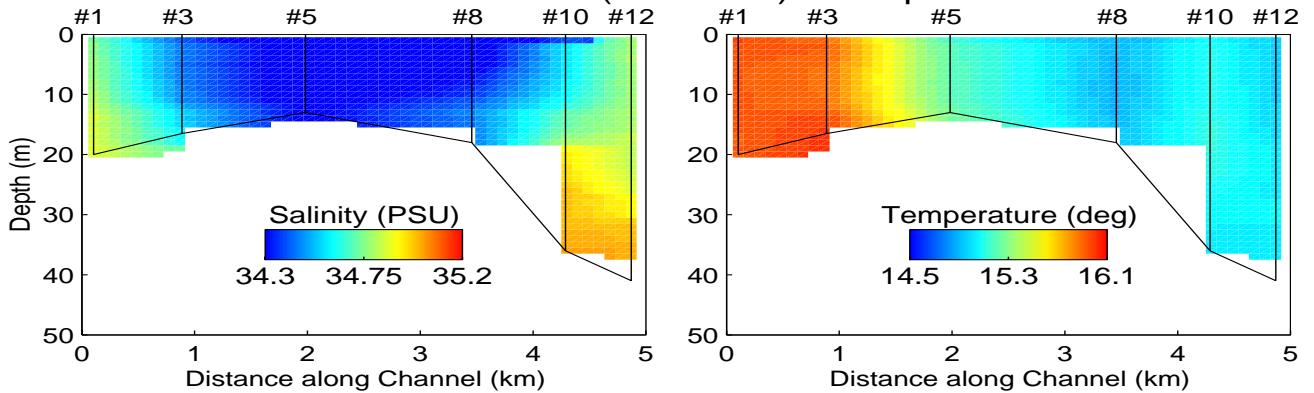


**Fig. 2.9: OBSERVED (downcast) 29 Apr 2002**

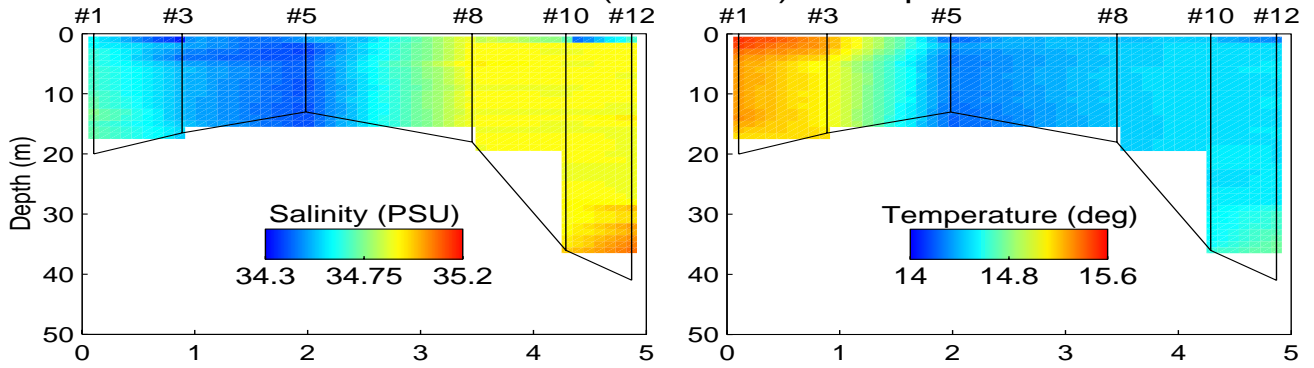


**Fig. 2.10: OBSERVED (downcast) 03 Jun 2002**

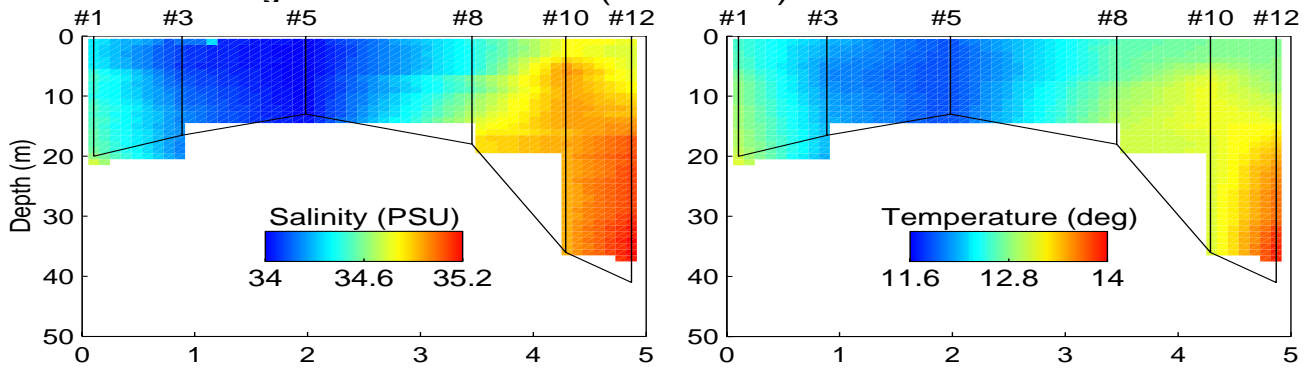


**Fig. 2.11: OBSERVED (downcast) 03 Jul 2002**

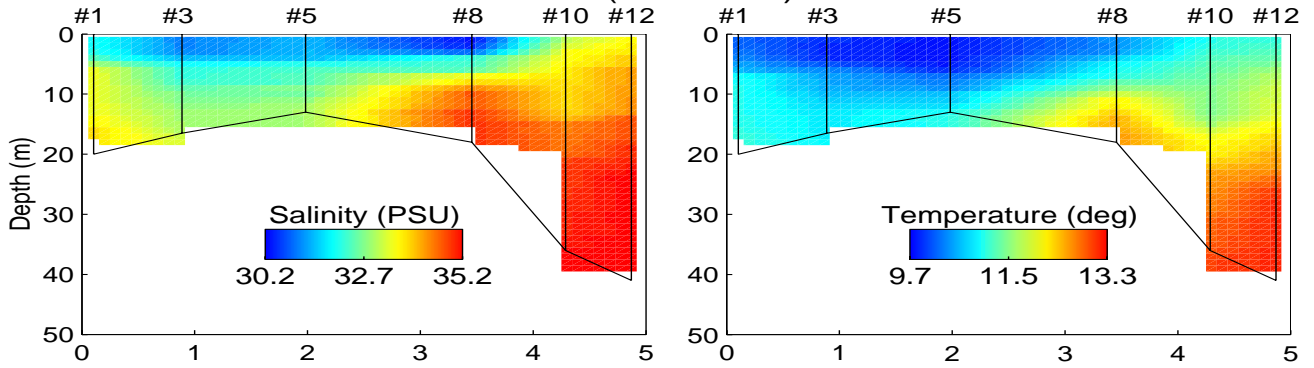


**Fig. 2.12: OBSERVED (downcast) 05 Aug 2002**

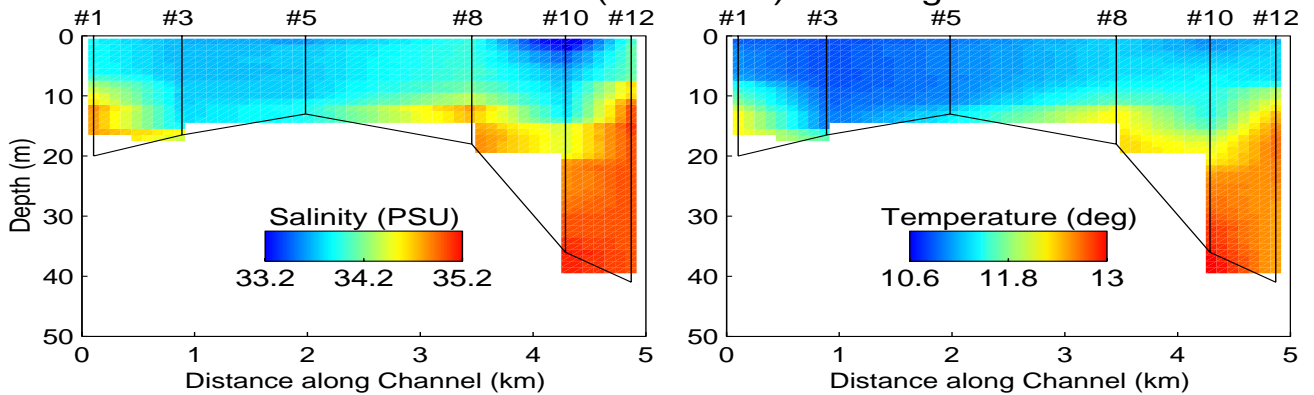


**Fig. 2.13: OBSERVED (downcast) 02 Sep 2002**

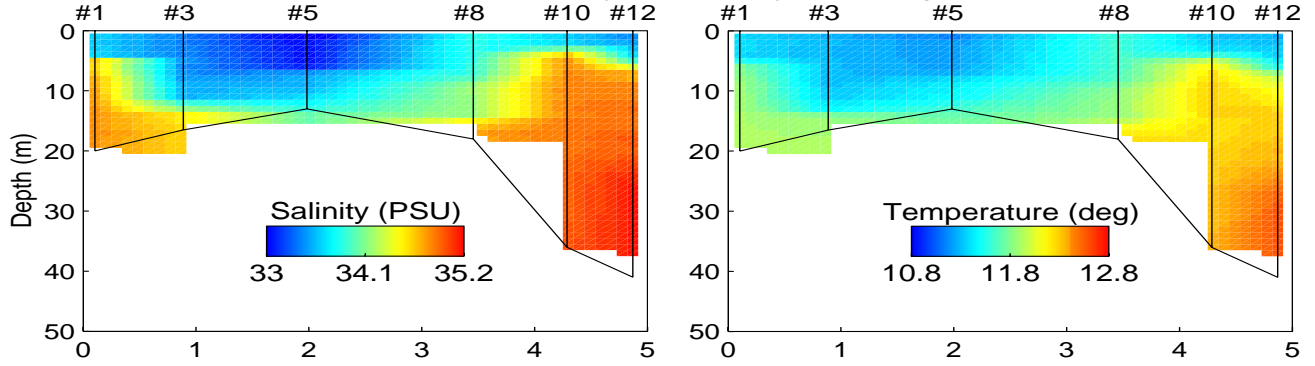


**Fig. 2.14: OBSERVED (downcast) 30 Sep 2002**

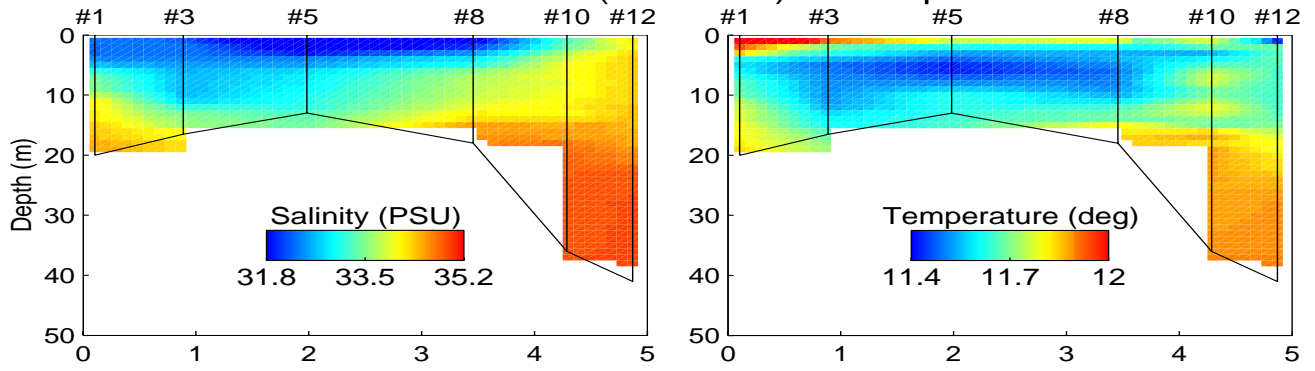


**Fig. 2.15: OBSERVED (downcast) 04 Nov 2002**

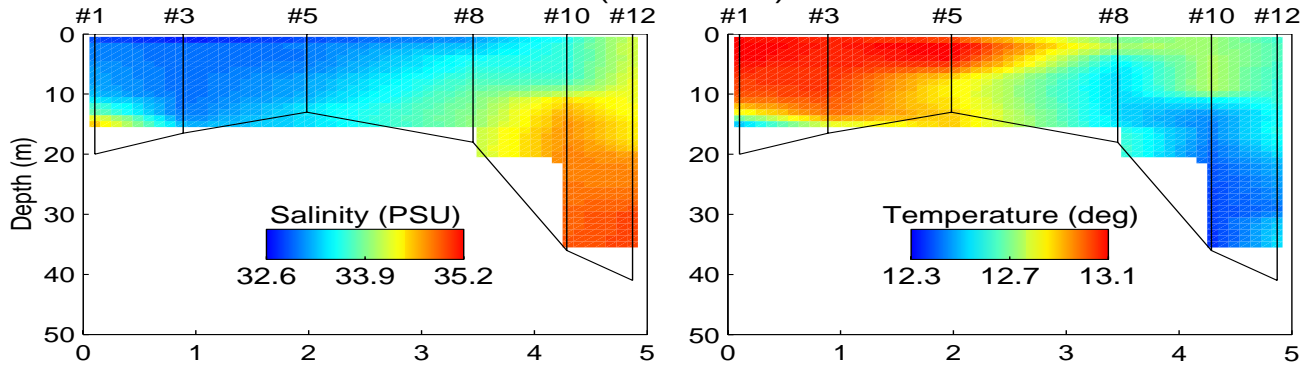
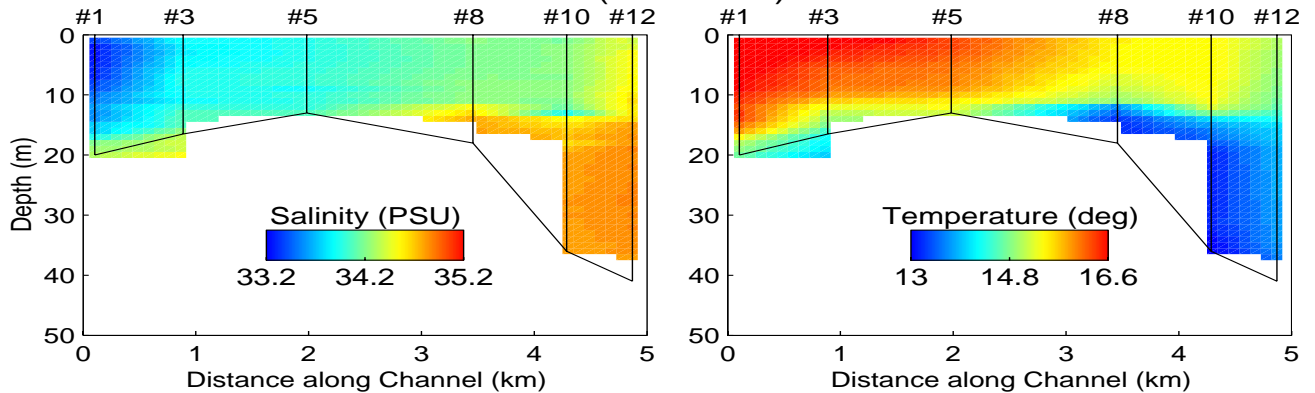


**Fig. 2.16: OBSERVED (downcast) 02 Dec 2002**



These data show that a gradient in temperature (up to 1°C) exists down the D'Entrecasteaux Channel during summer and autumn, with the northern end associated with higher temperature. The deeper waters at the southern end have the lowest temperature in the channel, presumably due to the sub-thermocline oceanic influence. Towards autumn this vertical gradient at the southern end is less pronounced as surface cooling decreases surface temperature heading into winter. In winter bottom waters become warmer than surface waters, but still several degrees cooler than the summer bottom temperature. This bottom temperature increase in winter is also observed at the northern end of the channel. On 10 January 2001, a warm surface layer was particularly pronounced and shallow, and is associated with a thin layer of fresher water attributed to the influence of Huon River outflow. The flow data indicates that a large flow of 883 m<sup>3</sup>s<sup>-1</sup> occurred on 8 Jan 2001, thus the measurements taken on 10 Jan 2001 certainly captures this event. Generally, salinity is lower in the mid-channel region and attains the highest values in bottom waters at the ends of the channel throughout the year, thus density compensating the temperature distribution. Thin fresh water layers can also be observed mid-channel during times of high Huon River flow.

Additional data was collected in the North West Bay region independently by TAFI (Tasmanian Aquaculture and Fisheries Institute). These data consisted of CTD and nutrient samples collected at specific sites and ADCP data from specific sites (courtesy of Dr Alan Jordan, TAFI) and covered the period Nov 2001 to Feb 2002. The North West Bay sampling are displayed in Fig. 17.

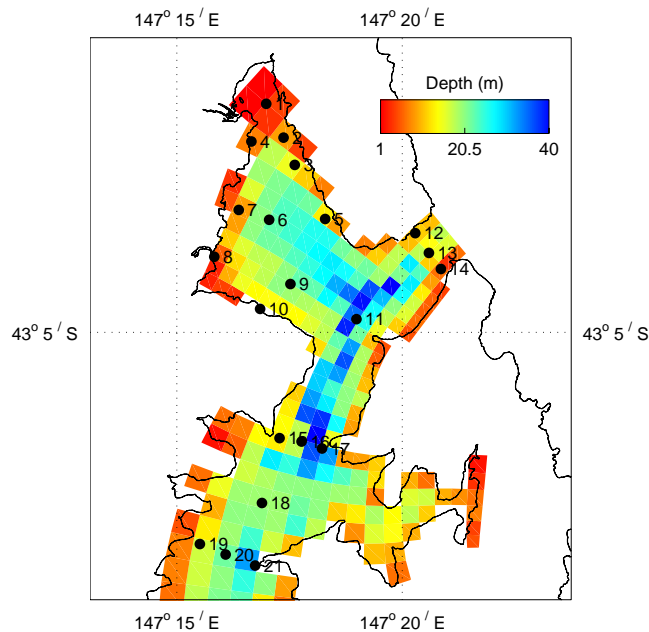


**Fig. 17. North West Bay Sites as sampled by TAFI**

The temperature and salinity data collected from field programs can be used for both model initialisation and forcing through the open boundaries as well as model calibration.

Additionally, these data provide useful insight into the thermodynamics and exchange processes occurring in the Huon / D'Entrecasteaux, which are discussed in Section 6.

## 5 Input Data

The model was forced with wind, river flow from the Huon River and elevation, temperature and salinity at the two oceanic open boundaries. The sources of these forcings are detailed below.

### 5.1 Wind Forcing

Wind speed and direction data were obtained from the Bureau of Meteorology (BOM, except for \* = CSIRO) at the following locations and interpolated onto the regional and D'Entrecasteaux / Huon domains to provide a temporally and spatially varying wind-field. Wind measurement sites are summarised in Table 1 and Fig. 18.

**Table 1. Wind Measurement Sites**

Site	Latitude (deg S)	Longitude (deg E)
Hobart Airport	42.8389	147.4992
Palmer's Lookout	43.1650	147.8317
Cape Bruny	43.4903	147.1447
Maatsuyker Island	43.6578	146.2711
Droughty Hill*	42.9256	147.4206

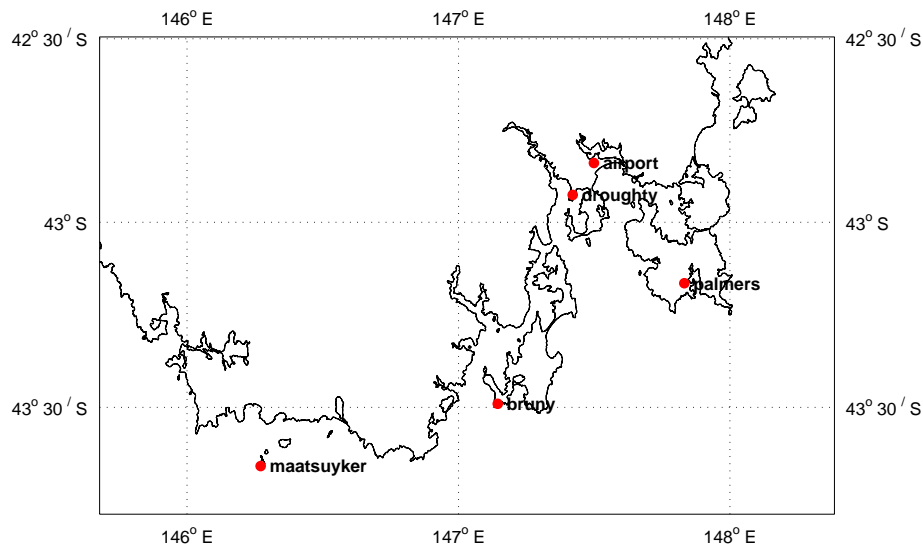


**Fig. 18. Wind measurement sites**

A sample of the wind-field at these sites is shown in Fig. 19 (a) and (b) for the year 2002. The mean for this period is a southerly with speed of  $4.3 \text{ ms}^{-1}$ .

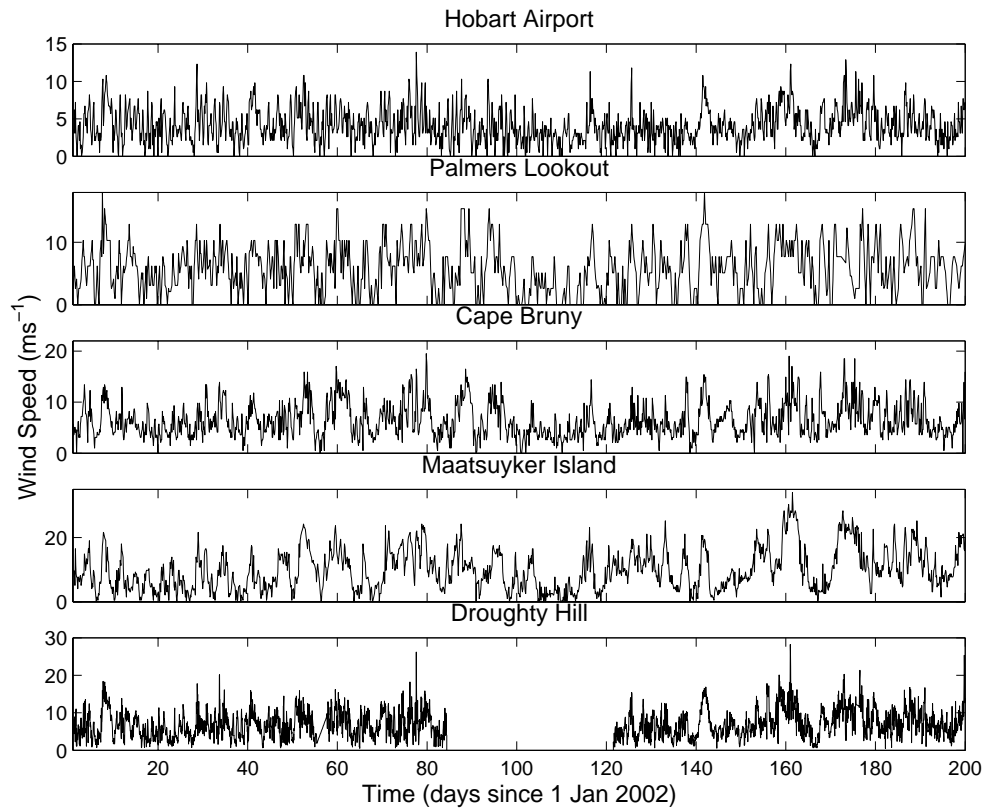


**Fig. 19 (a). Wind Speed at Measurement Sites**

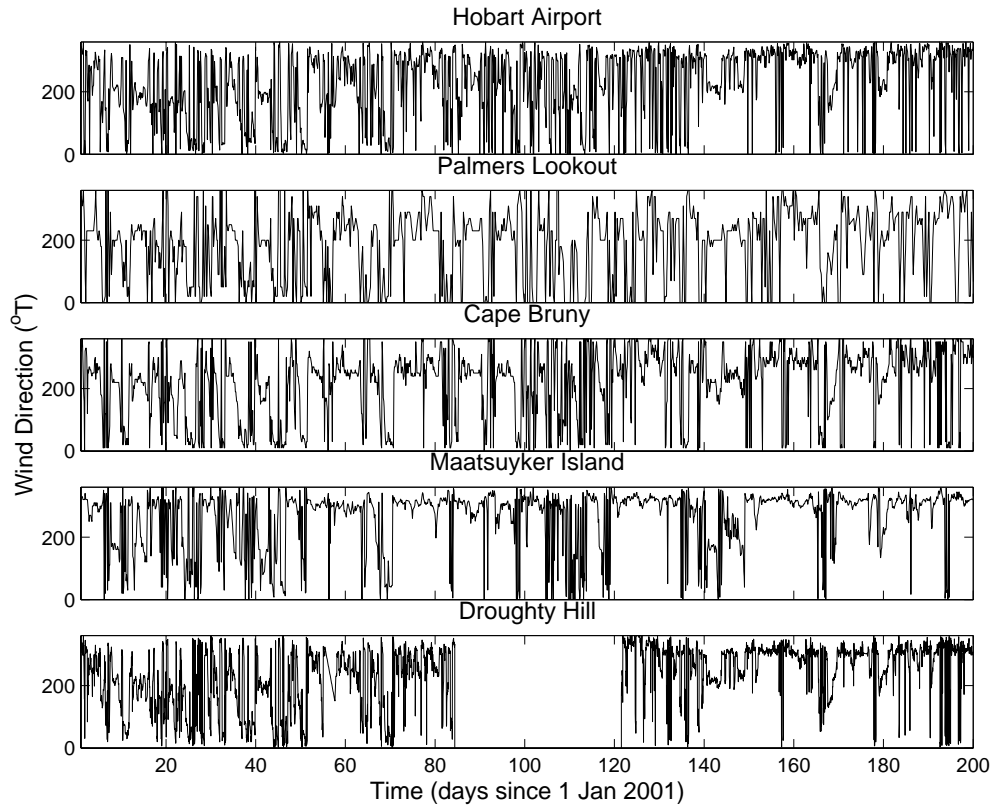


**Fig. 19 (b): Wind Direction at Measurement Sites**

## 5.2 Surface Elevation

The surface elevation for the Huon/D’Entrecasteaux domain was supplied from output of the regional model. The elevations used in the region model consist of a high frequency component (tidal component with frequencies  $< 1$  day) and a long period component with frequencies of days to weeks. The tidal component applicable to the regional domain was constructed from a global tidal model (Cartwright and Ray, 1990). This global model did not perform well in the vicinity of the north-eastern cross-shelf boundary, so a yet larger domain was created to encompass the regional grid upon which the model was run in barotropic (2-D) mode only to yield time series of surface elevation on this boundary. These time series were then decomposed into the tidal constituents, which were subsequently used to force the tidal component in the regional model. This approach provided better results than directly imposing the global tidal model constituents on the north-eastern boundary. The tidal constituents are presented in Table 5.2 with the ranges of amplitude encountered. Note that these constituent’s amplitude and phase vary spatially around the open boundary perimeter.

The long period component was extracted from low passed elevation records collected at Port Arthur on the Tasman Peninsula (courtesy of Dr John Hunter, University of

Tasmania) and Spring Bay on the east coast (from National Tidal Facility). The Port Arthur signal was lead by 0.5 days and applied at the western open boundary of the regional model with no change in amplitude. The Spring Bay long period component was applied directly to north-eastern boundary. These long period components are applicable to the coast only, and an offshore profile was imposed on the amplitude to correctly specify the long period wave over the shelf. The resulting modelled surface elevations were compared to those measured at Hobart to validate the forcing, as illustrated in Fig. 20.

**Table 2. Tidal Harmonics for the Regional Model**

Name	Western Boundary	Offshore Boundary	NE Boundary
	Amplitude (m)	Amplitude (m)	Amplitude (m)
Q1	0.028 - 0.029	0.022 – 0.028	0.022
O1	0.119 - 0.125	0.099 – 0.119	0.099 - .113
P1	0.054 - 0.058	0.049 – 0.054	0.049 – 0.058
S1	0.001	0.001	0.001 – 0.002
K1	0.165 - 0.176	0.150 – 0.165	0.151 – 0.172
2N2	0.008 - 0.010	0.008 - 0.014	0.014
MU2	0.009 - 0.011	0.009 - 0.016	0.017
N2	0.031 - 0.034	0.031 - 0.083	0.085
NU2	0.005 - 0.006	0.005 - 0.015	0.016
M2	0.119 - 0.120	0.119 - 0.325	0.330 – 0.332
L2	0.003 - 0.004	0.003 - 0.006	0.006
T2	0.004 - 0.005	0.003 – 0.004	0.002 – 0.003
S2	0.074 - 0.087	0.038 – 0.074	0.035 – 0.039
K2	0.022 - 0.026	0.008 – 0.022	0.008

The elevations provided by the regional model were then used in the higher resolution nested grids. Obviously these elevation signals contained both the diurnal and long period fluctuations.

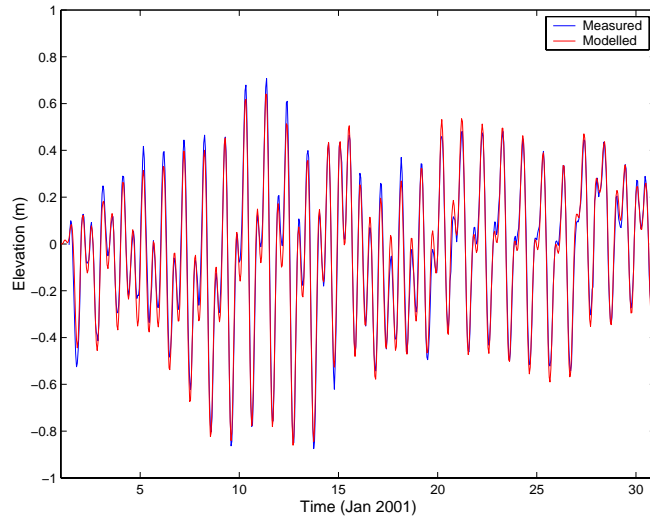


**Fig. 20. Segment of Surface Elevation at Hobart.**

### 5.3 Temperature and Salinity

The temperature and salinity distribution in the regional model was initialised with annual mean distributions provided by the CARS atlas (Climatological Atlas of Regional Seas, Ridgway et al 2002). These data provide a mean annual cycle of temperature and salinity output at 10 day intervals on a 1/8 degree grid. The open boundaries of the regional domain were also forced with the CARS climatology. The CARS data did not perform well in the inshore regions, presumably due to lack of data in the assimilation procedure. Temperature was too low in these regions, and salinity was typically too high. The lack of data in the compilation of CARS in the inshore region probably omitted signatures of important sources of heat (e.g. local atmospheric heat fluxes) and fresh water (river flows) which contributed to these inconsistencies. For this reason it was decided not to use output from the regional model to initialise and force the local Huon / D'Entrecasteaux domain on the open boundaries.

Although the data collected from the broad-scale field program is temporally and spatially coarse, these data could be interpolated onto the grid to provide initial conditions and interpolated temporally to provide open boundary conditions that were better than output from the regional model. The temperature and salinity distribution in the local domain on 10 January 2002 as derived from the field program and output from the regional model are presented in Figs 21 and 22. The regional model is relaxed to CARS on a time scale of 10 days so as to provide a pseudo seasonal forcing. It can be seen that the regional model is significantly cooler and saltier than the field derived measurements. Again, there exist no local heat and salt sources in the CARS relaxed solutions, leading to these inaccuracies

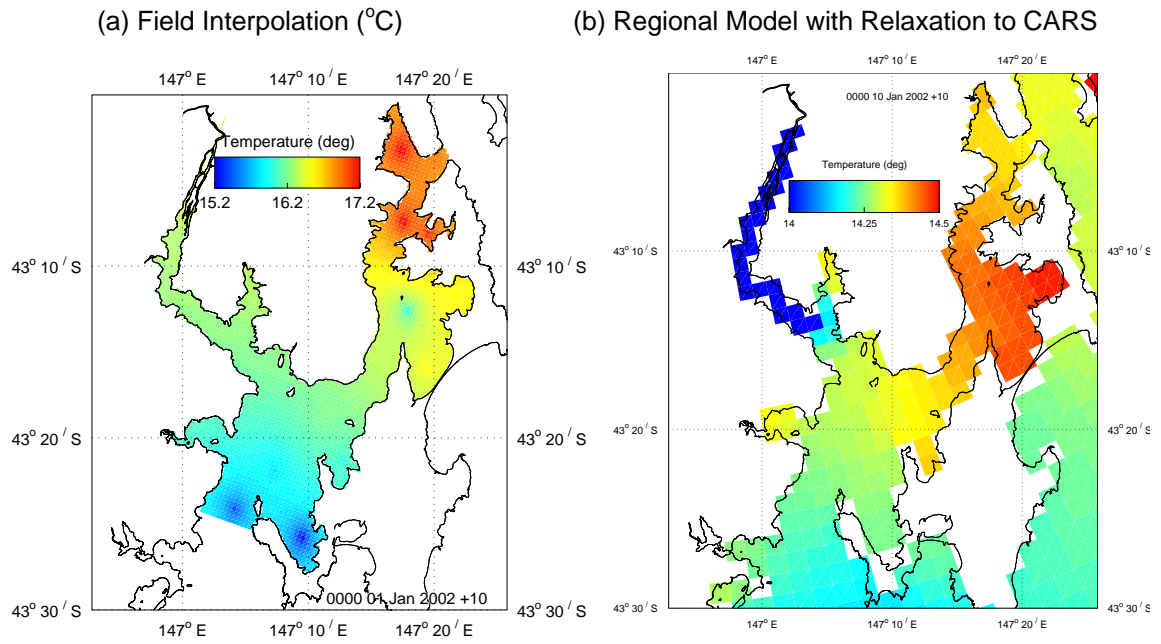


**Fig. 21. Temperature Distribution at 10 Jan 2002**

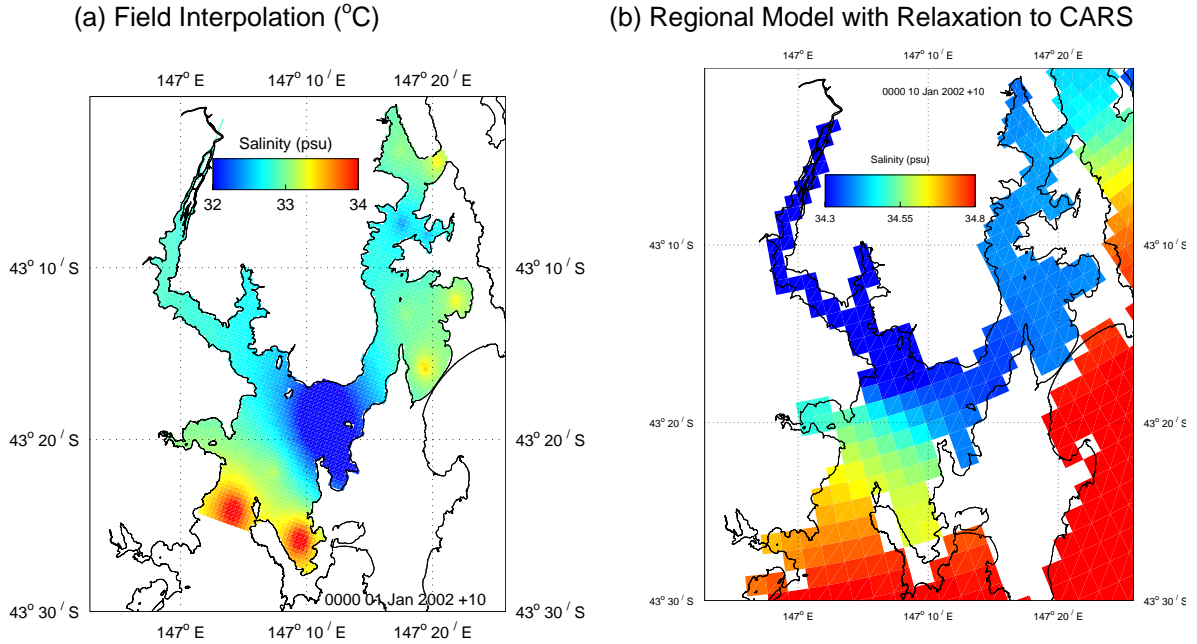


**Fig. 22. Salinity Distribution at 10 Jan 2002**

## 5.4 River Flow

### 5.4.1 Huon River Flow

Flow from the Huon River was input directly into the model as an open boundary condition. River flow records were obtained at Frying Pan Creek, upstream from the riverine input open boundary in the Huon/D'Entrecasteaux domain (courtesy of DPIWE). This flow record was multiplied by a scaling factor of 1.2 to allow for catchment area contributing to flow below Frying Pan Creek, resulting in flow applicable to Huonville. Time series of this flow is presented in Fig. 23, from which it is observed that several large flood events occurred in 2002, primarily in the winter and spring months. The largest flow of close to 1000 cumecs occurred on 13 Aug. The salinity of the Huon inflow is assumed to be fresh (i.e. 0 psu) and the temperature was obtained from measurement (DPIWE). River temperature is illustrated in Fig. 23.

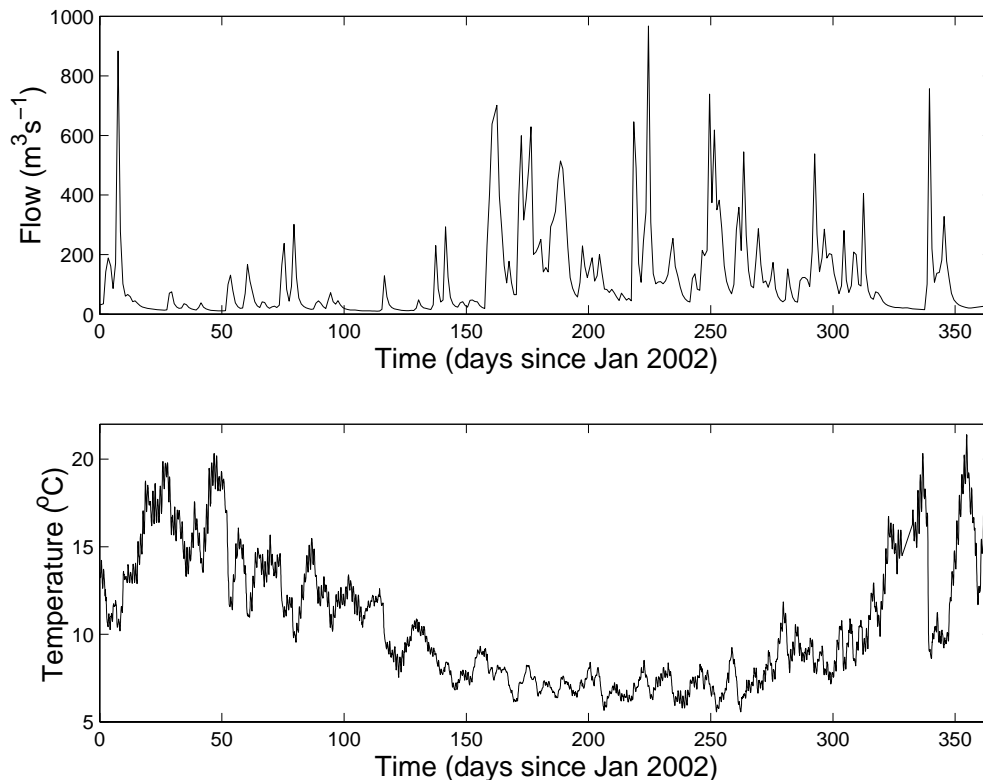


**Fig. 23. River Characteristics at Huonville**

### 5.4.2 Derwent River Flow

Derwent River flow was input as boundary conditions to the larger scale models within which the local domain was nested. Daily flow was obtained from the Tasmanian Hydro below Meadowbank and hourly data from DPIWE of the Tyenna flow. These flows were combined and used as the river flow at New Norfolk. River temperature was unavailable and the low passed air temperature at Hobart airport was assumed to be representative of

the river temperature at New Norfolk. River flow and temperature are displayed in Fig. 24.

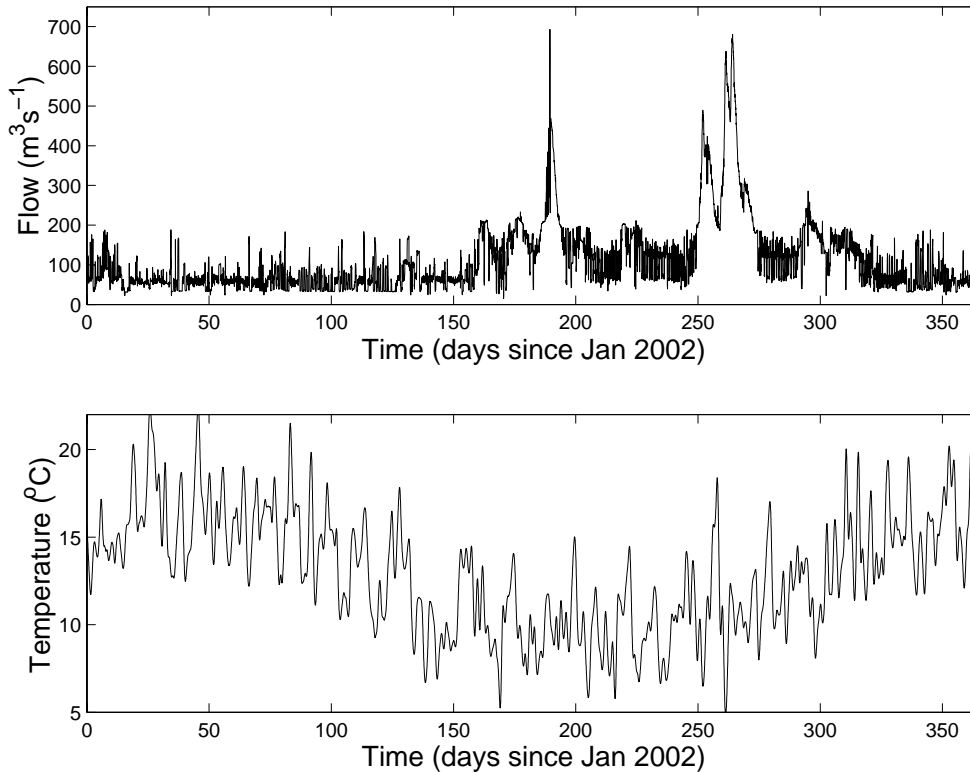


**Fig. 24. River Characteristics at New Norfolk**

## 6 Modelling Strategy

The objective of running the hydrodynamic model is to provide insight into the physics governing the Huon Estuary/D'Entrecasteaux Channel system and provide transports and the mixing regime for the biogeochemical model. Output is generated for the period Jan 2002 to Aug 2002 using the forcing data described in Section 5, which may then be calibrated and validated against data collected during the field programs from Dec 2001 to May 2002.

### 6.1 Local Domain Grid

A common challenge faced in developing a hydrodynamic grid is to maintain sufficient spatial resolution in the domain without sacrificing accuracy by under-resolving certain scales of motion. Basically, the greater the resolution the longer the model takes to execute, which often places prohibitive restrictions on the length of a simulation. The objective is to create a model that executes at a run-time ratio of at least 100:1 (i.e. 100 model days for each day of real time) allowing one year of simulation in under 4 days real time. There exists stability criterion the model is subject to which place restrictions on the time-stepping used, e.g. basically any wave or current in the model cannot traverse more than one grid cell in one time-step. Among other things this is dependent on the

water depth, degree of stratification and the grid cell size. Obviously it is only the latter that control may be exerted over when building a grid, and an iterative process is usually employed to obtain an optimum grid that balances resolution with computational pressures.

This iterative process involves performing simulations on a given grid with a conservative time-step. The theoretical upper limit for the time-step is then computed at every grid node and at every time-step, allowing the minimum over the simulation to be obtained and areas in the grid susceptible to restrictive time-steps identified. The resolution in these areas could then be increased, and the process repeated. The optimized grid resulting from this process is displayed in Fig. 25.

The grid resolution in this domain ranged from a minimum of 150 m in the Huon Estuary to a maximum of 700 m near the southern boundary. The model uses 26 layers in the vertical. There exist 13000 surface cells total in this grid, only 1800 (13%) of which are wet; i.e. the majority of this grid is associated with dry land which can also lead to computational inefficiencies. Using this grid, time steps of 60 and 5 seconds were used for the 3D and 2D components of the model respectively, yielding a run time ratio of greater than 100:1 which allowed long term simulations to be performed (e.g. 1 year simulations in approximately 3 days real time) .

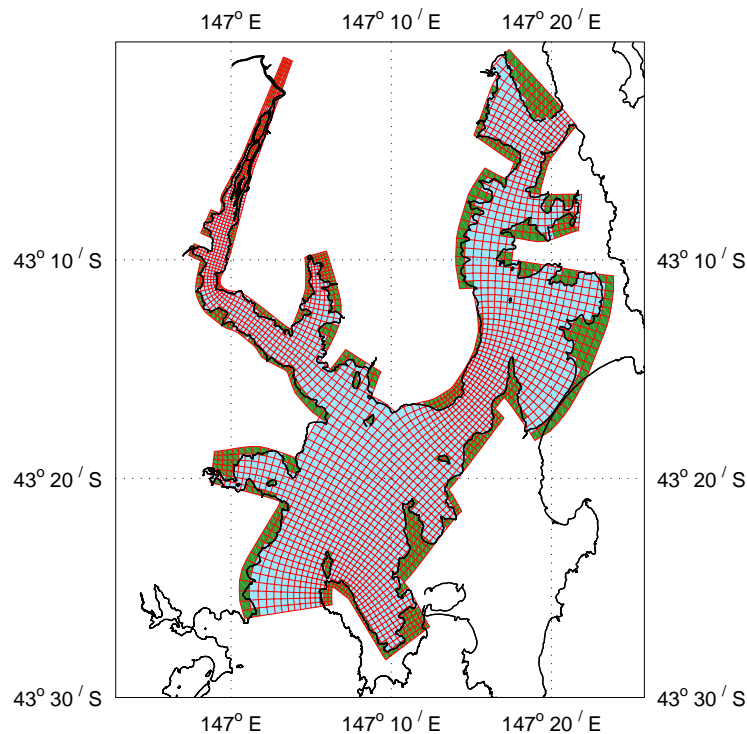


**Fig. 25. Model Discretization**

## 6.2 Thermodynamic Effects

The sea surface temperature and salinity at the sites in Fig. 4 and 10 are displayed in Table 3 and 4 respectively.

**Table 3. Sea Surface Temperature (°C) and Salinity (psu) in the D'Entrecasteaux Channel. Measurements are quoted from the downcast at depths <1 m.**

Date	Station 1		Station 3		Station 5		Station 8		Station 10		Station 12	
	T	S	T	S	T	S	T	S	T	S	T	S
10/01	16.9	33.43	17.3	32.27	15.9	33.04	16.2	29.13	15.8	33.14	15.3	34.63
06/02	17.3	34.47	17.3	34.26	17.2	34.10	16.4	34.17	16.3	34.40	16.3	34.65
04/03	17.1	34.27	17.2	34.63	16.6	34.29	16.0	33.84	16.1	34.78	15.8	34.92
05/04	15.9	34.73	15.9	34.46	15.2	34.19	14.9	34.13	15.1	34.56	14.9	34.76
29/04	15.3	34.70	15.2	34.43	14.4	34.39	14.4	34.89	14.4	34.27	14.1	34.69
03/06	12.6	34.37	12.1	34.10	11.9	34.06	12.7	34.43	12.8	34.77	12.8	34.73
03/07	10.2	31.87	9.9	31.03	9.8	31.42	10.4	30.38	11.1	33.10	11.1	33.56
05/08	11.0	33.84	10.8	33.69	11.0	33.69	11.2	34.00	11.1	33.10	9.6	33.24

**Table 4. Sea Surface Temperature (°C) and Salinity (psu) in the northern D'Entrecasteaux Channel. Measurements are quoted from the upcast at depths < 1m.**

Date	Station 13		Station 11		Station 16		Station 18		Station 20	
	T	S	T	S	T	S	T	S	T	S
13/11/01	14.3	41.40	14.3	41.64	14.3	41.17	14.4	35.65	14.5	
05/12/01	15.6	32.59							15.3	32.46
17/12/01	15.4	32.68			15.8	32.36	15.6	32.72	15.7	32.75
10/01/02	16.7	32.91	16.6	31.29	16.9	32.26	16.9	32.01	16.8	32.25
23/01/02	18.5	32.93	19.1	33.06					18.7	33.11
15/02/02	17.8	34.07								

These data indicate that the Channel generally becomes warmer and slightly saltier over summer, and then tends to a cooler, fresher state in autumn. The temperature solutions resulting from the model forcing and initialisation described in Section 5 indicate that boundary forcing alone cannot input sufficient heat to raise temperatures to those observed in summer. Fig. 26 shows the measured and modelled temperature at all

stations. It is observed that the SST at all stations is underestimated in summer when the observed temperature increases, and warmer in autumn when the system cools and observed temperature decreases. The discrepancy in temperature between modelled and measured can be over 1°C.

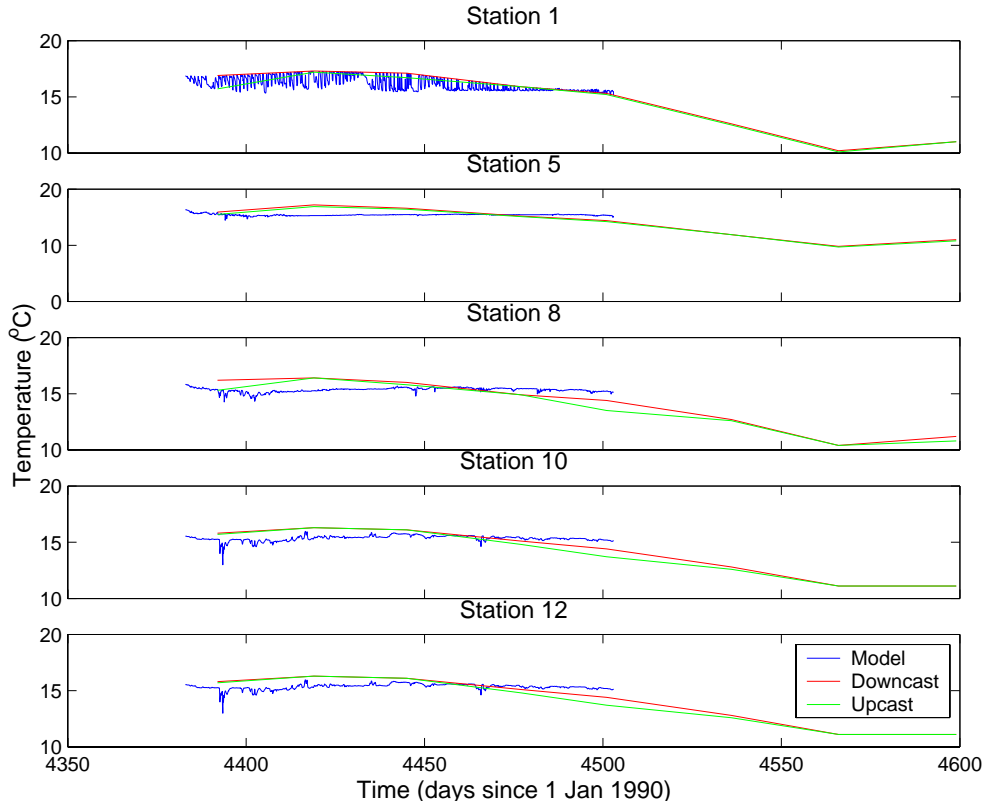


**Fig. 26. Modelled and Observed Temperature at Station 8**

Note that cooler input from the Huon River may contribute to temperature changes in the cooler months, however, these calculations suggest that boundary driven advection cannot be solely responsible for temperature changes in the mid-channel regions away from the open boundaries. The only possible alternate heat source is a heat flux through the surface, which should be accounted for in the model. This was calculated from standard meteorological measurements collected at Hobart airport (wet and dry bulb temperature, air pressure, wind speed and cloud amount) using short and longwave calculations outlined in Zillman (1972) and the bulk method for sensible and latent heat using bulk coefficients of Large and Pond (1981). The heatflux for the period 2002 is displayed in Fig. 27.

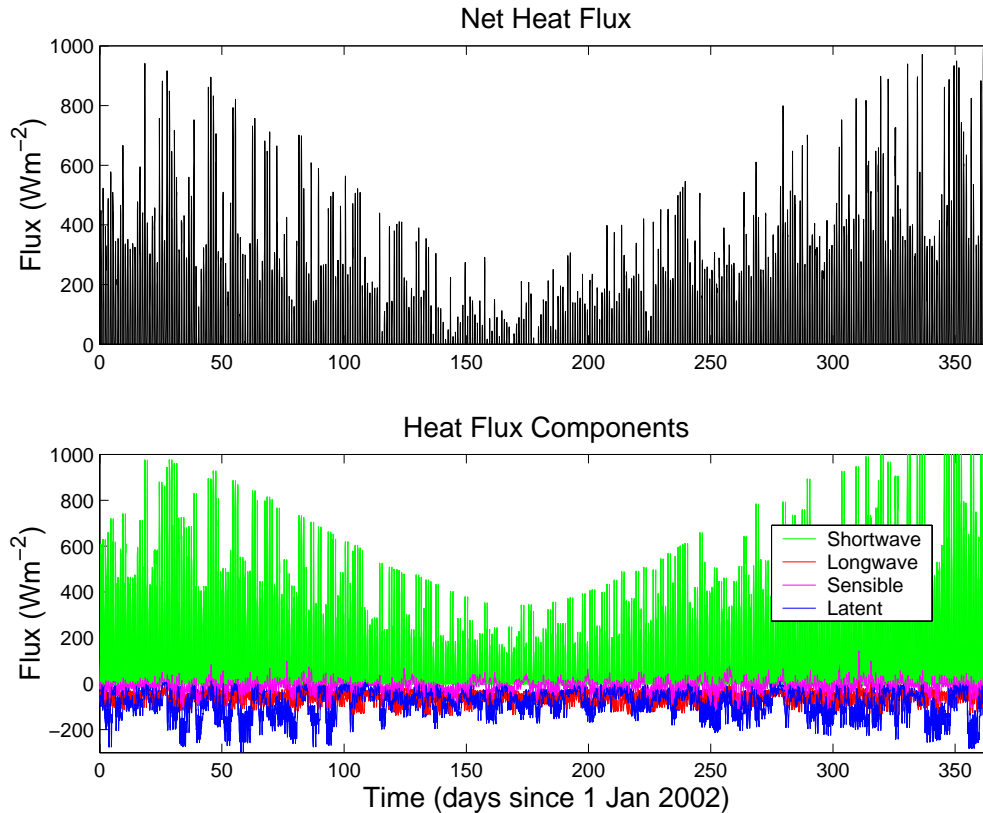


**Fig. 27. Heat Flux Characteristics for 2002**

The largest input of heat into the region is due to the short wave radiation component. During the winter months this decreases by approximately one-third in comparison to summer. The latent heat flux constitutes the largest heat loss term, with larger losses observed during summer. Long wave radiation is predominantly a loss although occasionally diffuse sky input results in net longwave input. The sensible heat flux can act as a source or sink of heat and remains relatively invariant throughout the year.

This heat flux was applied as the surface boundary condition for vertical diffusion of heat; the resulting temperature at the field station locations are displayed in Fig. 28. The annual cycle of SST is well captured by the model. The temperature distribution along the measurement section on March 2 is displayed in Fig. 29. This section is directly comparable to Fig. 7, and it is observed that the inclusion of heatflux terms greatly improved the temperature solutions.

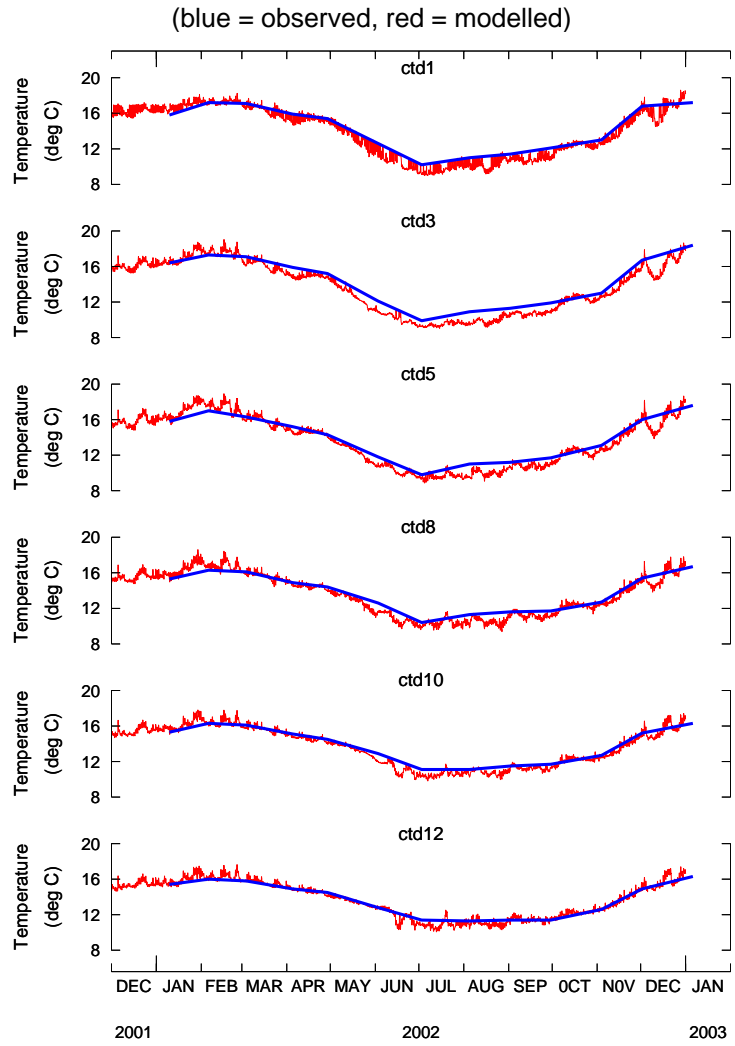


**Fig. 28. Surface Temperature with Heat Flux Included**

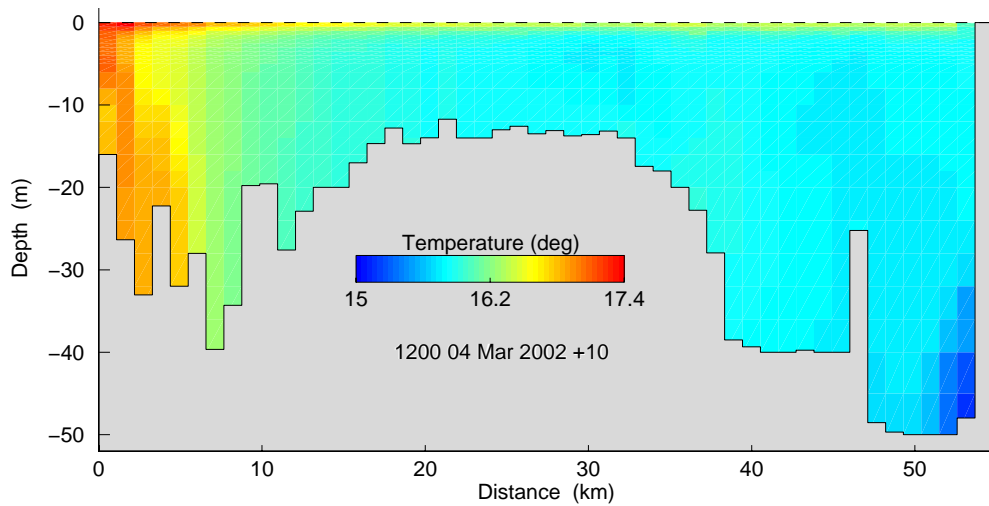


**Fig. 29. Modelled Temperature Section with Heat Flux Included**

The SST along a transect from the head of North West Bay (Station 1) into the channel (Station 11) is displayed in Table 5. It is observed that temperature is significantly higher at the head of the bay than the channel during summer, presumably due to differential heating associated with the gradient of bathymetry. This suggests that the shallow side bays adjacent to the main channel may play an important role in acting as a heat source for the main channel during summer, subject to exchange processes.

**Table 5. Sea Surface Temperature (SST) in North West Bay**

Date	Site 1 T (°C)	Site 4 T (°C)	Site 6 T (°C)	Site 9 T (°C)	Site 11 T (°C)
13/11/01	14.4	13.5	14.6	14.7	14.3
05/12/01	16.3				
17/12/01	17.1	16.7	15.8	15.6	
10/01/02	20.8	17.2	17.2	16.8	16.6
23/01/02	20.9	20.7	19.8	19.2	19.1
15/02/02	19.1	18.6	18.4	18.4	

Certainly from the data in Table 5 it appears that differential heating of North West Bay generated a strong SST gradient across the bay around 10 Jan 2001 (over 4°C temperature change). In order for this gradient to be maintained it can be assumed that the Bay remained in a relatively quiescent state for this period. The bay/channel appears to be subsequently exposed to exchange/mixing processes thus reducing the temperature gradient across the bay and elevating the temperature in the main channel around 23 Jan 2001. The temperatures at Stations 6, 7 and 8 from the broad-scale field program also indicate slight warming of Isthmus and Great Bays in summer (Table 6), whereas on 10 Jan the shallow side bay is 0.7 °C warmer than the main channel. When a strong net gain of heat at the sea surface is absent in ensuing months the side bay is consistently slightly cooler than the channel. The temperature solution for February with heat flux applied is displayed in Fig. 30, showing the above-mentioned temperature increase in the side bays due to differential heating.

**Table 6. SST in Isthmus and Great Bays**

Date	Station 5 T (°C)	Station 6 T (°C)	Station 7 T (°C)
10/01	15.9	16.6	16.6
06/02	17.2	14.8	17.1
04/03	16.6	16.7	16.4
05/04	15.2	14.9	15.0
29/04	14.4	14.2	14.3
03/06	11.9	11.8	11.5
03/07	9.8	9.8	9.8
05/08	11.0	10.5	10.2

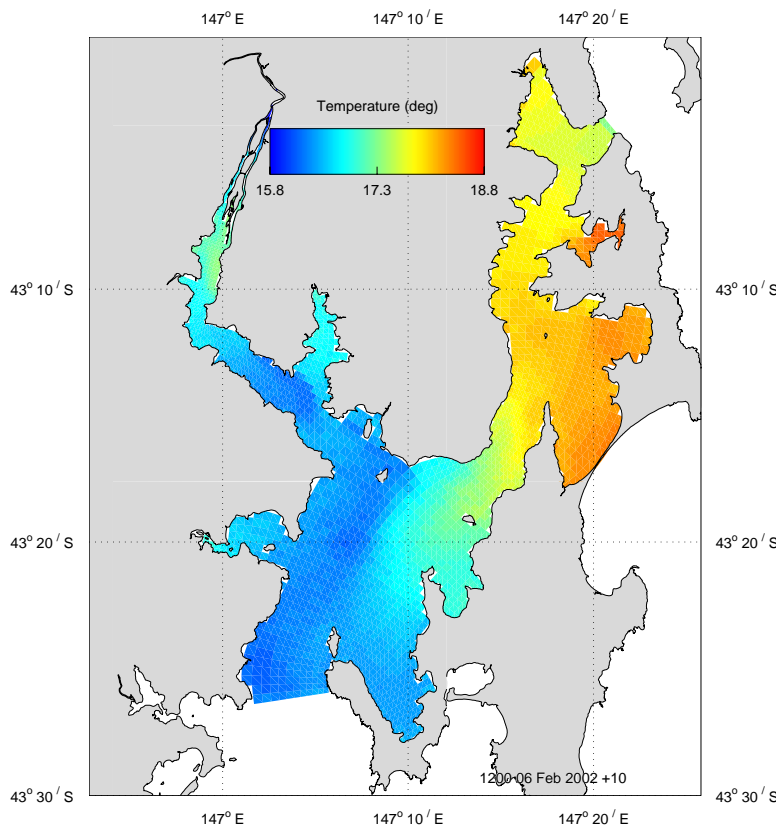


**Fig. 30. SST Solution for February 6 2002**

### 6.3 Nesting Procedure

Successively nesting local scale models inside larger regional models is a common practice that has two main advantages: (a) Regional models are capable of resolving large scale phenomena (e.g. boundary currents, mesoscale eddies, large scale upwelling, coastally trapped waves) that are not captured by local models. Motion resulting from these phenomena can be communicated into the local model through the open boundaries. (b) Open boundaries are notorious sources of error due to reflection and over-specification<sup>1</sup> problems. By prescribing measured data on regional open boundaries and using output of the regional model to drive the local model these problems are minimized.

The open boundaries of the model may be forced with either sea level or vertical profiles of velocity. The latter is the preferred method since all motion described by the momentum equations is represented, rather than just motion due to the pressure term as is the case with elevation forcing (i.e. non-linear effects are excluded in the elevation forced case). Velocity forcing is more problematic since velocity measurements are rarely available at the resolution required to force a model. Also, if velocity is available from a nesting process, this method is prone to over-specification which is difficult to alleviate using partially passive boundaries as is common with elevation forcing (e.g. Blumberg and Kantha, 1985).

It was observed that solutions of the local model compared more favourably to observation using a velocity forced northern boundary than the elevation-forced case (e.g. Fig. 31). This suggests that non-linear effects may be important in the Storm Bay area that contributes towards driving flow through the north entrance of D'Entrecasteaux Channel, probably through inertial effects of gyral activity or perhaps the influence of Derwent River flow. To avoid instabilities due to over-specification the southern boundary was partially passive by using a radiation condition (Miller and Thorpe, 1981) that was relaxed to prescribed elevation on a time-scale of 15 minutes.

The non-linearity of the boundary forcing was investigated further by examining the components contributing to the momentum balance (obtained from an intermediate scale model – see below) at Station 1 (Fig. 32). The  $u_1$  velocity component is oriented normal to the northern boundary (i.e. along-channel) in the local domain, and it is observed that the largest contributor to the velocity is the barotropic pressure gradient, i.e. the tide. However, the non-linear terms (advection and horizontal diffusion) are also dominant contributors to the balance; the horizontal diffusion tendency acting to always oppose the barotropic pressure gradient and non-linear advection acting to induce flow into the channel. If these non-linear terms were absent, the flow would be over-estimated on the flood tide and under-estimated on the ebb (e.g. difference between black and yellow curves). For the  $u_2$  velocity component (across-channel) the non-linear terms are the dominant contributors to the momentum balance and oppose each other. It is clear that

---

<sup>1</sup> Over-specification occurs when the data the model is being forced with is not compatible with the solutions provided by the equations in the domain interior (see Marchesiello et al., 2001).

non-linearity is important in this region, and as stated above, the flow cannot be represented accurately in the northern local domain by only prescribing the pressure gradient at the boundary.

The regional model resolves the northern open boundary of the local model quite poorly; hence an intermediate model was constructed with the aim of generating more accurate velocities with which to force the local model. A three level nesting process was therefore used; a regional model which forced the open boundary of an intermediate model with sea level, and the local model which was forced on the northern boundary with velocity and the southern boundary with elevation derived from the intermediate model (Fig. 33).

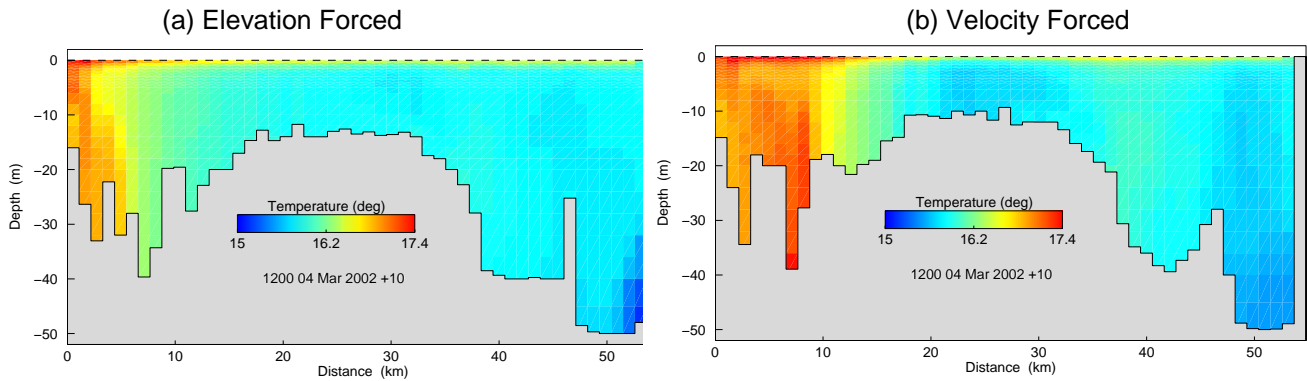


**Fig. 31. SST for 04 March 2002 using elevation and velocity forcing. These sections are comparable with Fig. 7.**

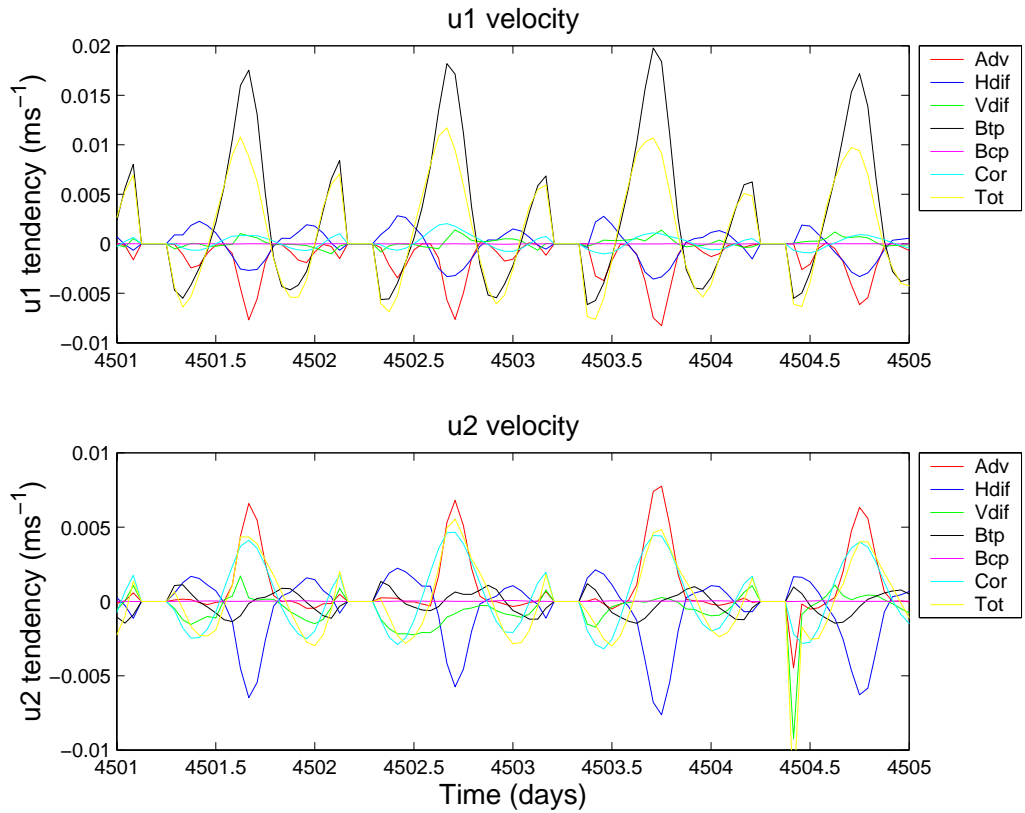


**Fig. 32. Momentum balance components for Station 1, intermediate grid.** Adv = advective terms, Hdif = horizontal diffusion terms, Vdif = vertical diffusion terms, Btp = barotropic pressure gradient, Bcp = baroclinic pressure gradient, Cor = Coriolis term and Tot = total tendency.

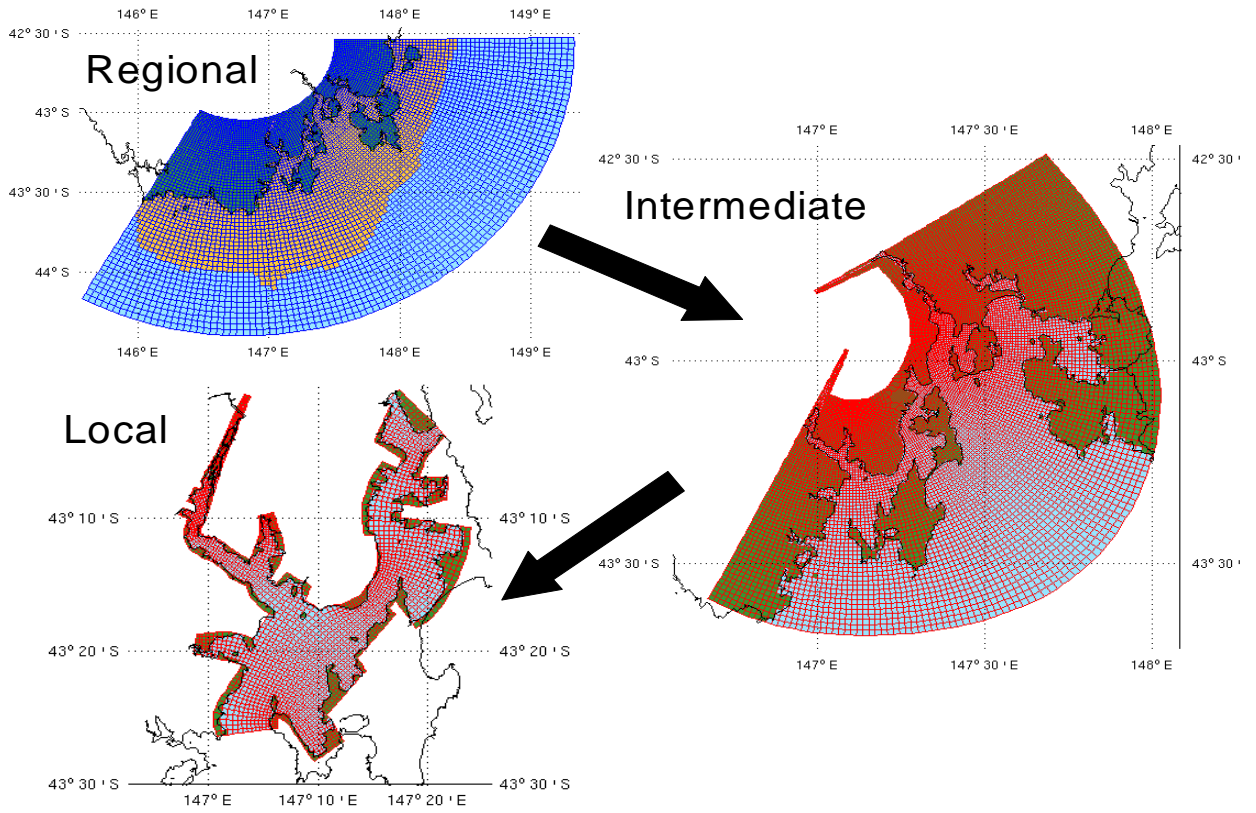
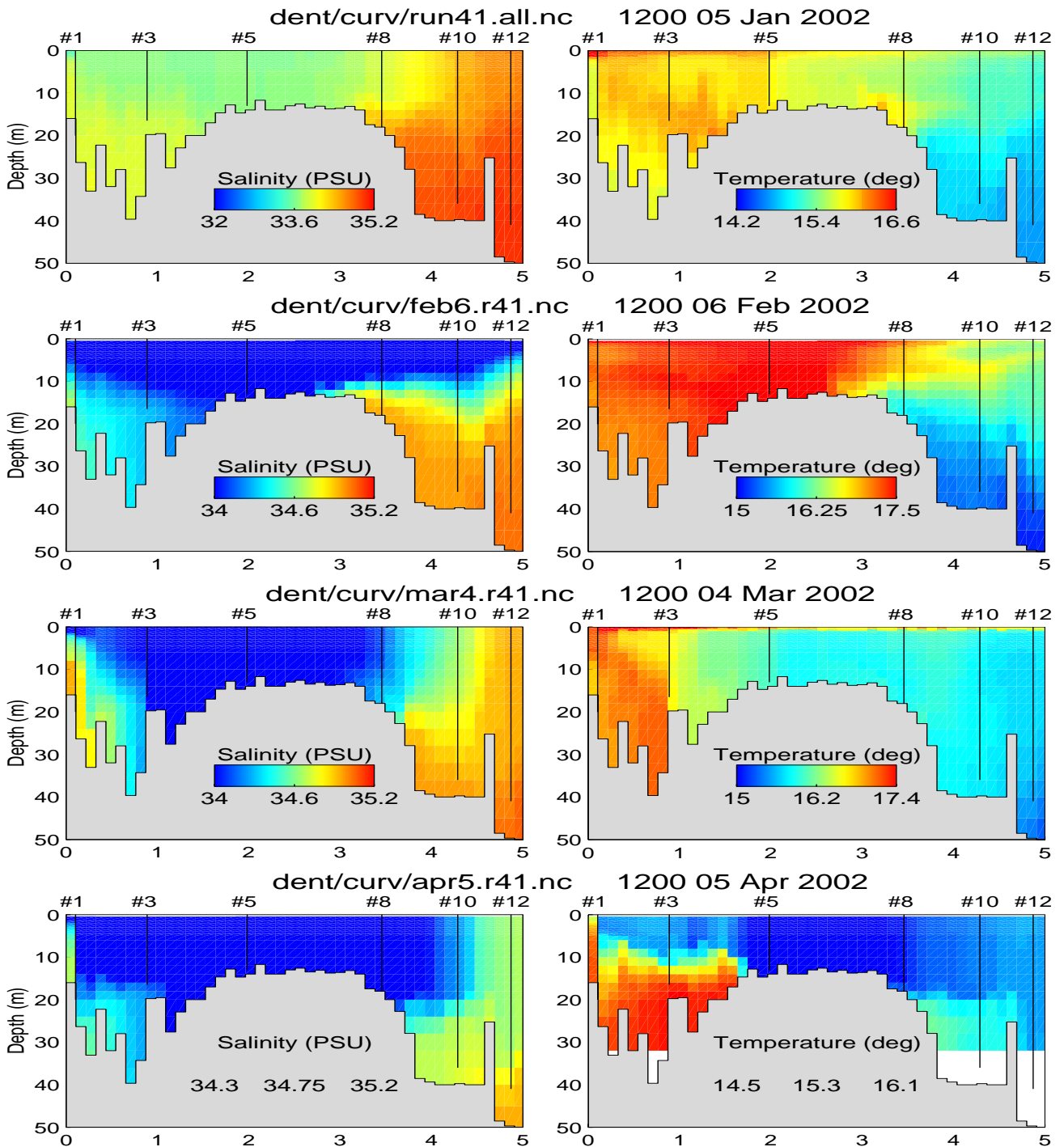


**Fig. 33. Nesting procedure**

# 7 Model Output

## 7.1 Model Calibration

The simulation period for all models was Jan 2001 to Jan 2002. Data from the broad-scale monitoring program along the main channel (Fig. 4) was used for calibration and validation for the model. The first 3 months of 2002 were used to obtain an acceptable calibration, and the remainder of the year was used to validate this calibration. The sections along the main channel, directly comparable to Figs 5 to 16, are displayed in Fig. 34 and time series at the broad-scale sampling sites are displayed in Fig. 35.



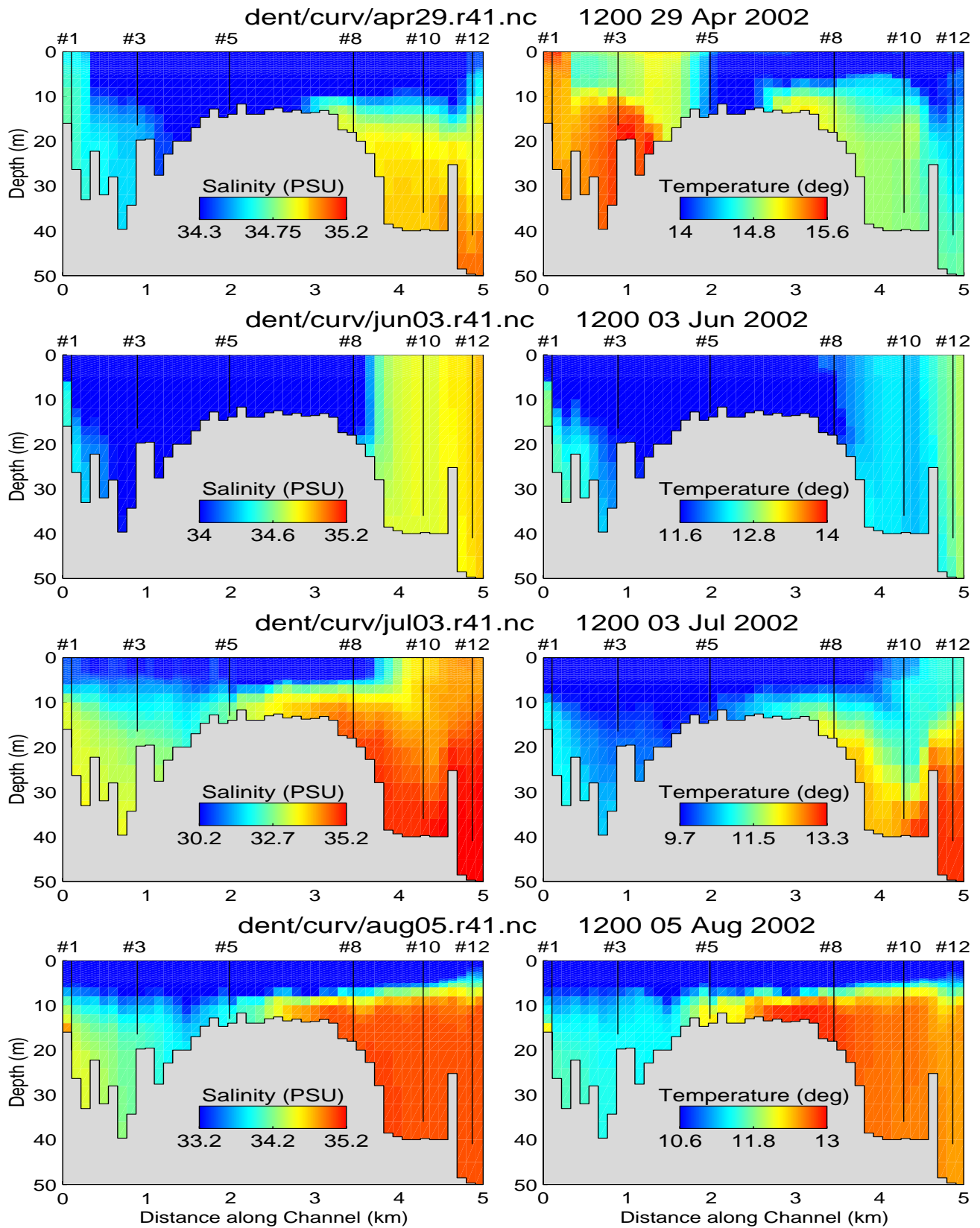


**Fig. 34. Modelled temperature and salinity sections**

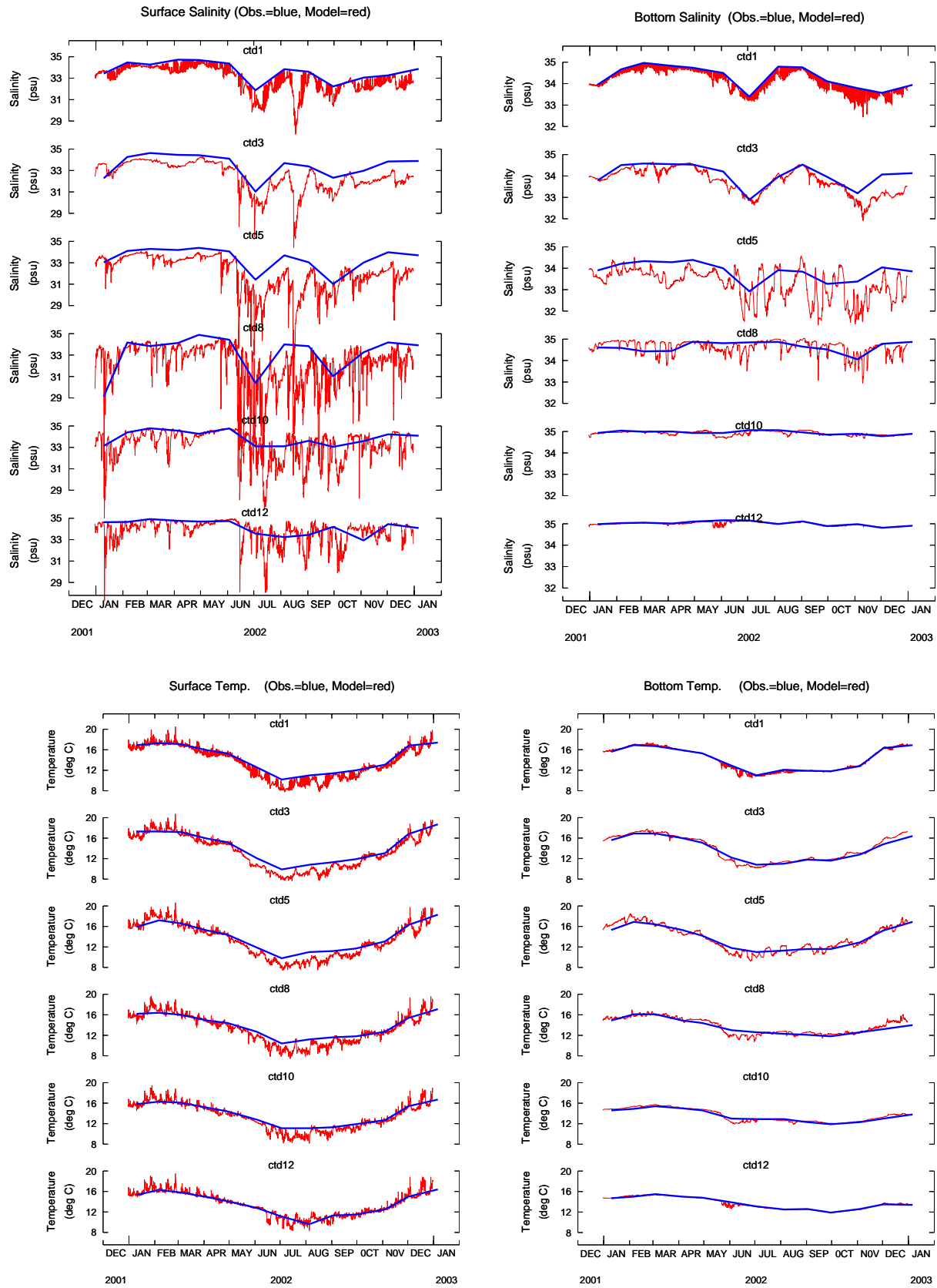


**Fig. 35. T/S time series comparison of observation and model results at monitoring stations.**

## 7.2 Sensitivity

During the calibration procedure an assessment of the sensitivity of model parameters and processes was made. As noted in section 6.2, the temperature solutions are very sensitive to surface heat flux parameterisations; particularly requiring short wave radiation to be depth distributed and being sensitive to the type of bulk scheme employed for sensible and latent heat fluxes. Examples of this sensitivity are displayed in Figs 36 and 37 which show salinity and temperature sections for March 2002 resulting from using two different bulk schemes for the latent and sensible heat fluxes. These Figures may be directly compared with measured data, Fig. 7. It can be seen that the temperature solutions show significant difference at the northern end of the channel (Stations 1 and 3), where the scheme of Kondo (1975) overestimates latent heat loss and excessively cools the channel in comparison to the scheme of Large and Pond (1982). The Large and Pond scheme was used in the verification simulations.

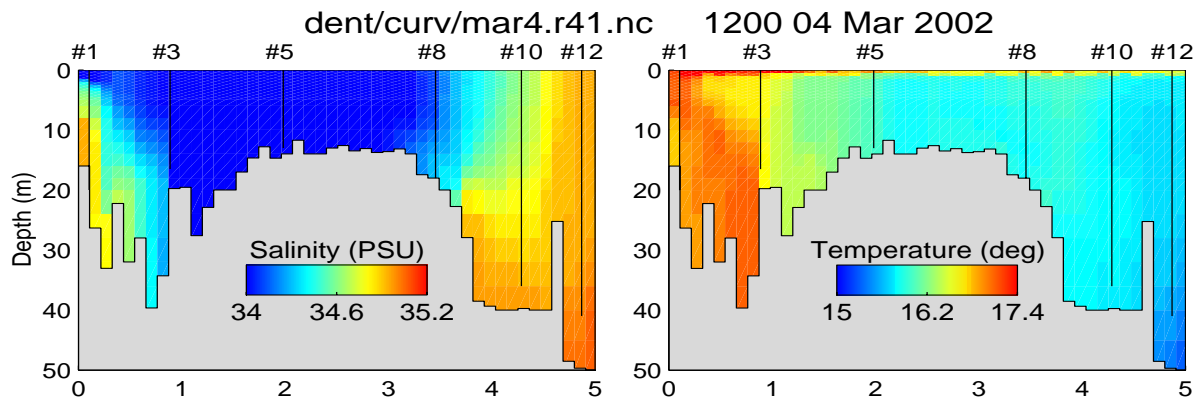


**Fig. 36. March sections using the bulk scheme of Kondo (1975)**

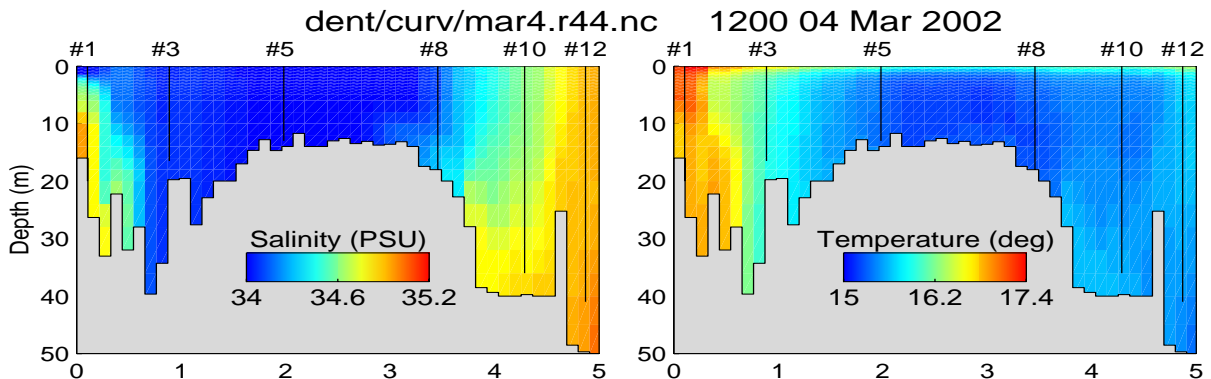


**Fig. 37. March sections using the bulk scheme of Large and Pond (1982)**

Solutions exhibited slight variability in response to the type of mixing scheme employed and the background diffusion coefficients prescribed for those schemes. Increasing background mixing tended towards a more well mixed solution which particularly impacted on the development of salt-wedge circulation in the Huon Estuary by pushing the equilibrium position of the salt-wedge downstream. Bottom salinity also became too low in the northern and mid-channel regions due to excessive mixing with fresher surface water. Too little background mixing resulted in the development of a stable surface skin due to short wave radiation input, which consequently further reduced surface mixing and led to too small mixed layers in the main channel. A vertical diffusivity of around  $1 \times 10^{-5} \text{ m}^2 \text{ s}^{-1}$  was found to be optimum. The effect of background diffusion coefficients is illustrated in Fig. 38, where comparisons mid-year at Station 5 represents the most dramatic difference in the solutions.

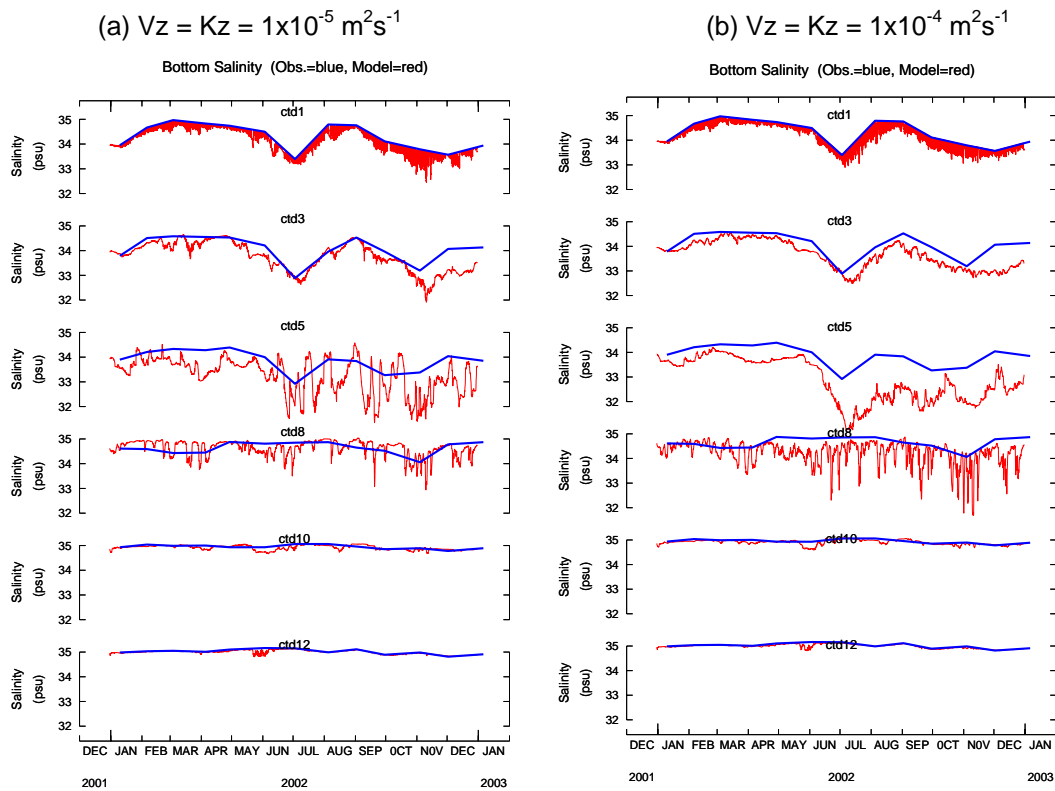


**Fig. 38. Bottom salinity resulting from different background mixing**

Bottom salinity exhibited the largest variation due to the choice of mixing scheme (Fig. 29) where the Mellor-Yamada 2.0 (Mellor and Yamada, 1982) scheme showed the best performance. The improved Mellor-Yamada 2.0 scheme features alternate turbulence length scale parameterization (Burchard et al, 1999) and is based on a three layer system where surface and bottom mixed layers are intersected by a stably stratified interior layer. This scheme generally delivers better performance in highly stratified regions such as the head of the Huon Estuary, but was generally not as stable as the Mellor-Yamada 2.0 scheme. The k-ε scheme (Burchard et al, 1998) generally provides too much mixing in

the highly stratified salt-wedge regions. The Mellor-Yamada 2.0 was considered optimum due to the better performance in the Huon Estuary mouth and main channel.

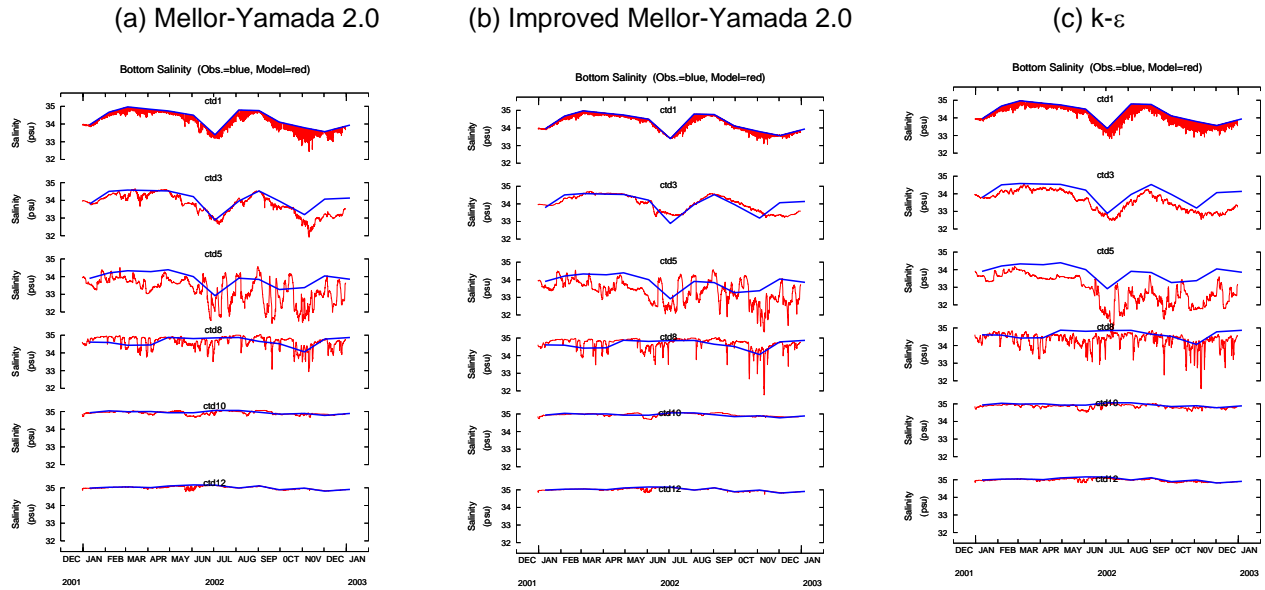


**Fig. 39. Bottom salinity resulting from 3 different mixing schemes**

The magnitude of the Huon River flow also impacted on the solutions; the less Huon flow the saltier and cooler the waters in the channel became. Reducing the flow by a factor of 1.2 (this was the scaling factor applied to allow for catchment area contributing to flow below Frying Pan Creek; section 5.4) resulted in negligible difference in solutions, whereas a distinct cooling in the channel was observed when the Huon flow was set to zero, especially in bottom water (Fig. 40). Also, as expected, the channel remained considerably saltier with little deviation below 34 psu. This suggests that the Huon River is also an important contributor of heat to the main channel. Increasing the salinity of the Huon River from 0 to 3 psu resulted in negligible changes to the salinity solutions in the channel.

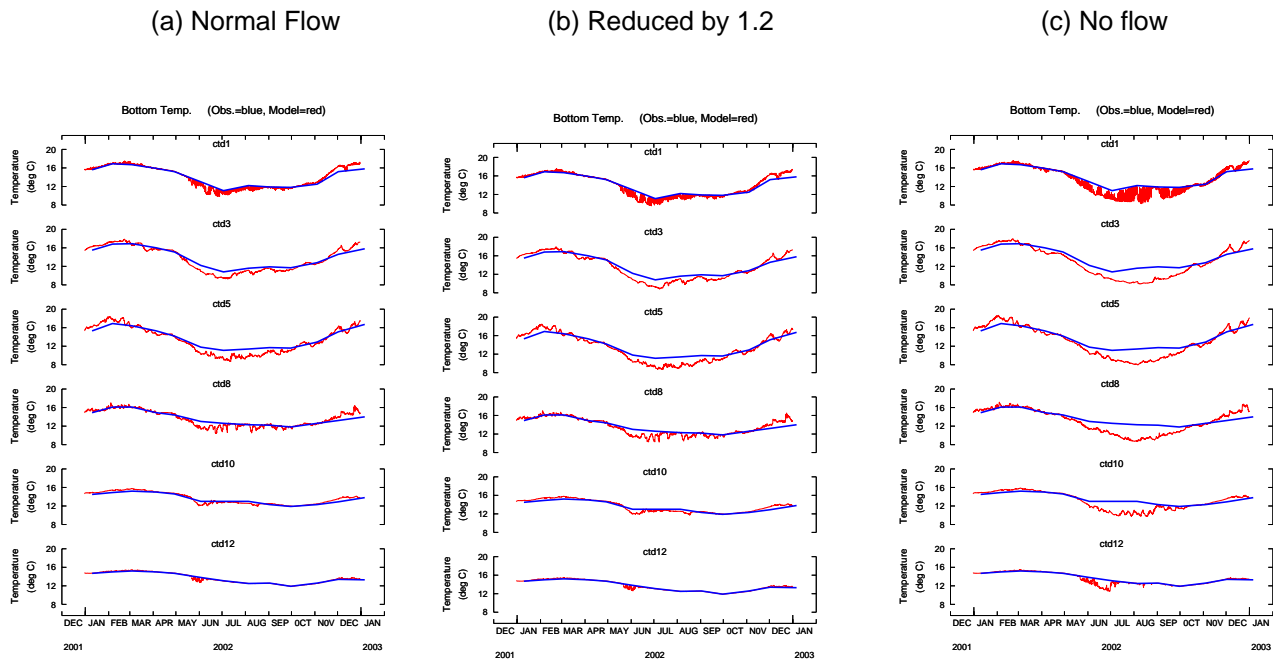


**Fig. 40. Bottom temperature resulting from 3 different flow regimes.** These simulations were performed with the improved Mellor-Yamada mixing.

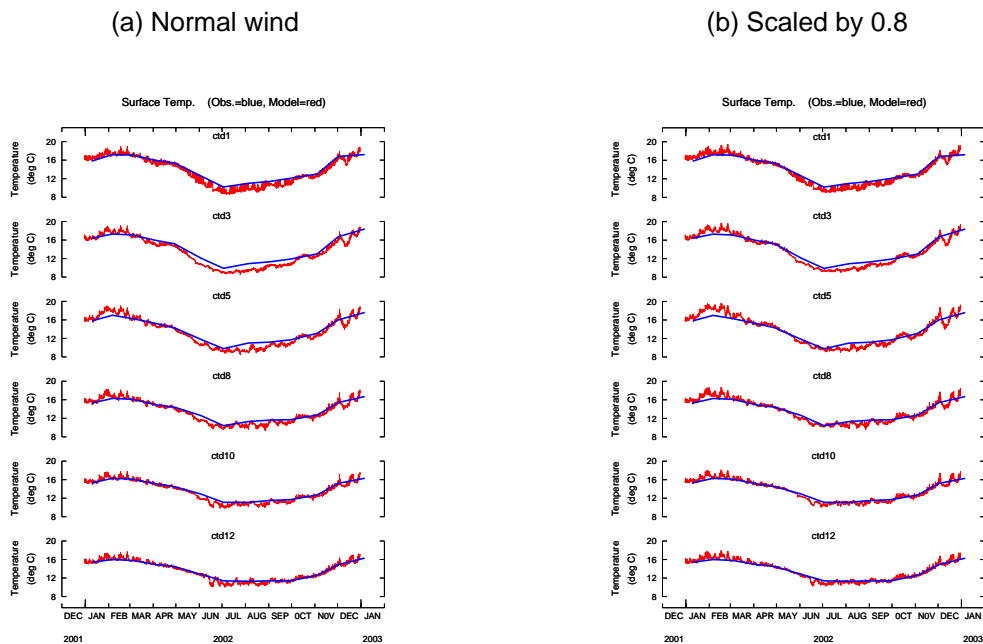


**Fig. 41. Surface temperature resulting from 2 different wind regimes.** These simulations were performed with the improved Mellor-Yamada mixing.

The applied wind stress has a two fold impact on the model solutions. Firstly the wind stress magnitude and direction affects the wind driven transport in the domain. Although the broad-scale wind characteristics are well represented using the interpolated wind from measurement sites (Fig. 18), local fluctuations, particularly due to topographic steering, may alter the wind and thus local circulation at certain points. A more intensive local sampling strategy is required to be implemented to address this issue. The wind stress also supplies energy for vertical mixing and is therefore important for regulating mixed layer depths. The model was run with a scaling of 0.8 applied to the wind. This resulted in little overall change in the temperature or salinity solutions. Surface temperatures at the northern end of the channel (Stations 3 and 5) during summer were slightly elevated, but winter temperatures were comparable (Fig. 41).

In this case the reduction in wind appears to decrease the mixed layer depth in summer resulting in warmer surface temperatures as the surface heat flux is distributed throughout a smaller volume. The absence of any significant difference in surface temperature in winter suggests that mixing is dominated by convective mixing due to surface cooling during this time. It is expected that dramatic changes in wind speed are required to alter the mixing regime to such an extent where manifestations are apparent in the temperature and salinity solutions.

Solutions did not alter to any great degree in response to the choice of bottom roughness, layer thickness, minimum coastal depth or horizontal mixing coefficients.

### 7.3 General Model Solutions

The annual cycle of temperature and salinity in the Huon-D'Entrecasteaux region is displayed in Figs 33 and 34. Generally the model tends to be slightly fresh and cool mid-channel in the winter months. The warmer winter southern bottom water and associated seasonal variability described in Section 4 is also evident. The Huon-D'Entrecasteaux system is micro-tidal with spring tide ranges up to 1 m. The diurnal tide has a range that is slightly larger than the semi-diurnal tide, and sea level in the region varies between periods of pure diurnal to pure semi-diurnal character (e.g. Fig. 42, semi-diurnal character around 18 July, diurnal character around 26 July). This is quantified by the form factor  $F = \text{ratio of diurnal to semi-diurnal amplitudes} (F = K_1 + O_1 / M_2 + S_2)$ , which in the case of the D'Entrecasteaux  $\sim 1.5$  verifying that the tide is of predominantly diurnal mixed character. The Huon Estuary is a salt-wedge estuary characterized by a freshwater layer overlying a saline wedge that intrudes up estuary. Fig. 43 shows this fresh layer overlying the salt wedge which propagates up to the river boundary at Huonville under low flow conditions. During periods of high flow a distinct fresh water plume is seen to emanate from the Huon Estuary and propagate up the D'Entrecasteaux Channel towards the northern boundary (Fig. 44a). This fresh water plume appears to favour the northern side of the estuary within the Huon, consistent with observation. Little fresh water makes its way to the southern boundary, and this occurs only under the influence of north-easterly winds (Section 7.5). Under high flow the salt wedge in the Huon Estuary is pushed downstream (Fig. 44b). Maximum current velocities are observed midway up the D'Entrecasteaux channel at the narrowest point near Gordon, and may reach more than

0.5ms<sup>-1</sup> at times (evidence exists in sediment composition at this location to suggest there are persistent strong currents in the region). These currents are predominately tidal in nature, exhibiting a distinct oscillation at the tidal frequency (Fig. 7.3.4). Motion is generally directed up-channel and up-river during the flood tide and down-channel and down-river during the ebb (see Section 7.5). Sea level gradients are low throughout the domain.

The general net flow through the system is inflow in bottom waters at the southern boundary following a route up the Huon Estuary in the salt wedge. Entrainment into the fresh river flow then carries water down-river into the channel where net flow up-channel out of the northern boundary occurs (Section 7.5).

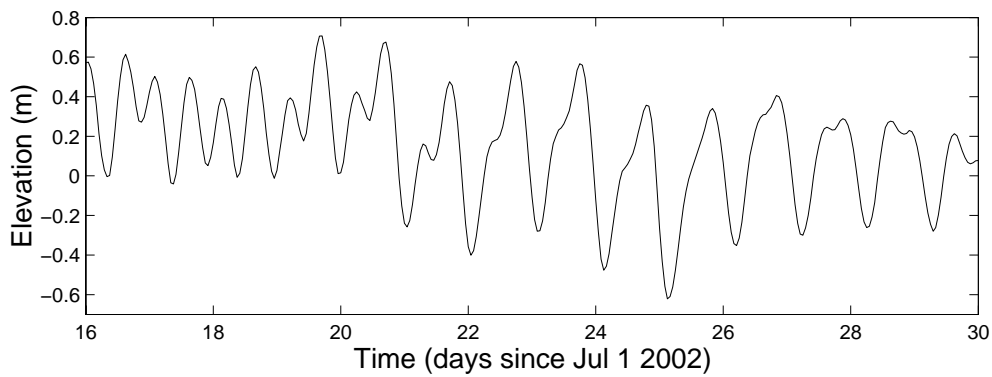


**Fig. 42. Tidal height at Station 10, July 2002**

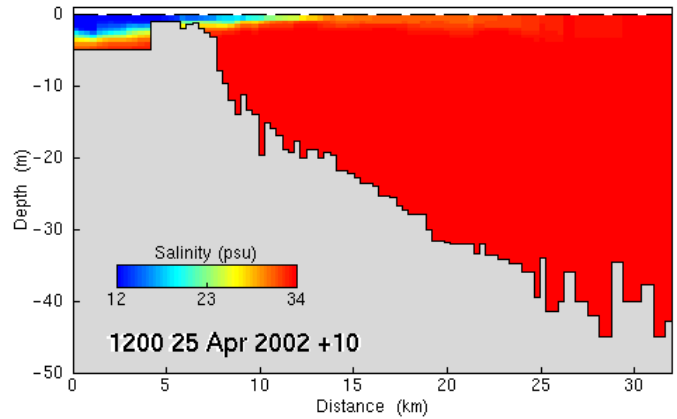
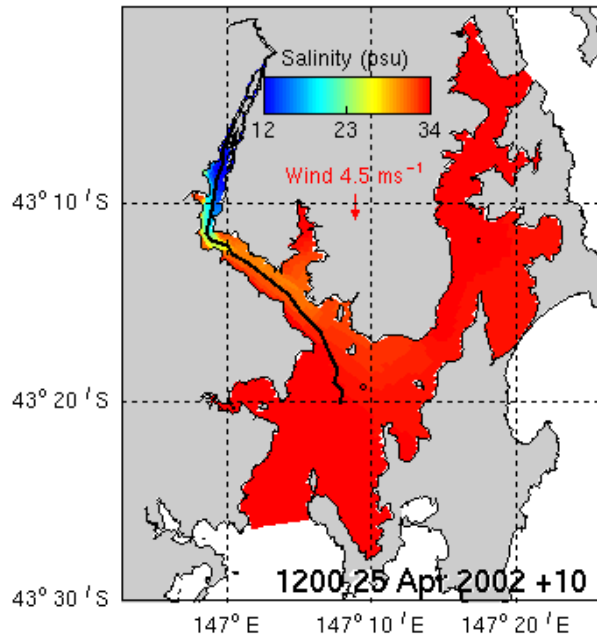
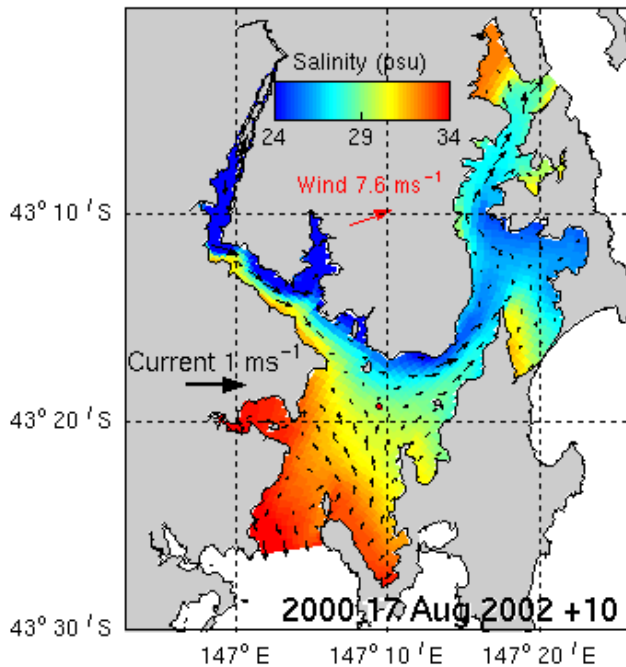


**Fig. 43. Plan view of surface salinity distribution and Huon Estuary section on 15 Apr 2002.** River flow is  $\sim 10 \text{ m}^3 \text{ s}^{-1}$ . The section location is marked on Fig. (a).

(a) Plan 17 Aug



(b) Section 18 Aug

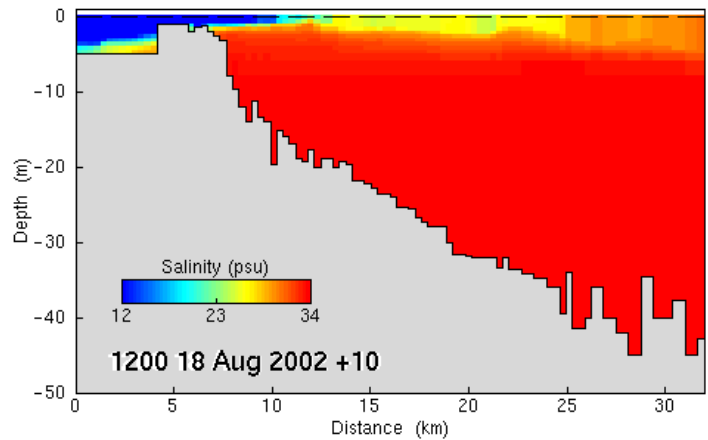


**Fig. 44. Surface salinity and surface currents during  $\sim 1000 \text{ m}^3 \text{ s}^{-1}$  flood.** Tide is ebbing with a range of 0.83 m.

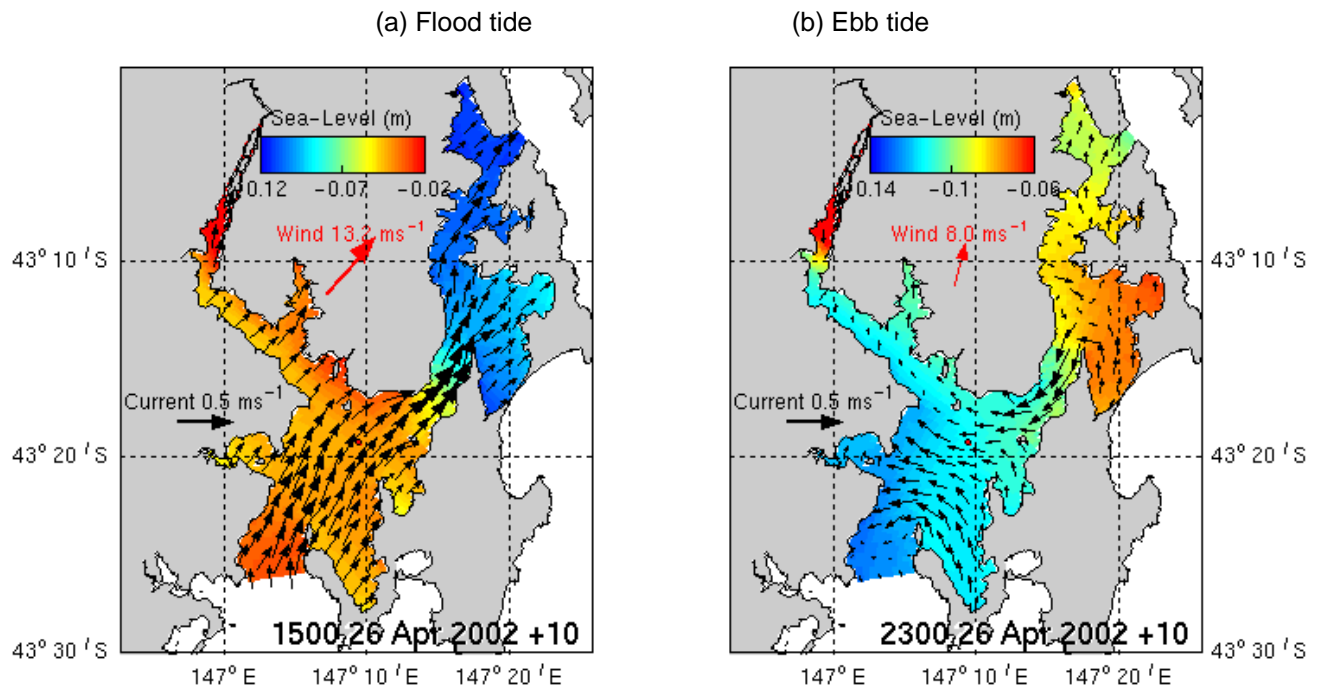


**Fig. 45. Surface currents and sea level on 26 Apr 2002.**  
Tidal range is  $\sim 0.7 \text{ m}$  and river flow is  $\sim 10 \text{ m}^3 \text{ s}^{-1}$ .

## 7.4 Momentum Balance

The model is capable of diagnosing the contribution from each term in the momentum balance to the change in velocity. This is in the form of a velocity tendency in  $\text{ms}^{-1}$  for each term in the momentum balance; i.e. momentum advection, horizontal diffusion (mixing), Coriolis (rotation), vertical diffusion (vertical mixing), barotropic pressure gradient forces (sea level gradients) and baroclinic pressure gradient forces (density gradients). Generally near the surface vertical diffusion represents the contribution due to the wind, which acts to accelerate the flow. Near the bottom vertical diffusion represents bottom drag which acts to retard the flow. The sum of all tendencies is equal to the total change in velocity over one time step. Note that the sum of tendencies is *not* equal to the actual velocity at any particular time, and must be added to the velocity at the previous time-step in order to obtain this actual velocity. Under steady state conditions the total tendency is zero and all momentum tendencies must balance. For non-steady motion one or several tendencies may dominate resulting in non-zero total tendency and acceleration of flow. Momentum tendencies are useful in evaluating the relative contributions of each

forcing mechanism and diagnosing the dominant forcing mechanisms that drive motion in the domain.

The local momentum balance varies markedly in time and space throughout the domain depending on wind strength and direction, river flow and the phase of the diurnal tide and neap-spring tidal cycle. A snapshot at Station 8 (approximately the middle of the domain) is presented in Fig. 42 for the surface and 43 for the bottom. During this time river flow varies from  $\sim 10 - 70 \text{ m}^3\text{s}^{-1}$  (low flow) and the tide was passing through a neap phase with minimum tidal range of 0.25 m occurring on 13 Apr and maximum range of 0.68 occurring on 19 Apr. Wind was generally low, coming from the south-western quadrant with speeds of around  $3 \text{ ms}^{-1}$  and an easterly maximum of  $\sim 7 \text{ ms}^{-1}$ . The along-channel direction corresponds to the  $u_1$  velocity and cross-channel direction by the  $u_2$  velocity. Fig. 42 shows that generally the barotropic pressure gradient (i.e. tidal forcing, black line in Fig. 42) and vertical diffusion (green line) dominates the solutions. This time series is taken at the surface, hence vertical diffusion represents acceleration on the flow due to the wind. The tide and wind are opposed by the Coriolis force (aqua line). The contributions from baroclinic pressure gradient forcing, momentum advection and horizontal diffusion are small in comparison. Therefore, a first order analysis is that surface motion in the domain is driven predominantly by wind and tide and balanced by Coriolis during this period. The bottom momentum balance (Fig. 43) is considerably different, with the frictional terms (horizontal and vertical diffusion) playing a more dominant role. All terms except the momentum advection contribute to the balance at this location. The momentum balance varies spatially and temporally throughout the domain, as mentioned above, hence while tendency snapshots are useful for diagnosing the momentum balance for a particular place and time, the characterisation of the system as a whole is difficult to capture. A mean momentum balance is of more use to infer the net motion in the domain.

The momentum tendencies are produced as a seasonal (90 day) mean in Figures 44 – 50 at Stations 1, 3, 5, 8, 10 and 12 (see Fig. 4), and the spatial distribution at the surface in Figures 51 – 66. The averaging process removes all contribution from the barotropic pressure, i.e. the tidal forcing has negligible contribution to the net flow. The relative contribution to the surface balance varies down the channel, as observed in Figs 44 to 49. At Station 1 for the  $u_1$  velocity (along-channel component) the baroclinic pressure is opposed by the advective forces. This was noted in Section 6.3 and prompted the use of velocity forcing at the northern boundary. The  $u_2$  velocity (cross-channel) component exhibits a balance between Coriolis and vertical diffusion, i.e. wind forcing. At Station 3 the along-channel component balance changes such that baroclinic pressure and Coriolis are opposed by the frictional terms. The cross-channel component remains similar to Station 1, except that the baroclinic pressure combines with Coriolis in the winter and spring. Coriolis is opposed by wind at Station 5 for the  $u_1$  component, with the baroclinic pressure contributing to Coriolis in the winter. A small up-channel momentum advection contribution exists throughout the year. The  $u_2$  component exhibits a balance between baroclinic pressure + Coriolis and vertical diffusion. During winter and spring the Coriolis influence lessens. At Station 8 the  $u_1$  component exhibits opposing baroclinic pressure and Coriolis forces. Wind contributes to Coriolis in the spring.

All the above stations exhibit a positive total tendency in the along-channel direction, indicating flow up-channel towards the north. This means that the baroclinic pressure and Coriolis forces are predominantly driving flow up-channel in the northern part of the channel. The cross channel total tendency is close to zero.

The balance at Station 10 for the  $u_1$  component is similar to Station 8, except the total tendency is close to zero at this location. The  $u_2$  component exhibits a balance between baroclinic pressure and vertical diffusion. At Station 12 Coriolis opposes the baroclinic pressure for the  $u_1$  component with an advective contribution to Coriolis in winter and spring. The total tendency is now negative, indicating down-channel flow. For the  $u_2$  component baroclinic pressure + advection opposes vertical diffusion + Coriolis. Again the total tendency is negative, indicating flow to the south-east.

The momentum balance mid-domain at the bottom (Station 8, Fig. 50) is again different to the surface. Baroclinic pressure dominates in the along-channel direction with horizontal friction predominantly providing the balancing force. Cross-channel horizontal friction balances vertical friction and the baroclinic pressure gradient. Horizontal friction generally plays a larger role in the bottom waters.

Care needs to be applied when interpreting the vertical diffusion tendency as a contribution by the wind, since if the drag on the sea floor is 'felt' at the surface (e.g. the bottom boundary layer extends to near the surface) then the vertical diffusion tendency may represent frictional effects retarding the flow rather than wind accelerating the flow. If the total tendency is zero (i.e. the tendencies balance) or vertical diffusion is of opposite sign to the total tendency then when vertical diffusion opposes baroclinic pressure (the pressure gradient is balanced by friction) this is a more likely scenario, whereas if vertical diffusion opposes Coriolis a more likely scenario is wind is balanced by Coriolis.

The spatial distributions for these seasonal means are shown in Figs 51 – 66. These Figures show the largest tendencies are due to the baroclinic pressure, vertical diffusion and Coriolis. The barotropic pressure tendency is negligible (Fig. 64). The Coriolis force tends to drive flow up-channel and cross-river towards the northern bank in the Huon (Fig. 65). In the Huon this is opposed by the baroclinic pressure gradient, which tends to drive flow towards the southern bank. Baroclinic flow in the D'Entrecasteaux is up-channel in the northern channel and towards the mainland in the southern channel (Fig. 65). The vertical diffusion tendency directs flow in the opposite direction in the channel, towards Bruny Island. In the Huon Estuary this tendency drives flow in a down-river direction (Fig. 63). These tendencies are generally strongest during winter and spring. The advective and horizontal diffusive tendencies show no coherent pattern and have maximum contributions in the upper Huon Estuary and the narrowest point of the channel near Gordon. Some boundary effects are also visible.

This analysis indicates that locally the tide and wind are dominant drivers of surface flow, opposed by the Coriolis force. The mean surface flow in the Huon Estuary is a balance between density forcing and Coriolis (as expected in a salt wedge estuary) with

wind contributing to down-river flow. In the northern channel density driven flow combines with rotation forces to produce seasonal up-channel residual flow. Cross channel forces balance in this area, with Coriolis opposing wind driven flow with some contribution of density effects to Coriolis. The southern channel exhibits both along and cross-channel net flow. Coriolis forcing opposes density forces in the along-channel direction while the wind driven flow opposes density driven flow in the cross-channel direction. Coriolis forcing is directed up-channel throughout the channel, whereas density effects are directed up-channel in the northern channel and down-channel in the southern channel. Horizontal friction becomes more important in bottom waters.

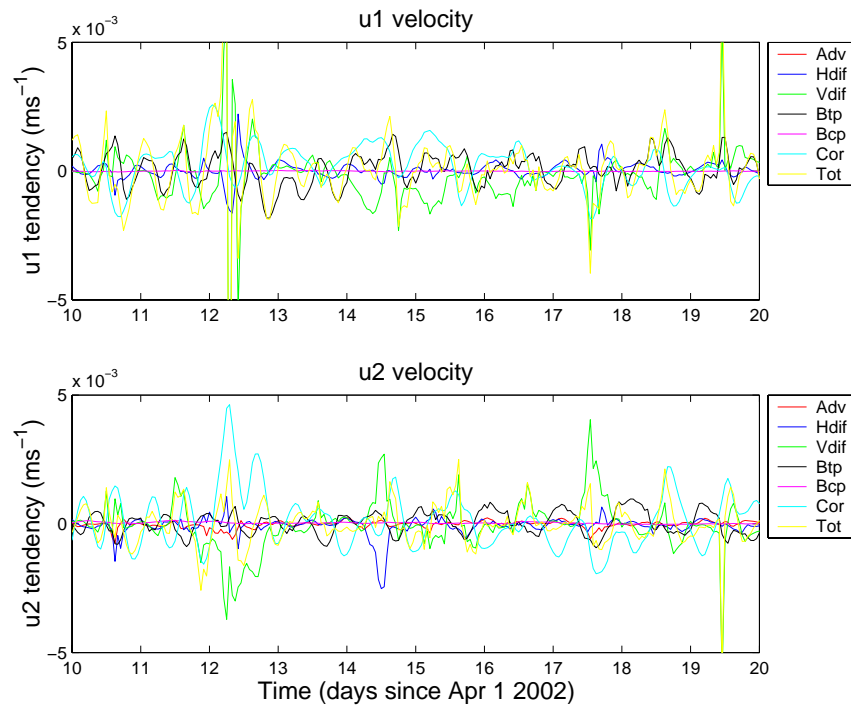


**Fig 42. Local surface momentum balance at station 8, 10 – 20 Apr 2002**  
 Adv = advective terms, Hdif = horizontal diffusion terms, Vdif = vertical diffusion terms, Btp = barotropic pressure gradient, Bcp = baroclinic pressure gradient, Cor = Coriolis term and Tot = total tendency.

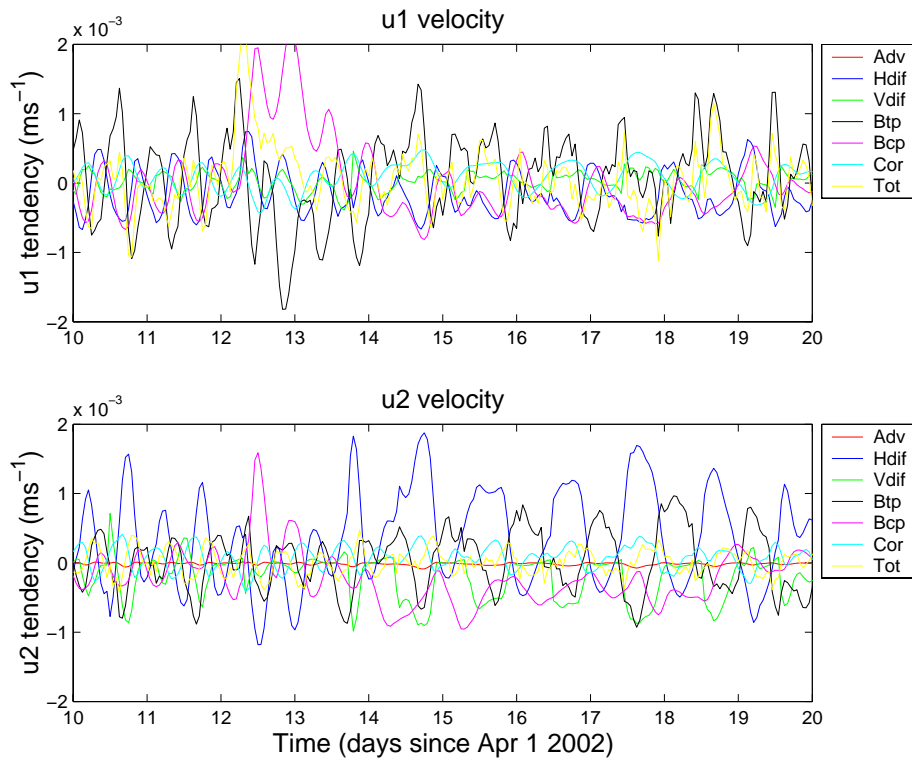


**Fig. 43. Local bottom momentum balance at station 8, 10 – 20 Apr 2002**

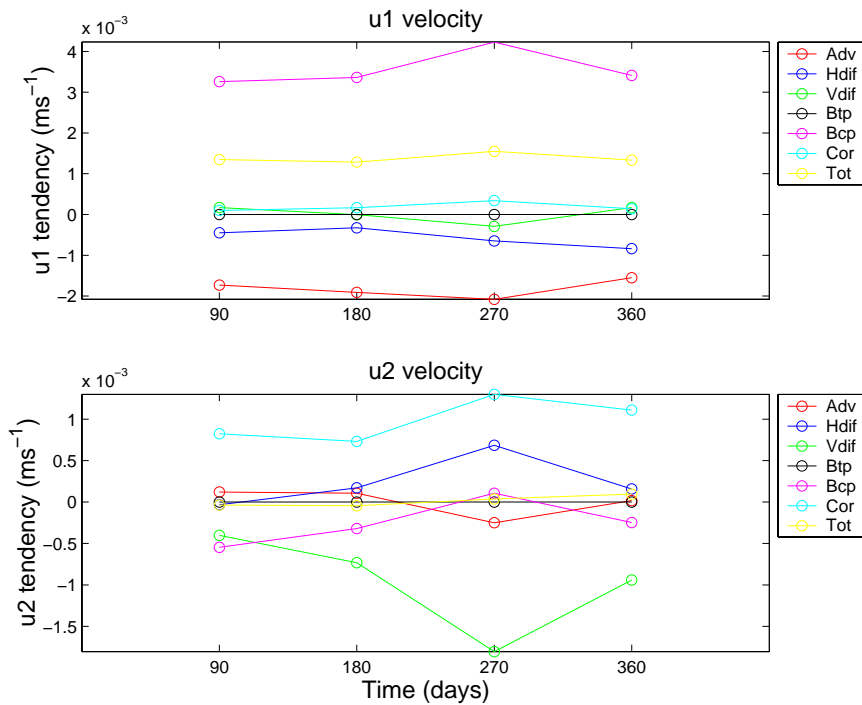


**Fig. 44. Surface momentum balance at Station 1.** Note: Day 90 corresponds to the mean from Jan to Mar (approximately summer), day 180 to autumn, day 270 to winter and day 360 to spring.

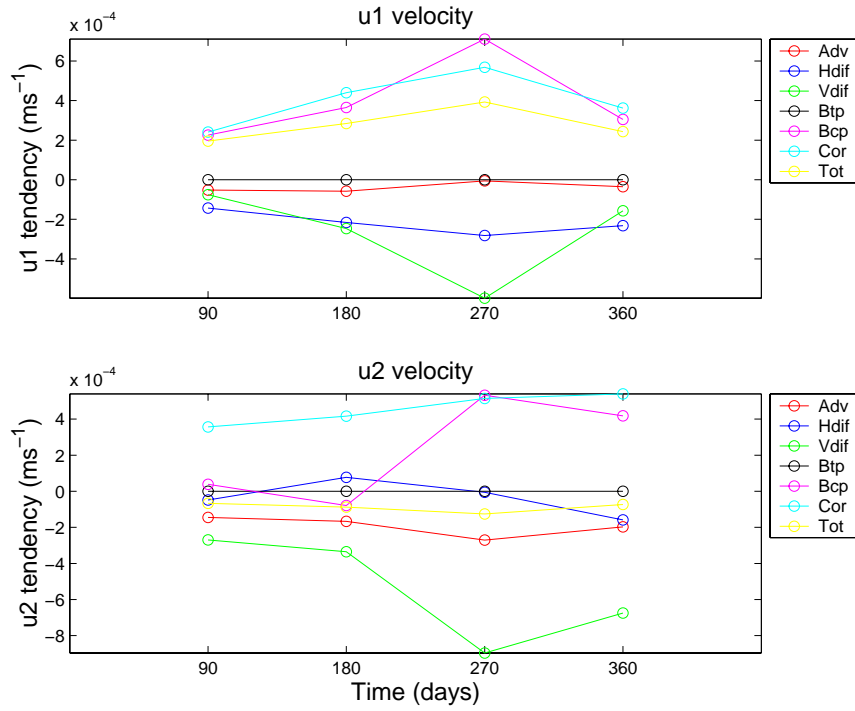


**Fig. 45. Surface momentum balance at Station 3**

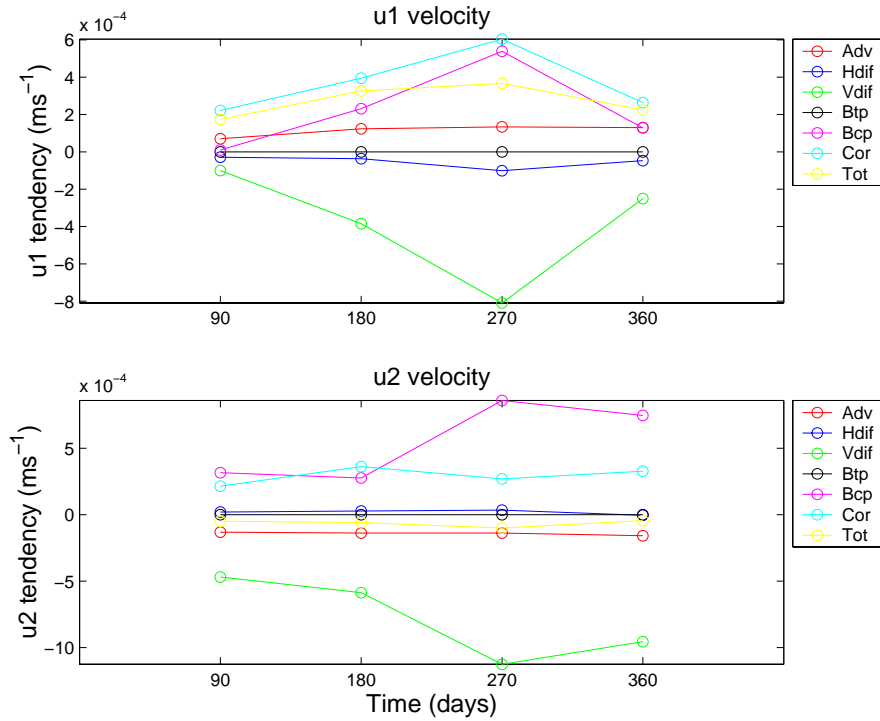


**Fig. 46. Surface momentum balance at Station 5**

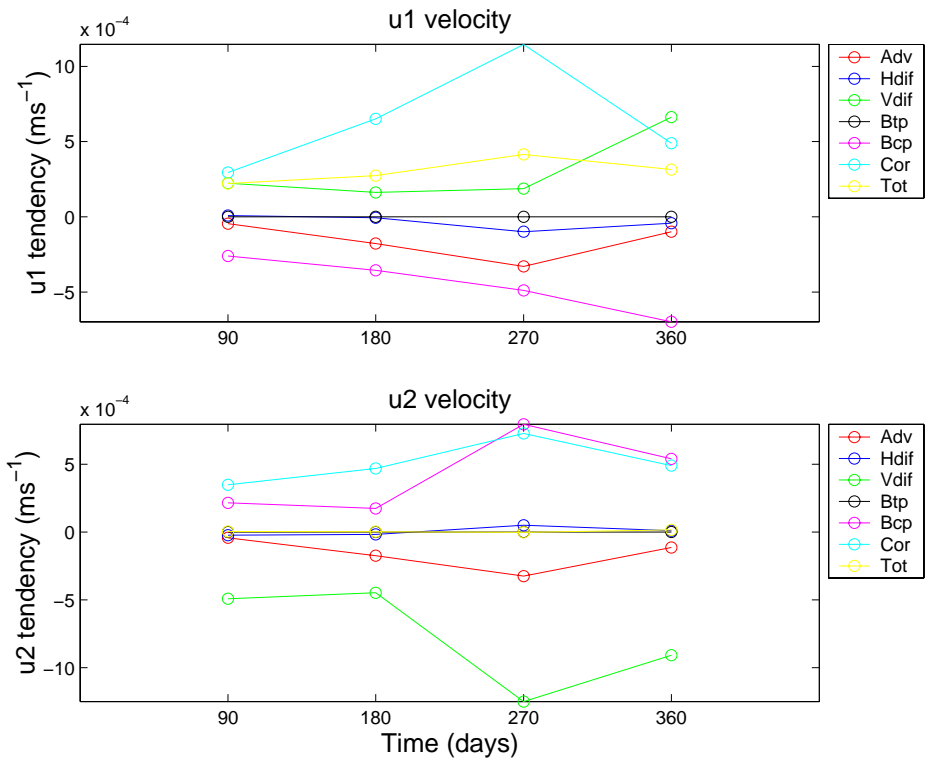


**Fig. 47. Surface momentum balance at Station 8**

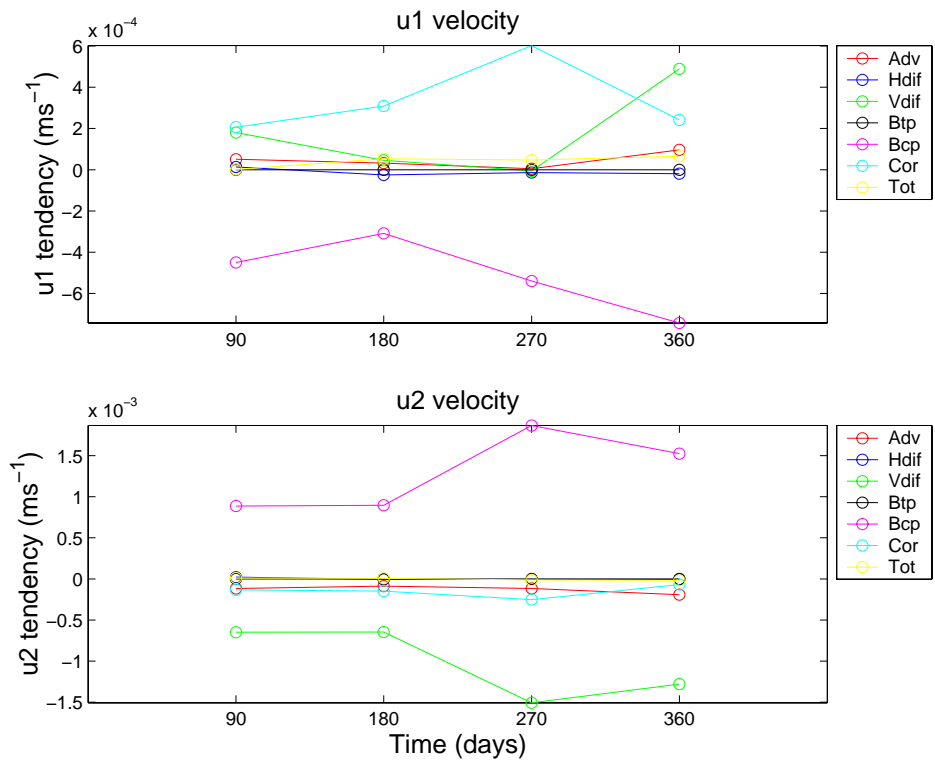


**Fig. 48: Surface momentum balance at Station 10**

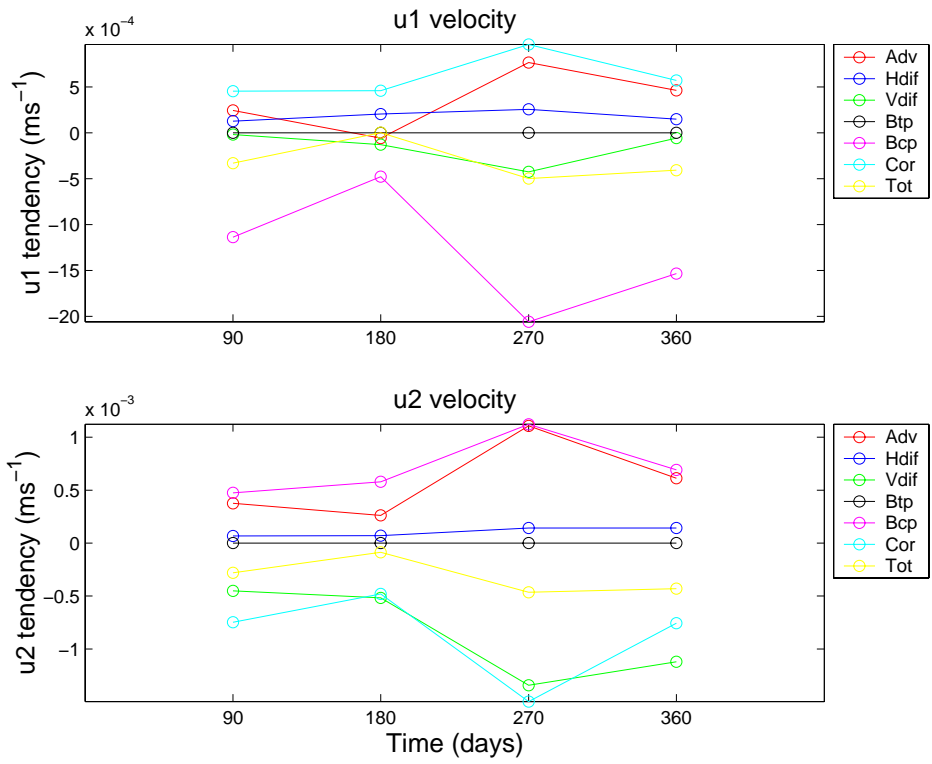


**Fig. 49. Surface momentum balance at Station 12**

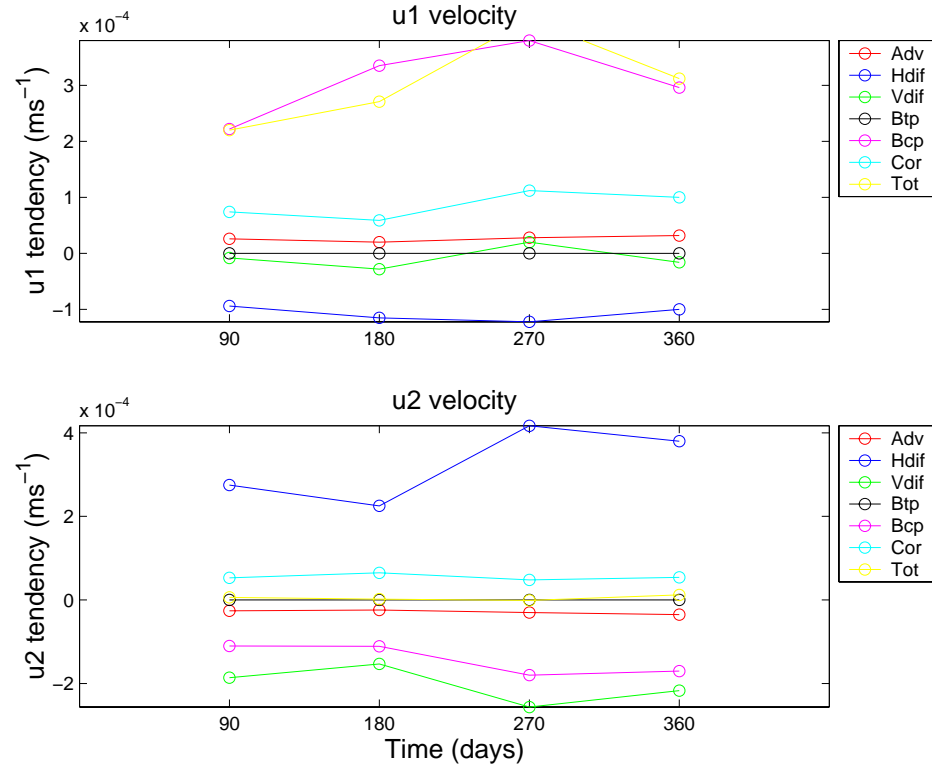


**Fig. 50. Bottom momentum balance at Station 8**

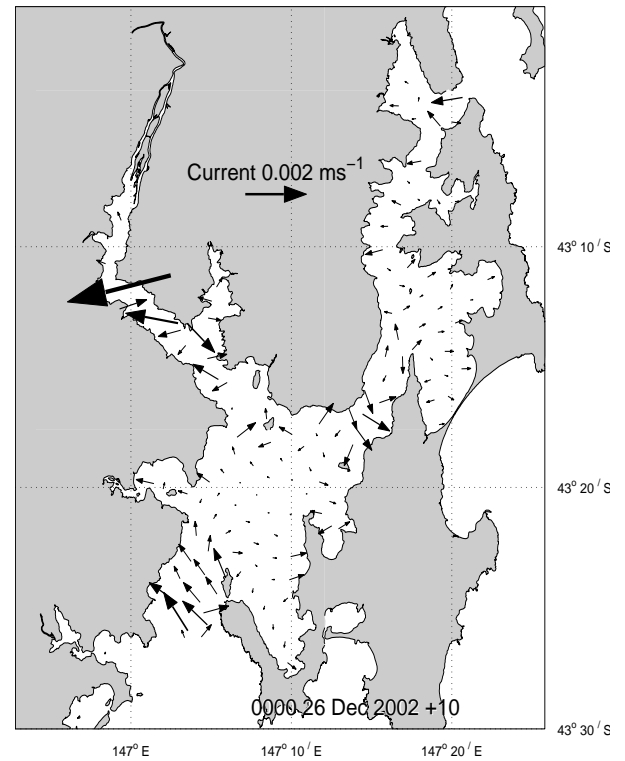
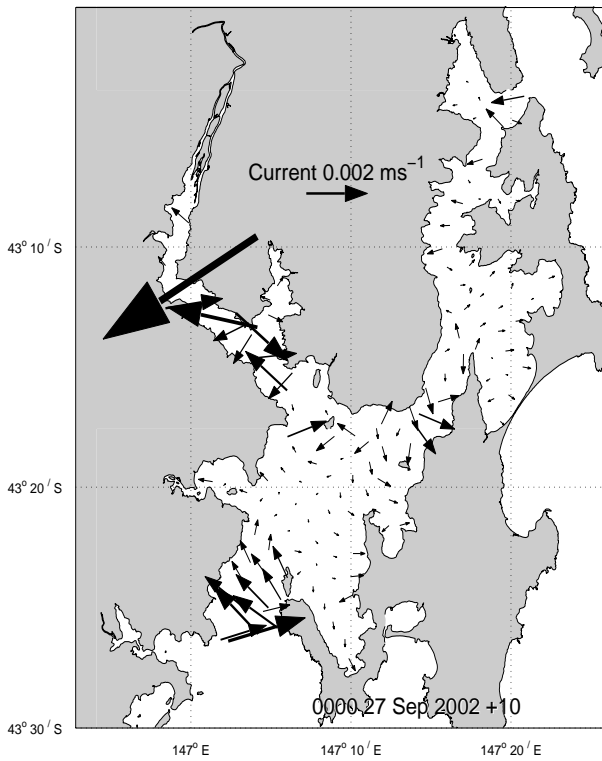
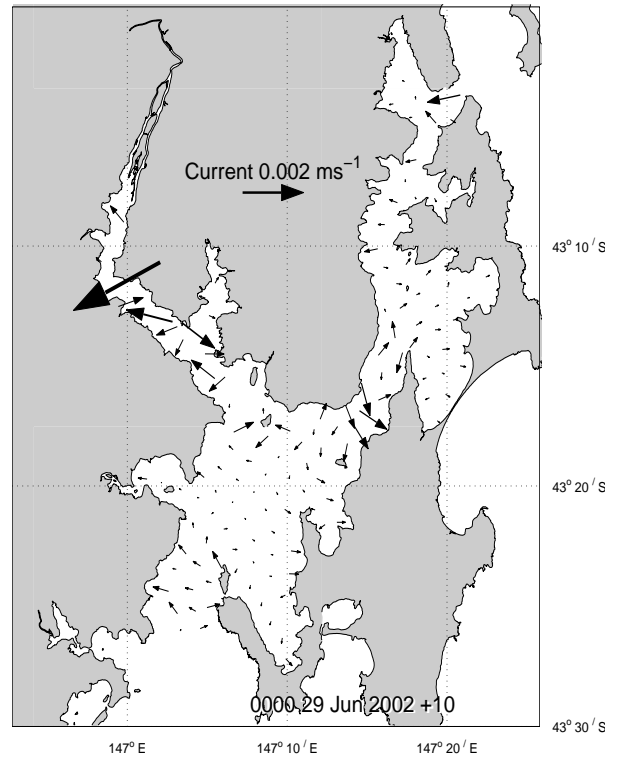
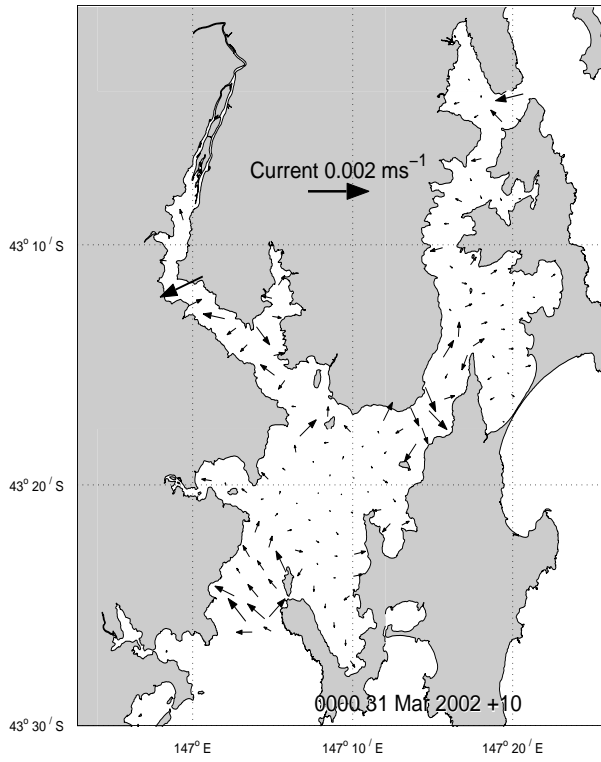


**Fig. 51. Mean Surface Advective Momentum Tendency**

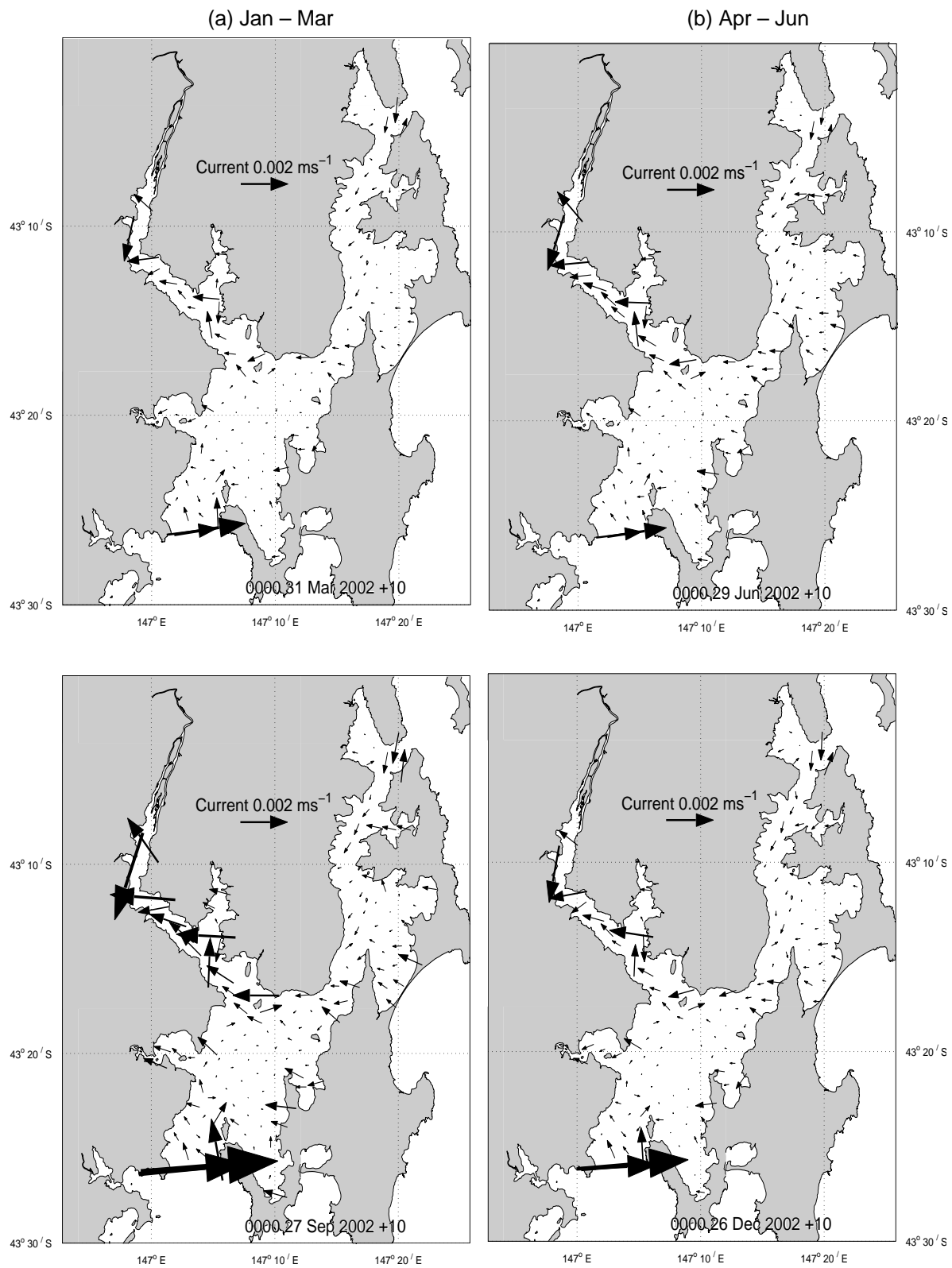


**Fig. 52. Mean Surface Horizontal Diffusion Tendency**

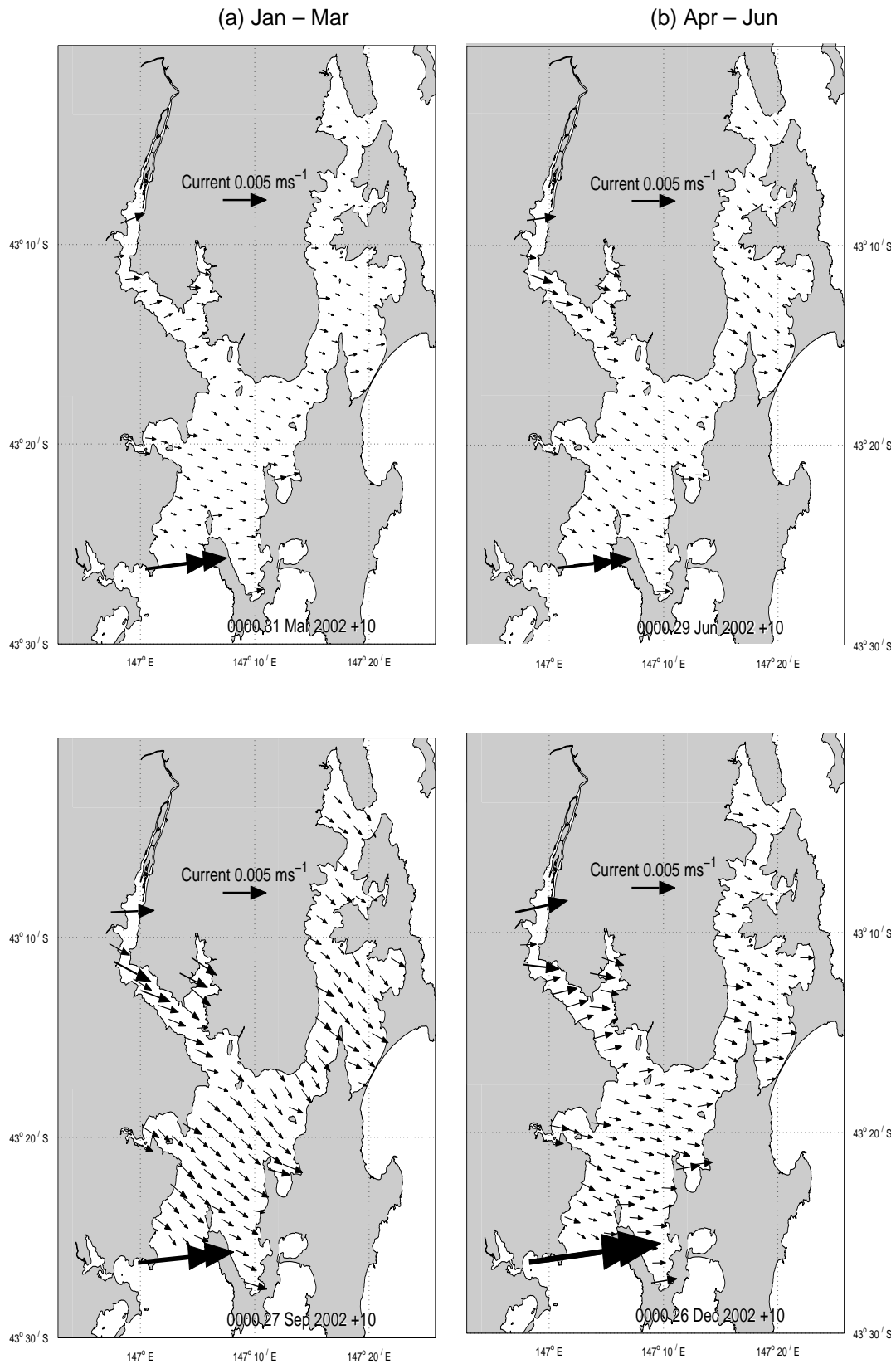


**Fig. 53. Mean Surface Vertical Diffusion Tendency**

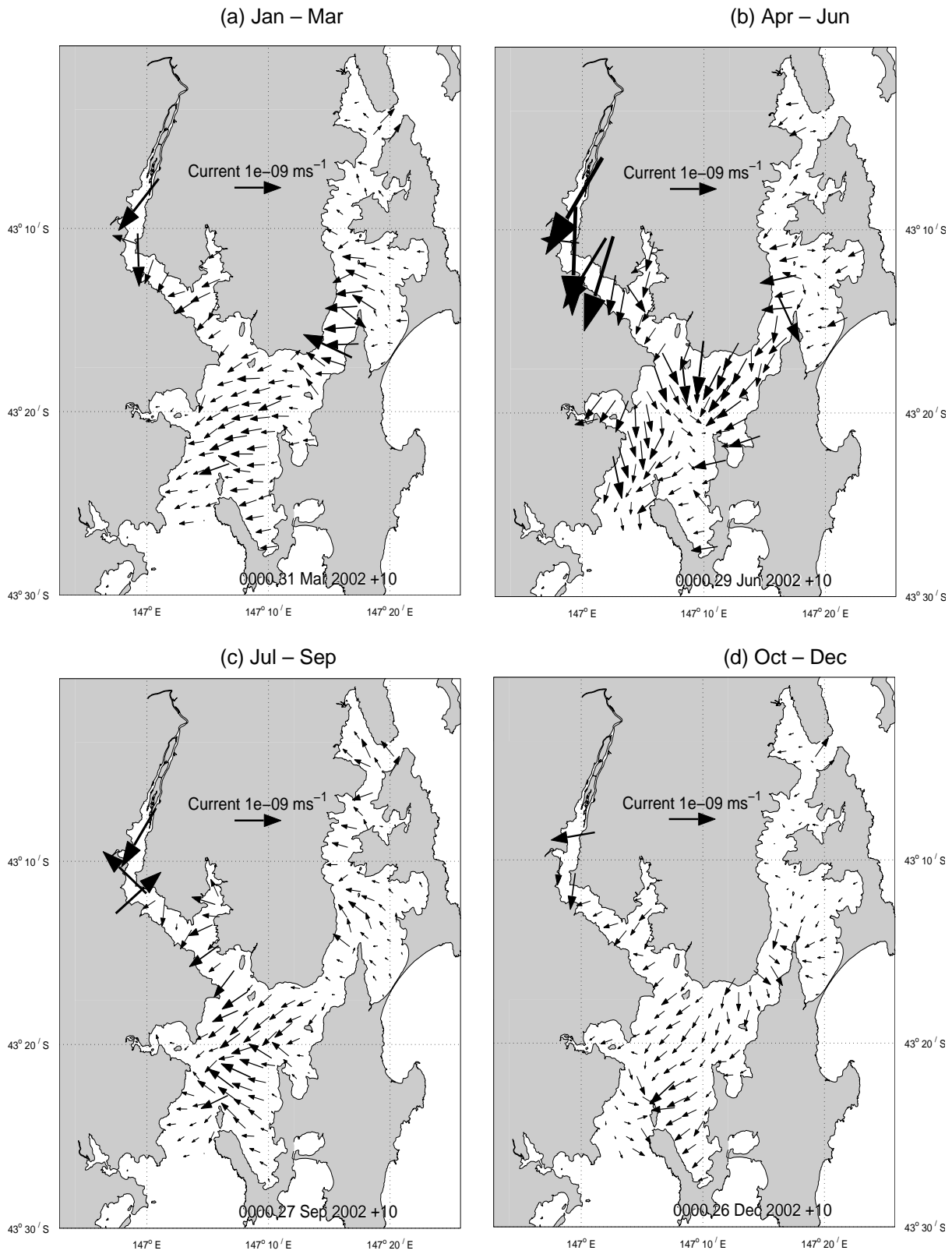


**Fig. 54. Mean Surface Barotropic Pressure Gradient Tendency**

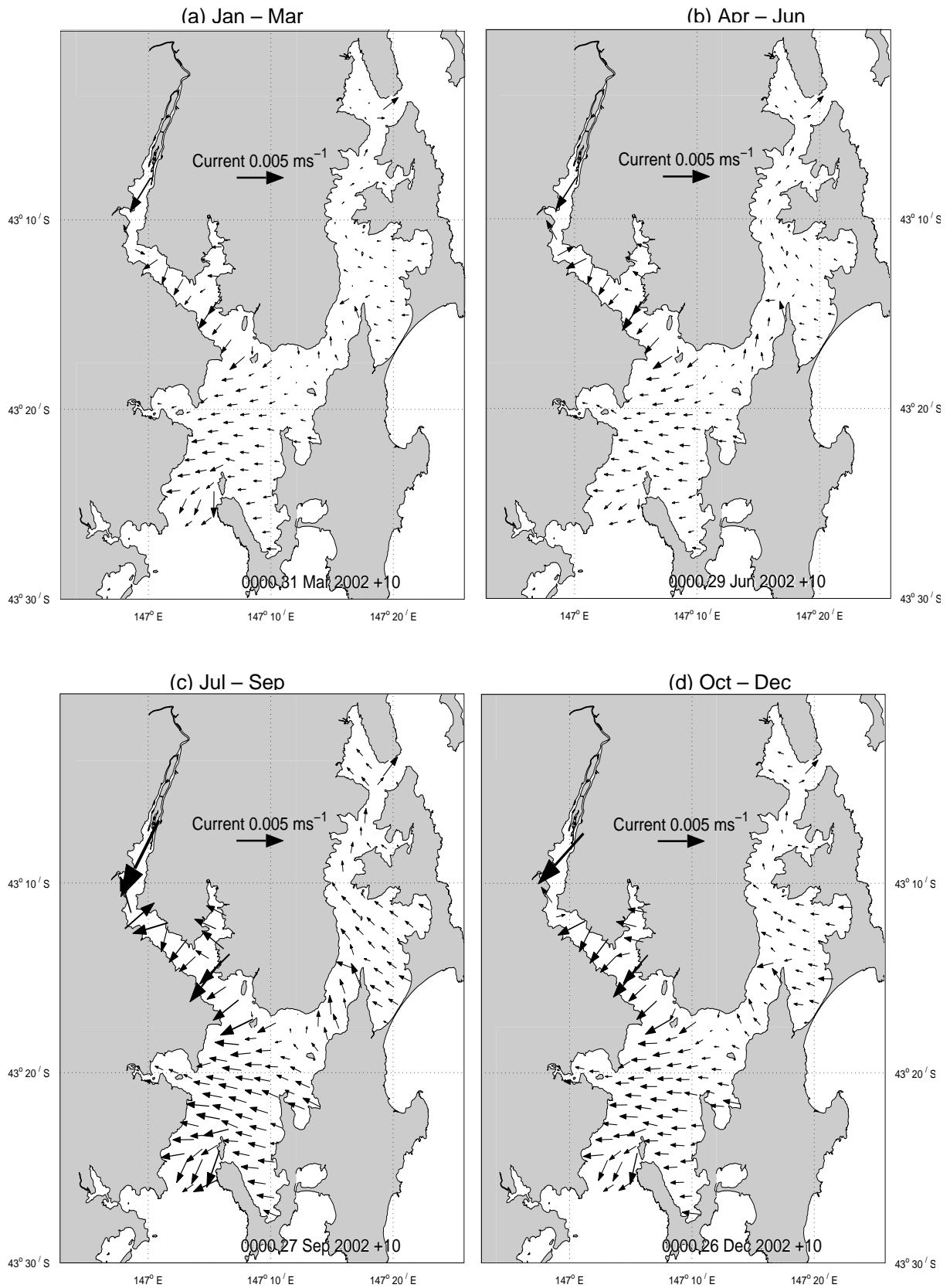


**Fig. 55. Mean Surface Baroclinic Pressure Gradient Tendency**

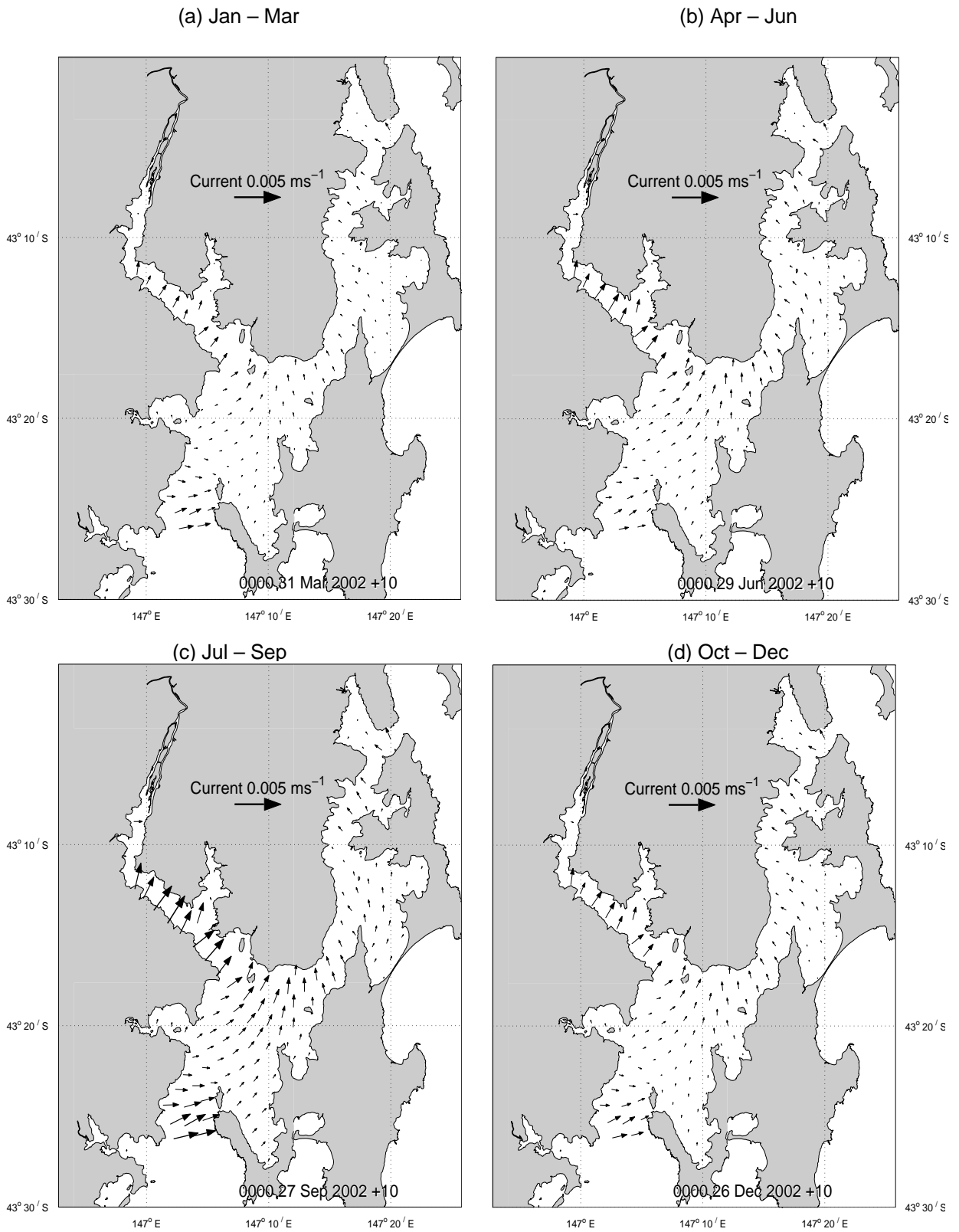


**Fig. 56. Mean Surface Coriolis Tendency**

## 7.5 Flushing Times

Passive tracers were used to obtain an estimate of the flushing characteristics of the estuary. A passive tracer was initialized in a sub-region of the estuary (Fig. 57) with a concentration of 1 and zero elsewhere, and the total mass in this sub-region was calculated throughout the simulation. Full forcing was applied to the domain (i.e. wind, tide, low frequency sea level and temperature / salinity effects) and the tracer distribution was simulated for a fixed period (14 days in this case). The e-folding time for flushing this sub-region is encountered when the total mass was reduced to  $1/e$  (~38%) of the initial mass.

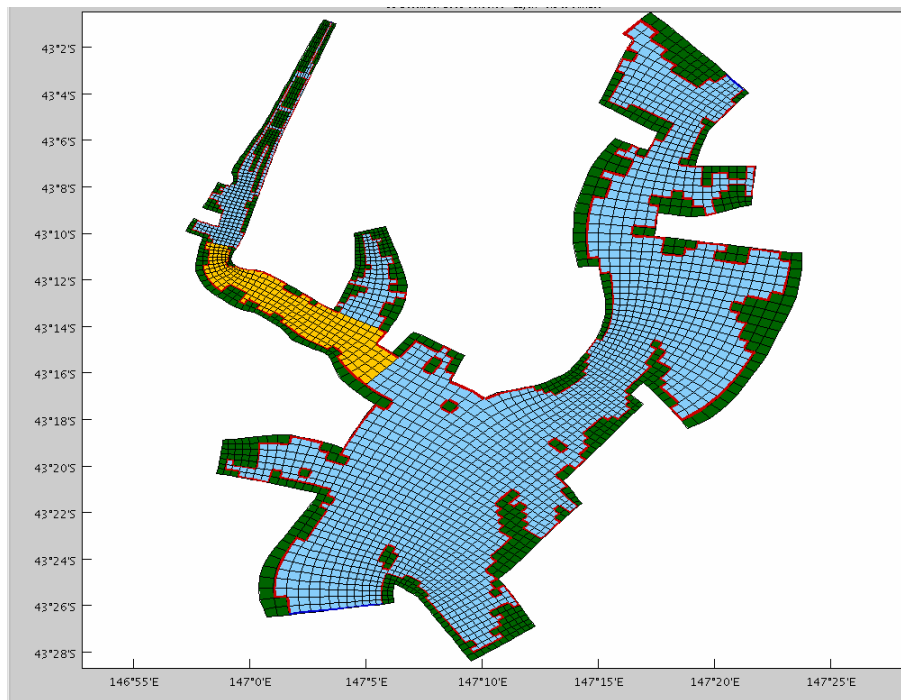


**Fig. 57. Huon flushing region**

Flushing times were calculated for the dates 14 Feb, 15 Apr, 14 Jul and 17 Oct. Time series of the normalized total mass in the sub-region for these times is displayed in Figs 58 to 61 respectively. The general trend of tracer decrease is obtained by fitting a curve to the total mass, from which it can be seen that the e-folding time for this sub-region varies from approximately 3.5 to 9.5 days depending on the magnitude of the Huon River flow, with faster flushing rates for higher flows. The passive tracer distribution in the surface layer at the end of the simulation is shown in Fig. 62 to 65. Maximum surface tracer concentration is found at the head of the estuary after 14 days, with significant concentrations ( $> 0.7$ , i.e. 70% of the original concentration) for low flows. The large flows in October deliver some tracer to the northern end of D'Entrecasteaux Channel.

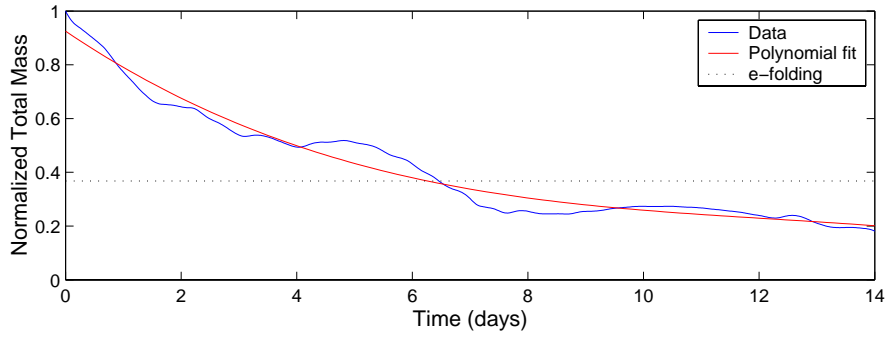


**Fig. 58. Flushing time initiated on 14 Feb 2002; max flow =  $131 \text{ m}^3\text{s}^{-1}$**

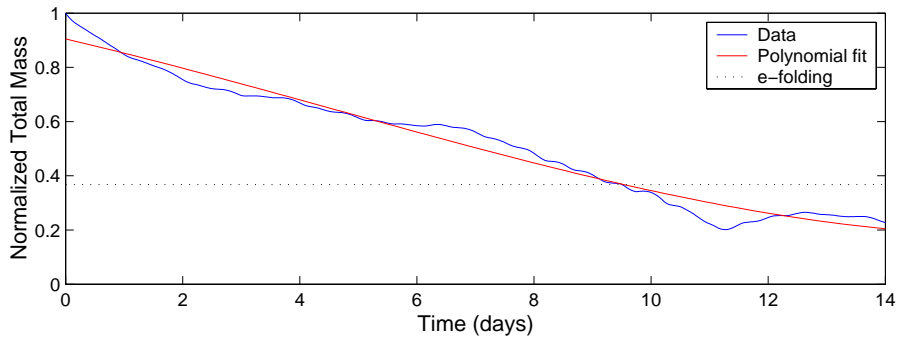


**Fig. 59. Flushing time initiated on 15 Apr 2002; max flow =  $128 \text{ m}^3\text{s}^{-1}$**

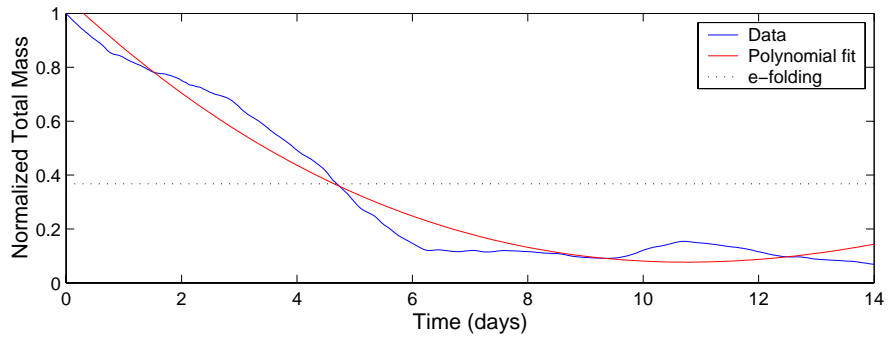


**Fig. 60. Flushing time initiated on 14 Jul 2002; max flow =  $229 \text{ m}^3\text{s}^{-1}$**

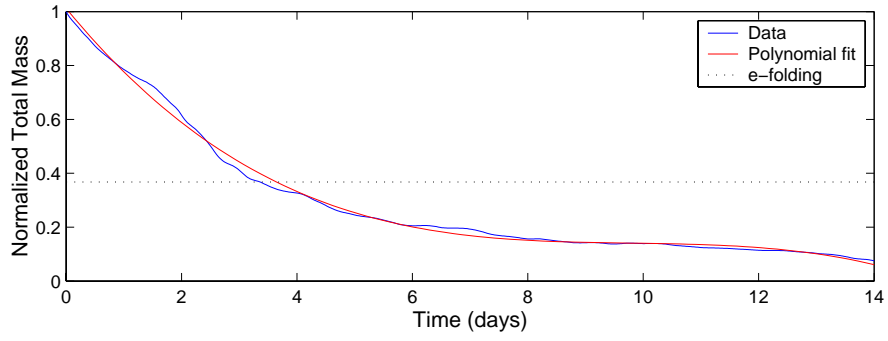


**Fig. 61. Flushing time initiated on 17 Oct 2002; max flow = 537 m<sup>3</sup>s<sup>-1</sup>**

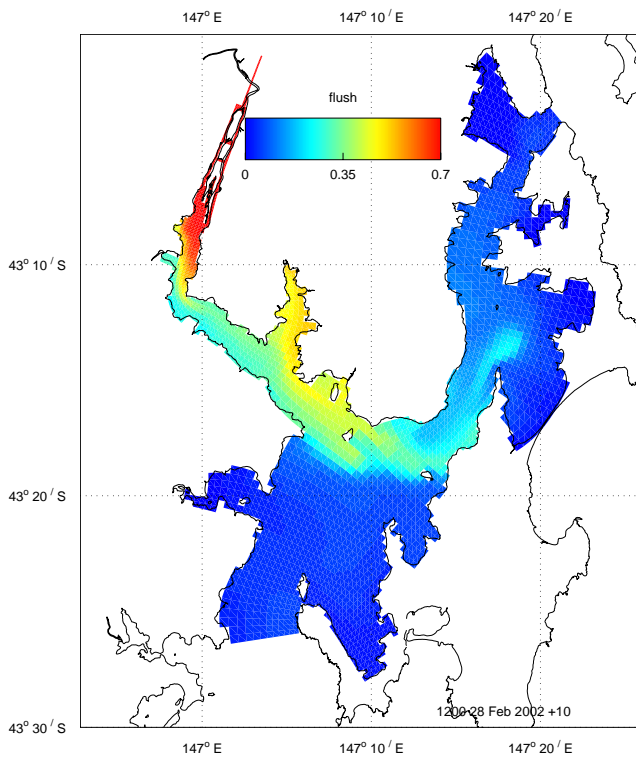


**Fig. 62. Flushing tracer distribution: Feb**

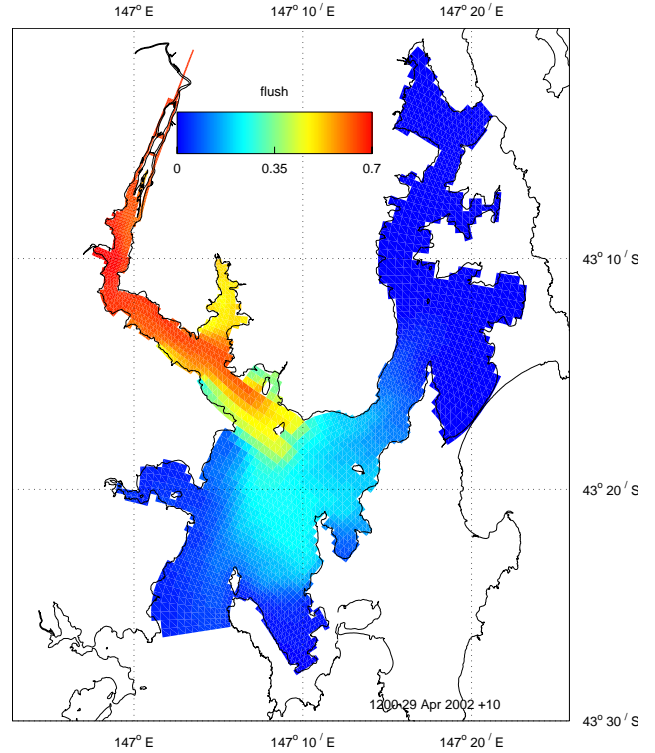


**Fig. 63. Flushing tracer distribution: Apr**

Flushing of the D'Entrecasteaux Channel was estimated by initializing tracer in the sub-region depicted in Fig. 66. Note that this flushing estimate is for the main channel only, excluding the side bays, therefore mass in the flushing region is reduced by advection and mixing through the open boundaries, into the Huon Estuary and into the side bays. Time series for tracer initialization on 14 Feb, 15 Apr, 14 Jul and 17 Oct are displayed in Figs 67 to 70.

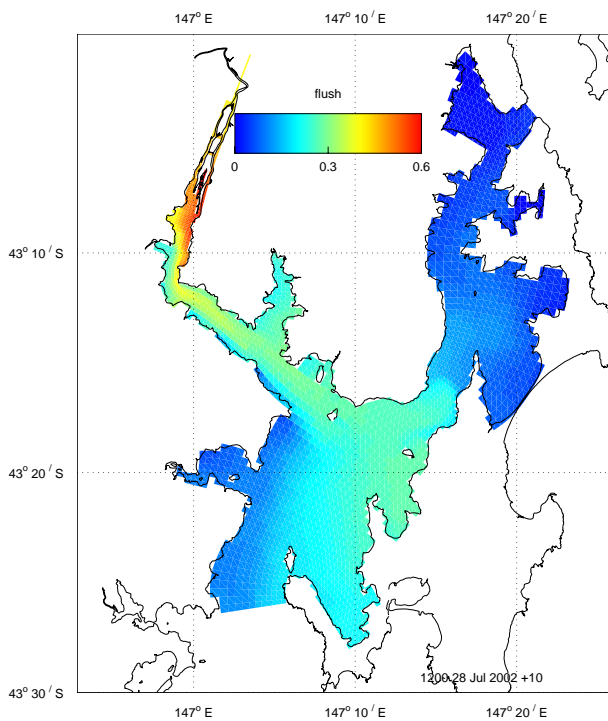


**Fig. 64. Flushing tracer distribution: Jul**

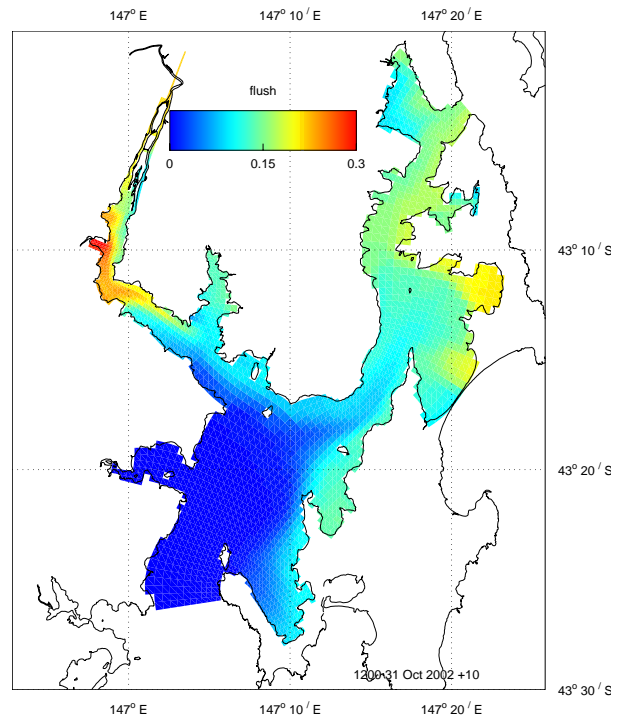


**Fig. 65. Flushing tracer distribution: Oct**

Flushing times for the main channel range from 7.5 days in February to 8.8 in October. Surface concentrations after 14 days of simulation are displayed in Figs 71 to 74. Surface concentration generally is higher (up to 0.7 in April) in the northern end of the channel and remains low in the southern end and upper Huon Estuary. The high flow case (October) results in highest concentrations in the lower Huon.

The open boundary conditions used on the flushing tracer were such that if flow is directed out of the domain, then boundary concentrations are set reflecting advection of tracer having interior values onto the boundary. If flow is directed into the domain, then boundary concentrations are set assuming advection of zero concentration into the domain. Hence if flow is into the domain, mass is decreased since new water (having zero tracer concentration) is brought into the flushing region. Two scenarios were

explored where each open boundary was separately given a zero-flux boundary condition; i.e. no new water is brought into the domain. This allows assessment as to which boundary is responsible for bringing the majority of new water into the flushing region. Time series of normalized total mass during July for the cases when southern and northern boundaries only can bring in new water are displayed in Fig. 75 and 76 respectively. It can be seen that the northern boundary is responsible for little import of new water, with total mass never reaching the e-folding fraction after 14 days. In fact total mass is approaching steady state, indicating that after an initial decrease while tracer is mixed into the side bays and Huon, there is negligible import of new water and this boundary must be associated with mass export. The southern boundary is almost exclusively responsible for bringing in new water with zero concentration tracer, since the flushing time in this case is 8.2 days, only marginally longer than the 8.0 days when both boundaries were open.

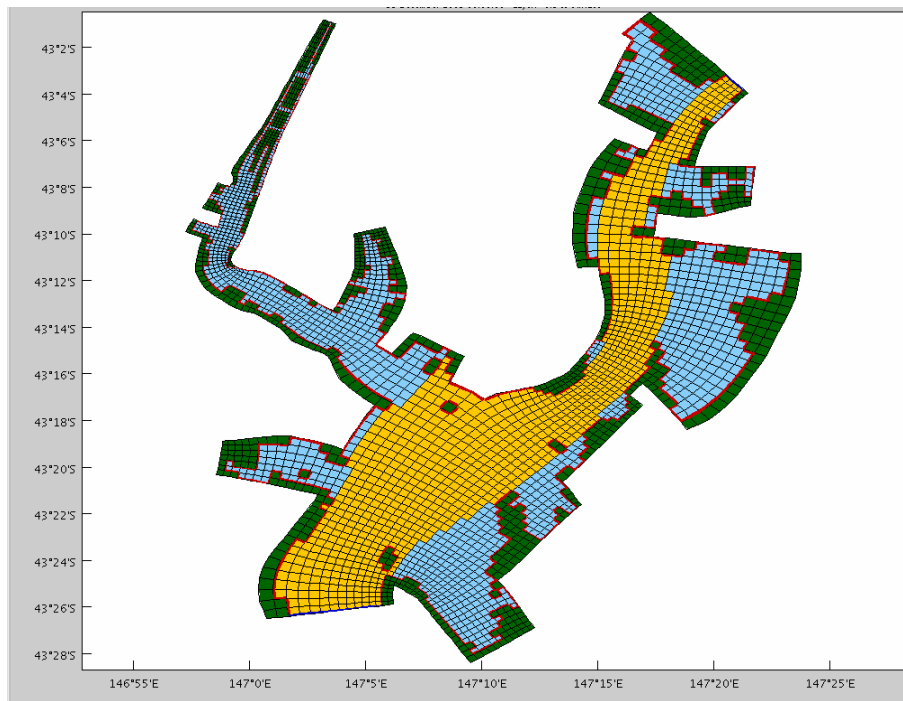


**Fig. 66. D'Entrecasteaux flushing region**

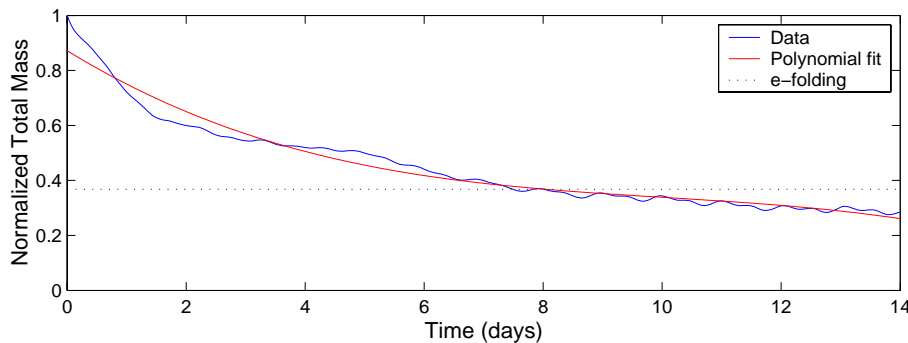


**Fig. 67. Flushing time initiated on 14 Feb 2002; max flow = 131 m<sup>3</sup>s<sup>-1</sup>**

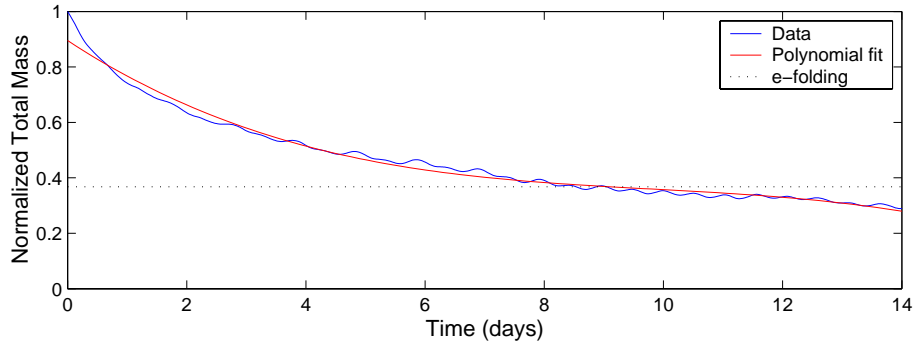


**Fig. 68. Flushing time initiated on 15 Apr 2002; max flow = 128 m<sup>3</sup>s<sup>-1</sup>**

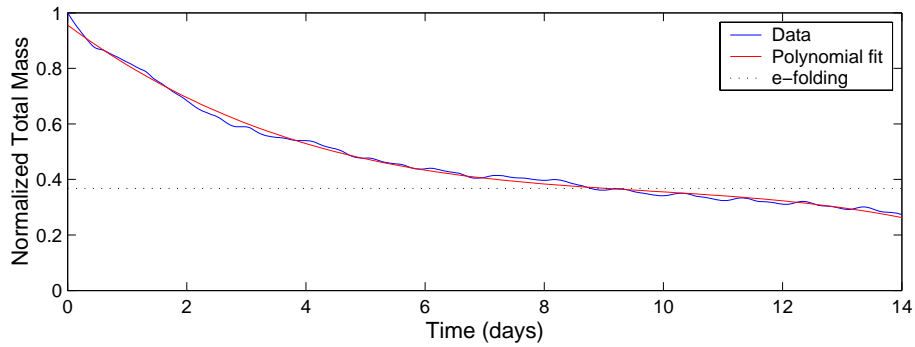


**Fig. 69. Flushing time initiated on 14 Jul 2002; max flow = 229 m<sup>3</sup>s<sup>-1</sup>**

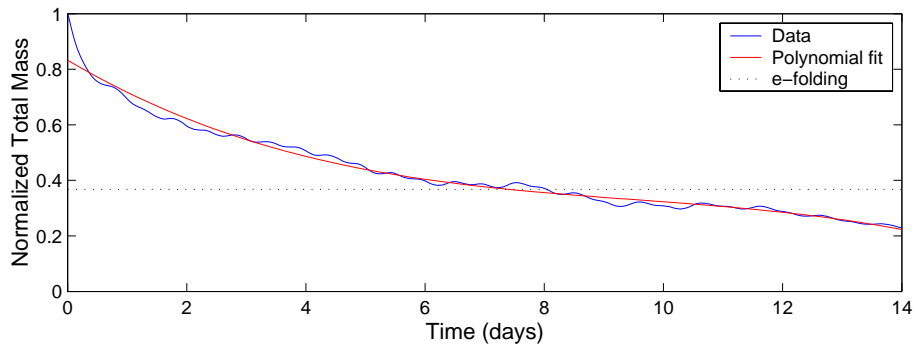


**Fig. 70. Flushing time initiated on 17 Oct 2002; max flow = 537 m<sup>3</sup>s<sup>-1</sup>**

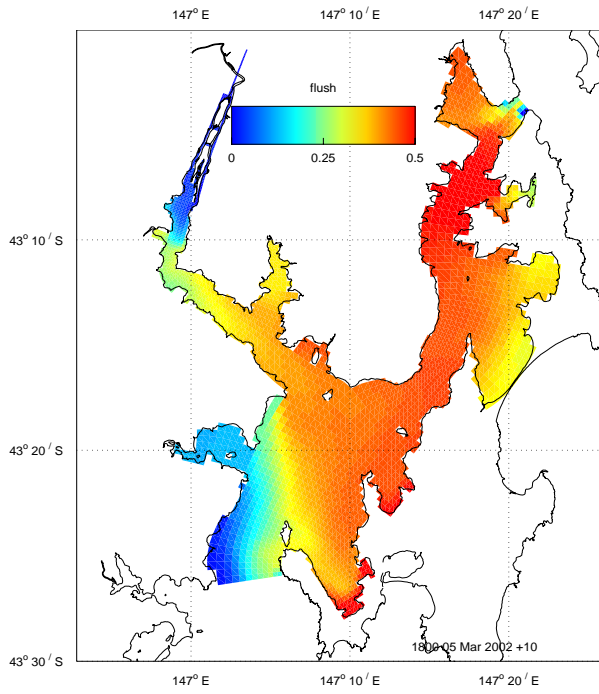


**Fig. 71. Flushing tracer distribution: Feb**

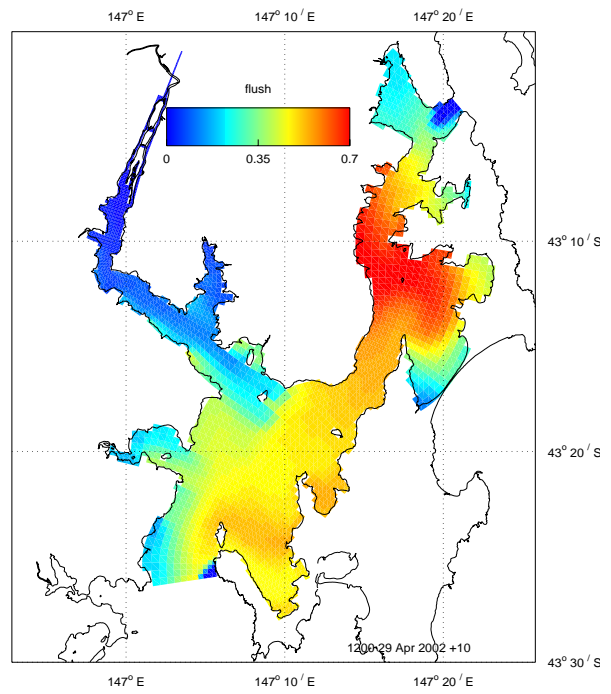


**Fig. 72. Flushing tracer distribution: Apr**

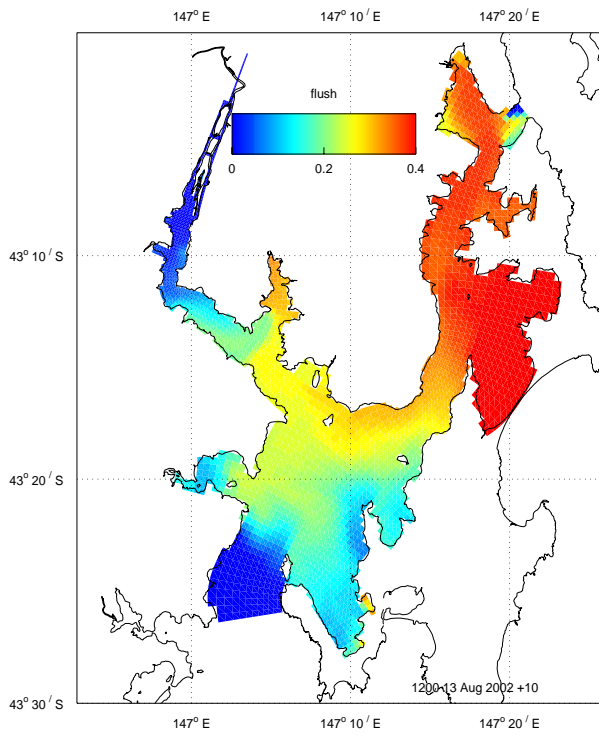


**Fig. 73: Flushing tracer distribution: Jul**

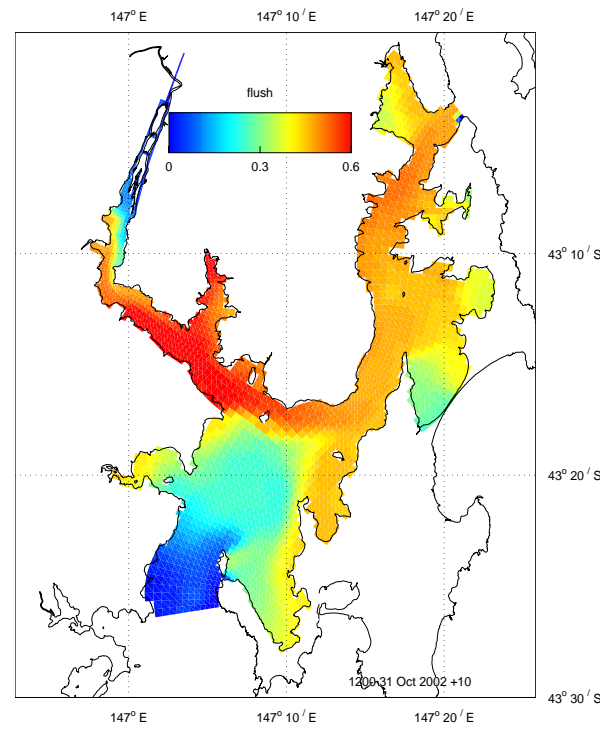


**Fig. 74: Flushing tracer distribution: Oct**

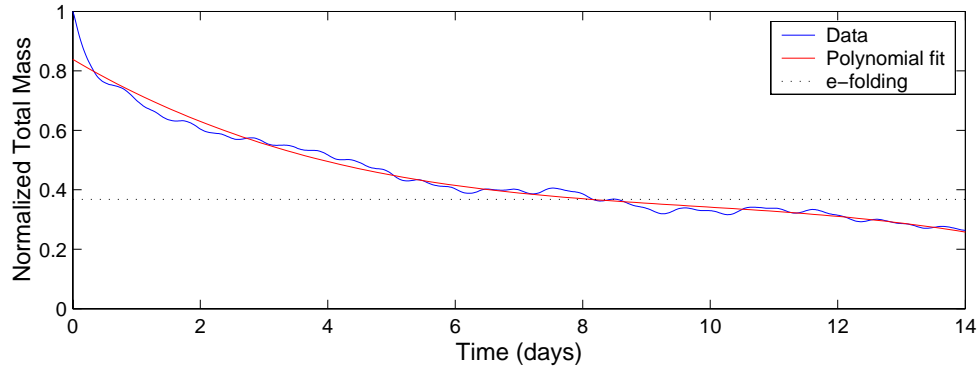


**Fig 75. D’Entrecasteaux flushing through southern boundary only**

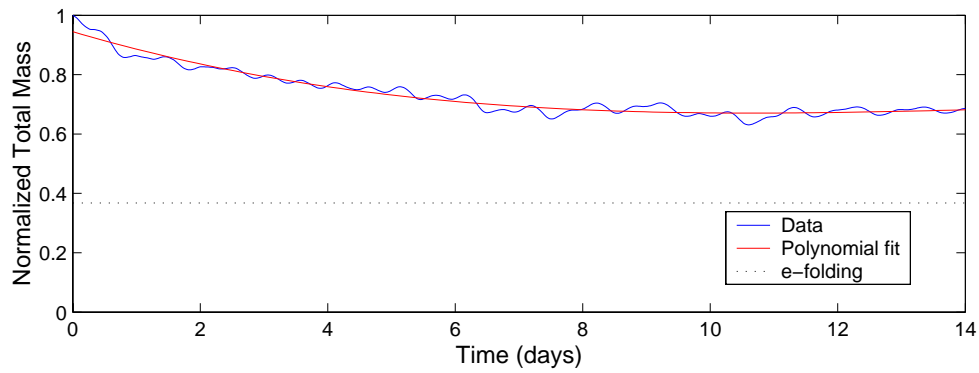


**Fig 76. D’Entrecasteaux flushing through northern boundary only**

The flushing region was set to the complete domain, excluding the upper reaches of the Huon Estuary (Fig. 77a). Time series of normalized total mass during July is displayed in Fig. 77b, and the surface concentration after 30 days in Fig. 77c. Flushing time in this case is 19.8 days. Maximum surface concentrations are approximately 0.8 in Great Bay after 30 days. Minimum concentrations are in the lower D’Entrecasteaux Channel and Huon Estuary. The northern Channel generally contains tracer with higher concentration than the lower, due to the southern boundary being the major supplier of new water.

Similar flushing experiments were conducted from all major side bays in the D’Entrecasteaux for July 2002 only. Although flushing times are expected to vary at other times of the year, this provides a relative comparison of various regions in the D’Entrecasteaux. Results are presented in Figs 78 to 85 and summarized in Table 6. North West Bay resulted in the shortest flushing time of 5 days for this time period, and Barnes Bay the longest with 10.3 days.

**Table 6. Summary of flushing times for major side bays**

Region	Date	River Flow (m <sup>3</sup> s <sup>-1</sup> )	Flushing Time (days)
Lower Huon Estuary	Feb 2002	131	6.5
Lower Huon Estuary	Apr 2002	128	9.5
Lower Huon Estuary	Jul 2002	229	4.7
Lower Huon Estuary	Oct 2002	537	3.4
Main D'Ent Channel	Feb 2002	131	7.5
Main D'Ent Channel	Apr 2002	128	8.5
Main D'Ent Channel	Jul 2002	229	8.0
Main D'Ent Channel	Oct 2002	537	8.8
Whole domain	Jul 2002	229	19.8
NWB	Jul 2002	229	5.0
Port Esperance	Jul 2002	229	5.1
Barnes Bay	Jul 2002	229	10.3
Great Bay	Jul 2002	229	7.4
Isthmus Bay	Jul 2002	229	9.5
Little Taylors Bay	Jul 2002	229	6.3
Great Taylors Bay	Jul 2002	229	6.9
Isthmus + Great Bays	Jul 2002	229	13.6

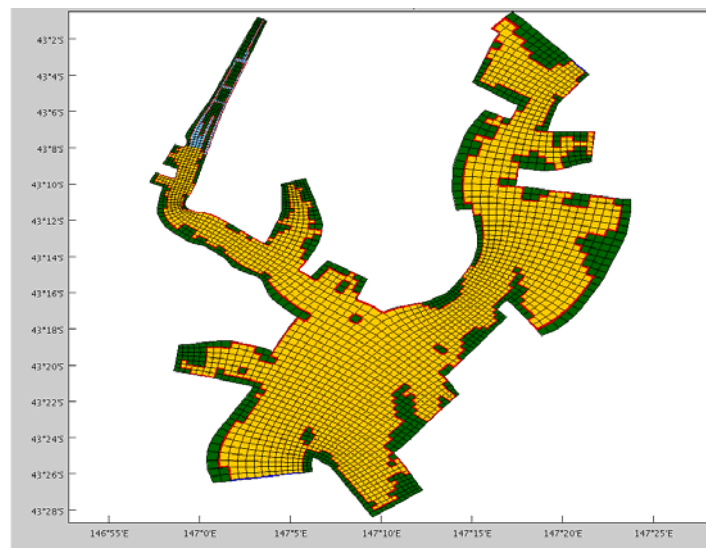


**Fig 77(a). D'Entrecasteaux – Huon flushing region**

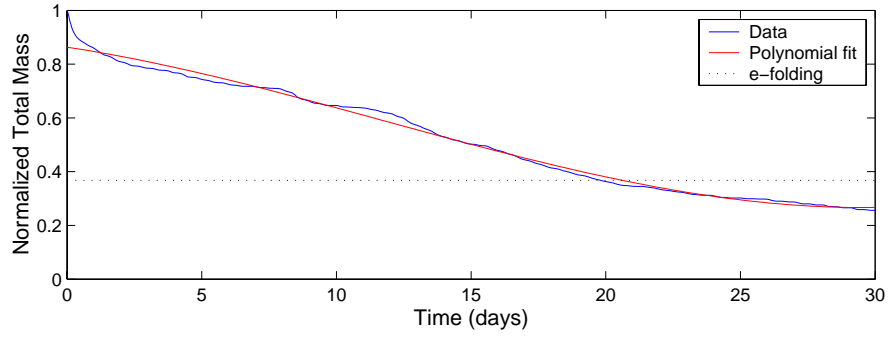


**Fig. 77(b). Flushing time initiated on 14 Jul 2002; max flow =  $229 \text{ m}^3\text{s}^{-1}$**

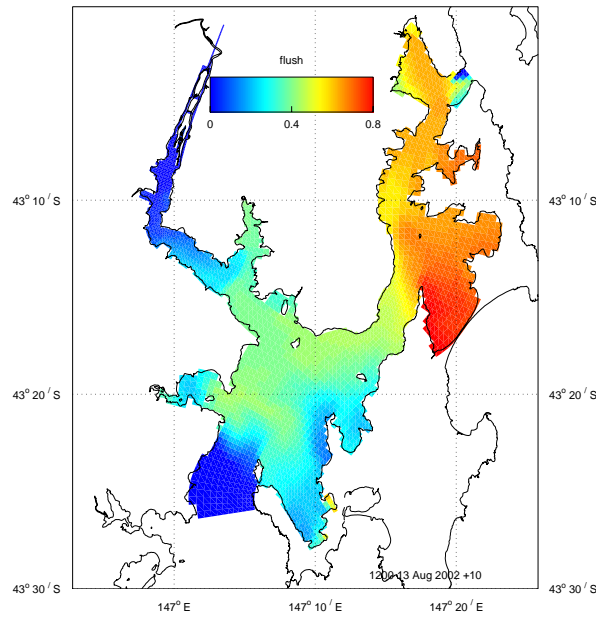


**Fig. 77(c). D'Entrecasteaux Channel – Huon flushing tracer distribution: Jul**

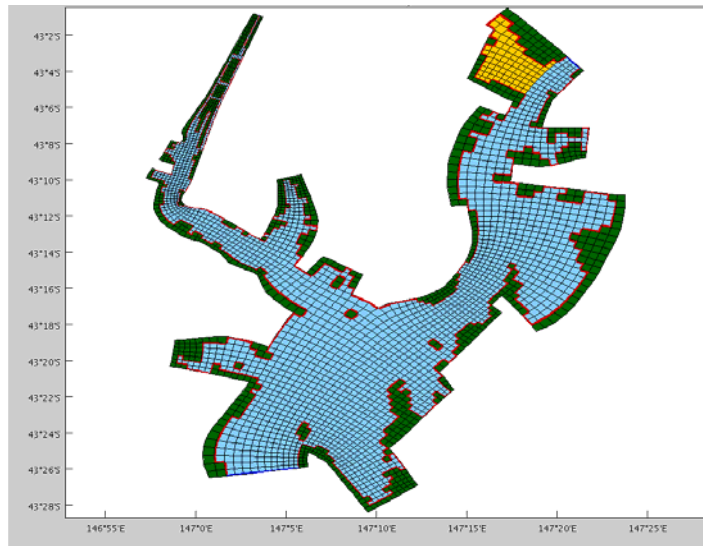


**Fig. 78(a). North West Bay flushing region**

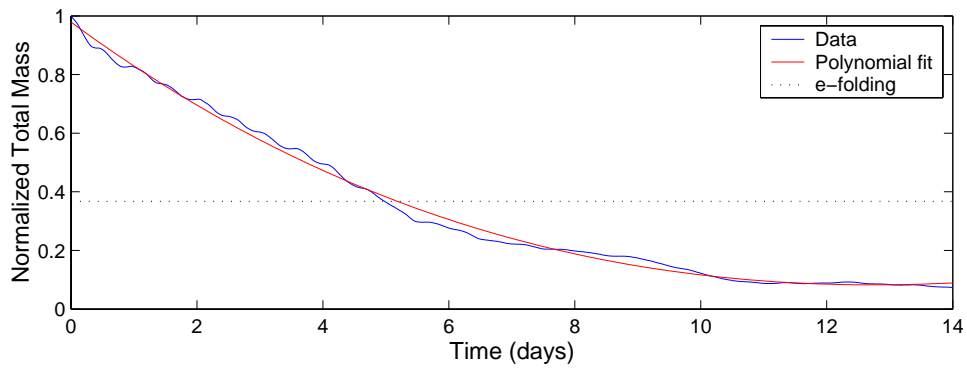


**Fig. 78(b). Flushing time initiated on 14 Jul 2002; ; max flow = 229 m<sup>3</sup>s<sup>-1</sup>**

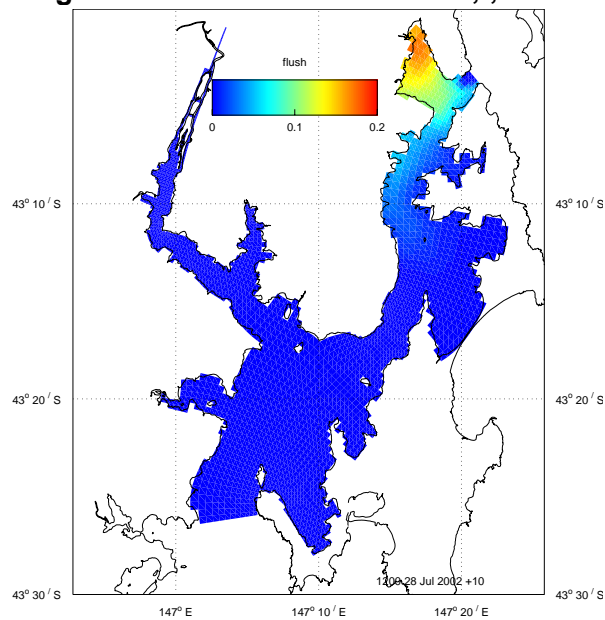


**Fig. 78(c). North West Bay flushing tracer distribution: July**

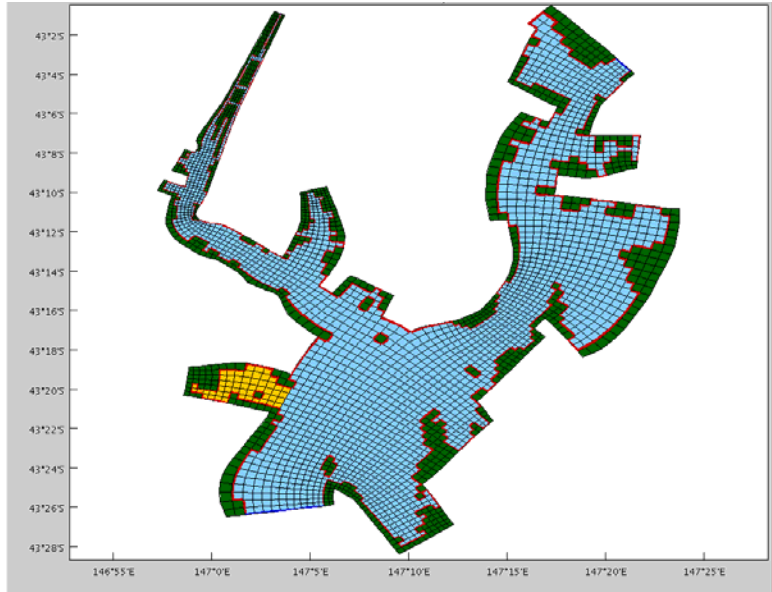


**Fig. 79(a). Port Esperance Bay flushing region**

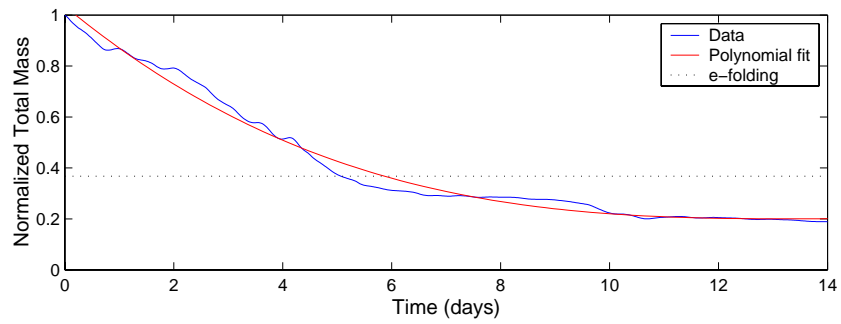


**Fig. 79(b). Flushing time initiated on 14 Jul 2002; max flow =  $229 \text{ m}^3 \text{ s}^{-1}$**

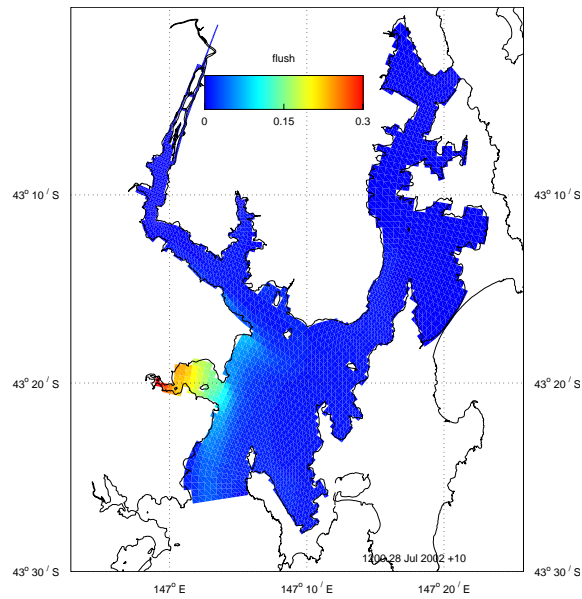


**Fig. 79(c). Port Esperance Bay flushing tracer distribution: Jul**

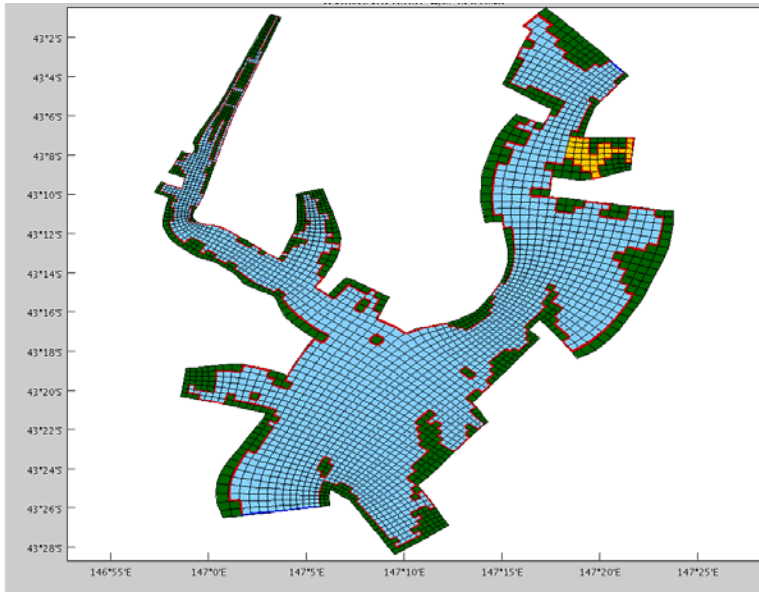


**Fig. 80(a). Barnes Bay flushing region**

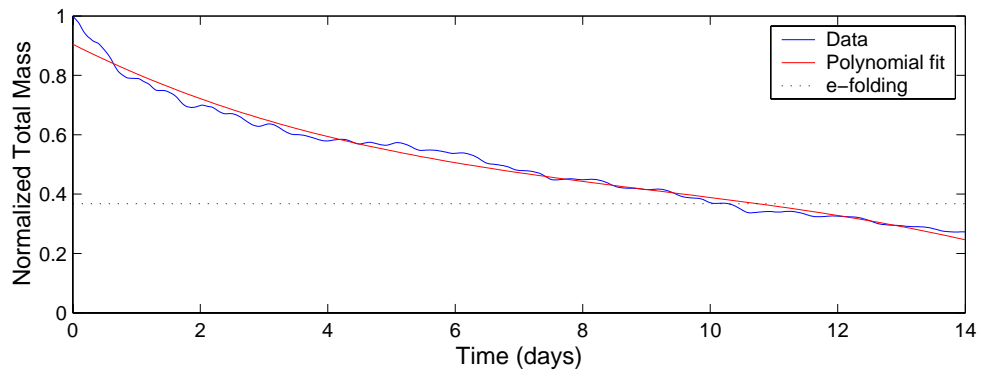


**Fig. 80(b). Flushing time initiated on 14 Jul 2002; max flow =  $229 \text{ m}^3\text{s}^{-1}$**

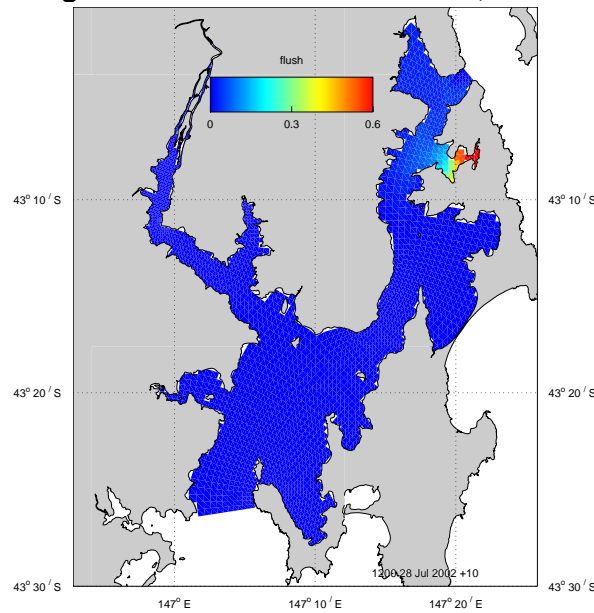


**Fig. 80(c). Barnes Bay flushing tracer distribution: Jul**

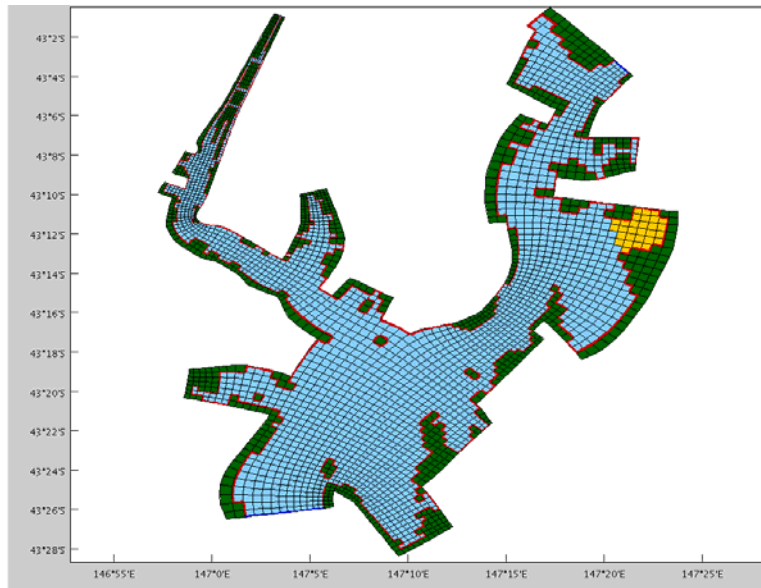


**Fig. 81(a). Great Bay flushing region**

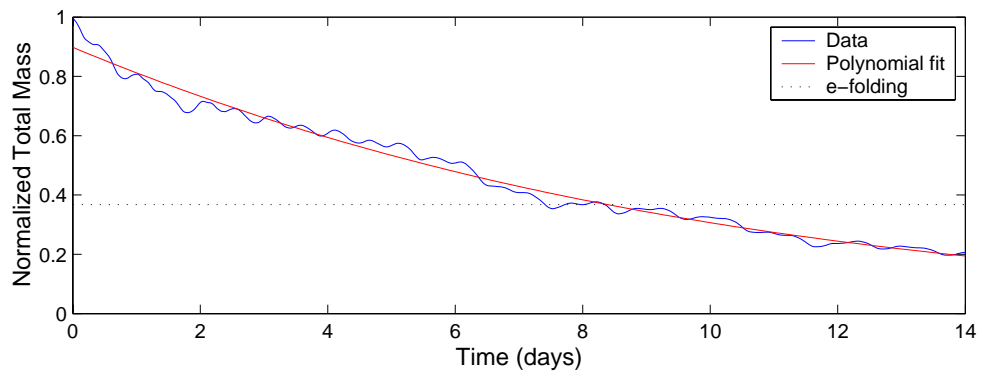


**Fig. 81(b). Flushing time initiated on 14 Jul 2002; max flow =  $229 \text{ m}^3 \text{ s}^{-1}$**

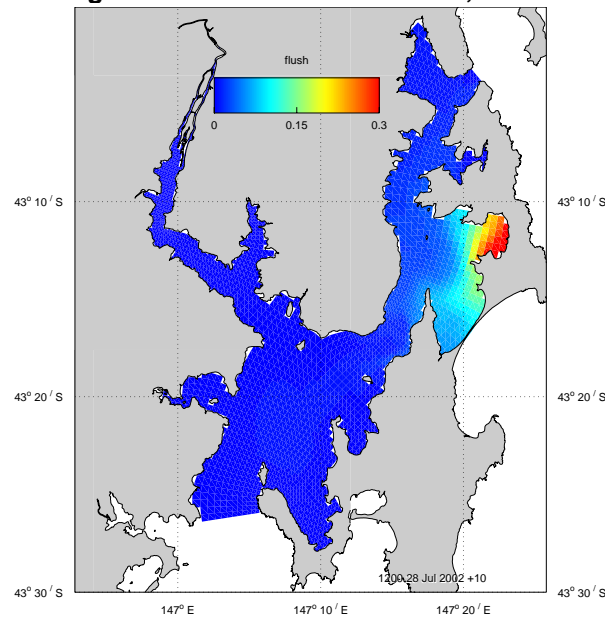


**Fig. 81(c). Great Bay flushing tracer distribution: Jul**

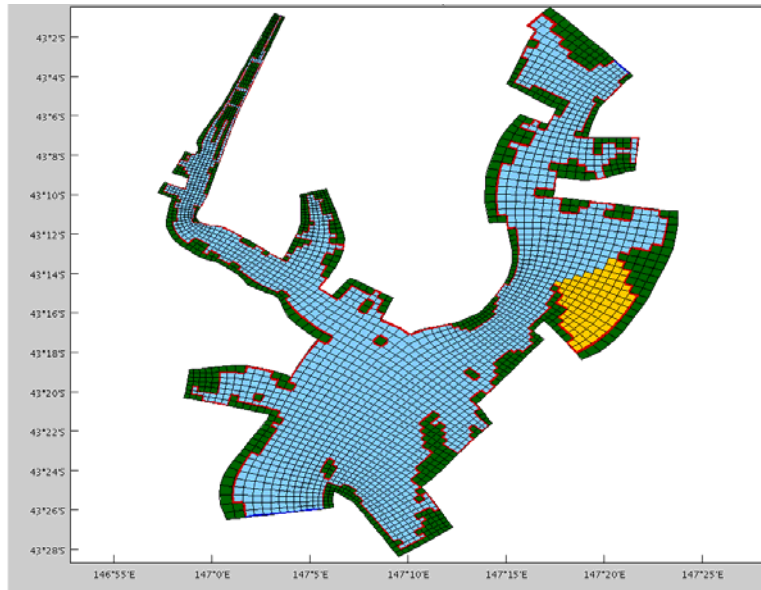


**Fig. 82(a). Isthmus Bay flushing region**

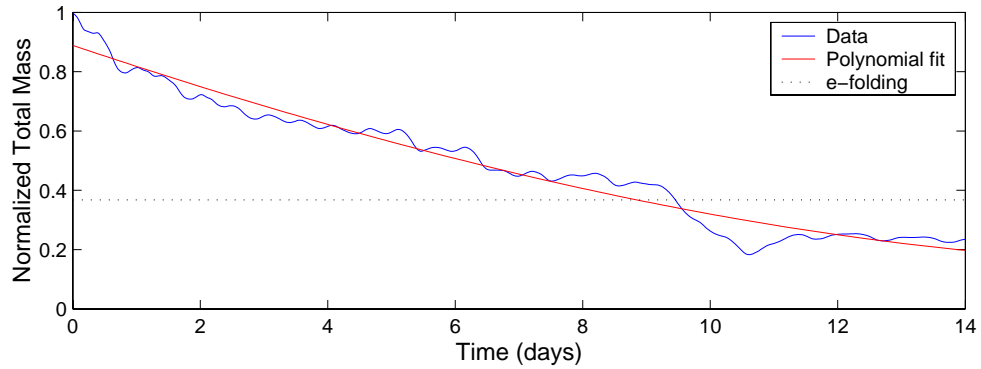


**Fig. 82(b). Flushing time initiated on 14 Jul 2002; max flow = 229 m<sup>3</sup>s<sup>-1</sup>**

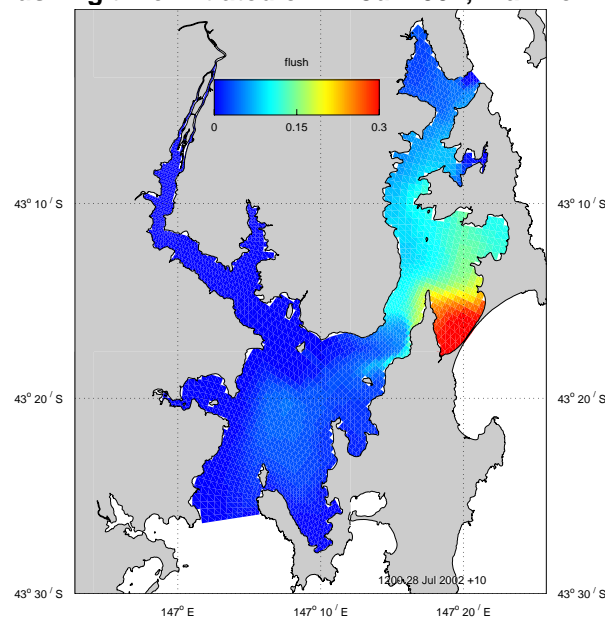


**Fig. 82(c). Isthmus Bay flushing tracer distribution: Jul**

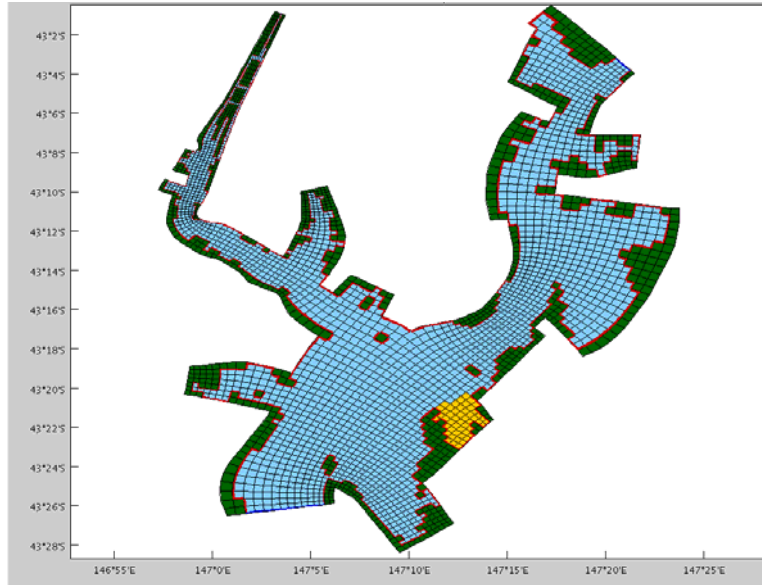


**Fig. 83(a). Little Taylors Bay flushing region**

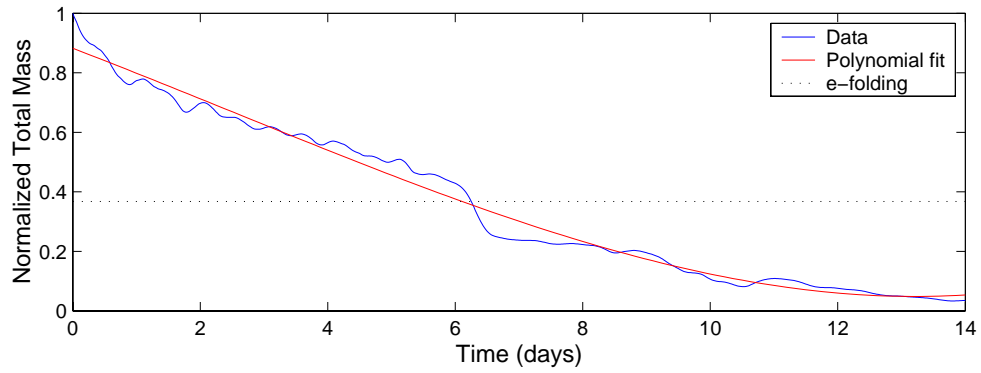


**Fig. 83(b). Flushing time initiated on 14 Jul 2002; max flow = 229 m<sup>3</sup>s<sup>-1</sup>**

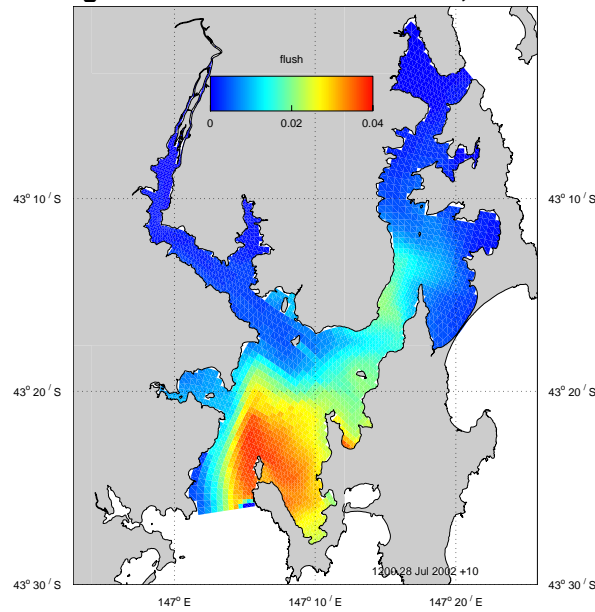


**Fig. 83(c). Little Taylors Bay flushing tracer distribution: Jul**

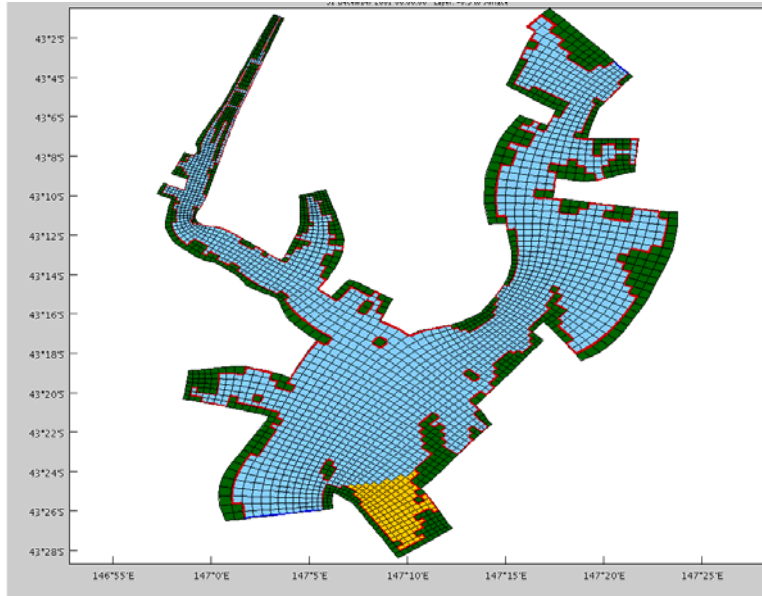


**Fig. 84(a). Great Taylors Bay flushing region**

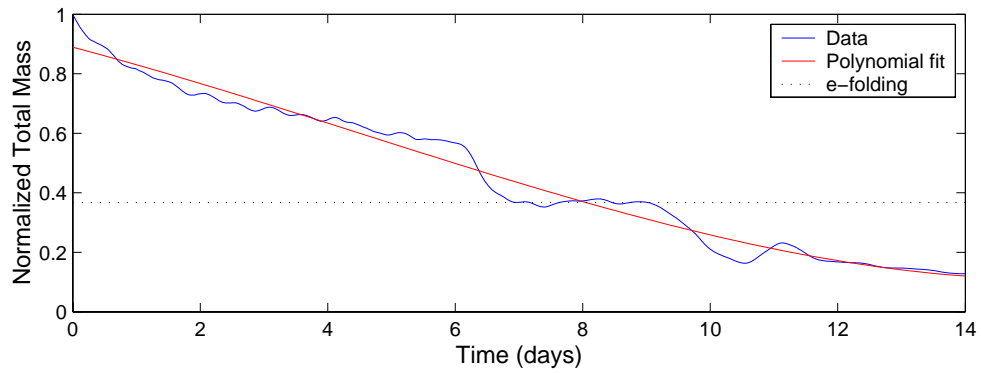


**Fig. 84(b). Flushing time initiated on 14 Jul 2002; max flow =  $229 \text{ m}^3 \text{ s}^{-1}$**

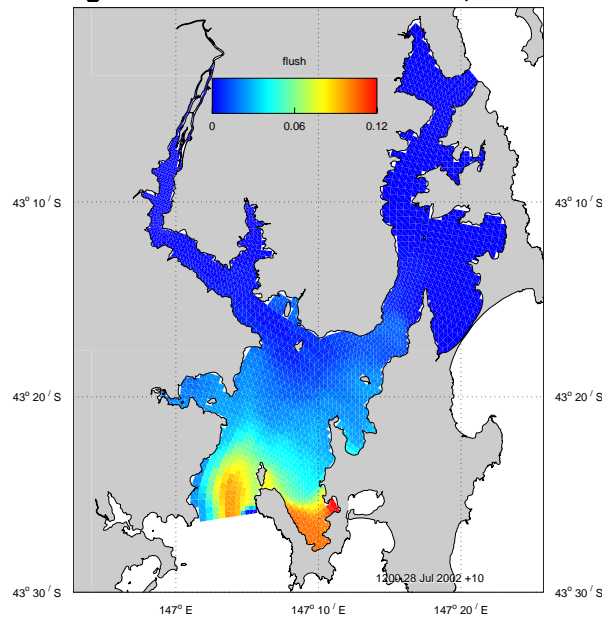


**Fig. 84(c). Great Taylors Bay flushing tracer distribution: Jul**

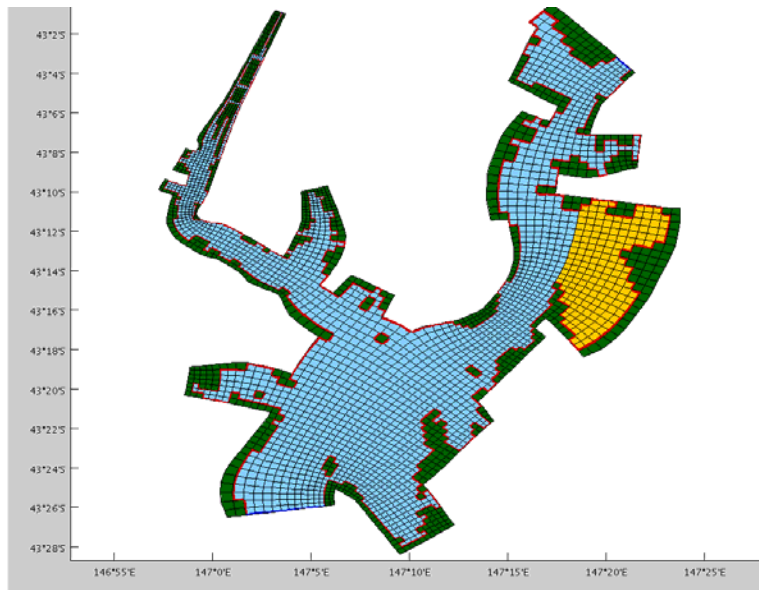


**Fig. 85(a). Isthmus + Great Bay flushing region**

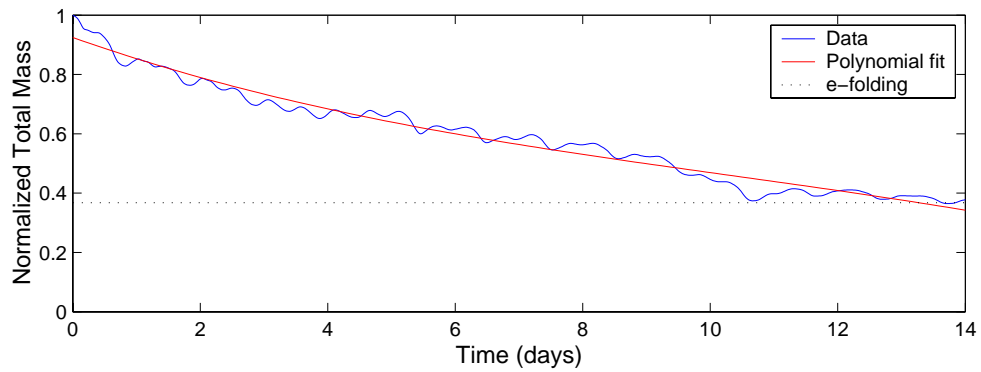


**Fig. 85(b). Flushing time initiated on 14 Jul 2002; max flow =  $229 \text{ m}^3 \text{ s}^{-1}$**

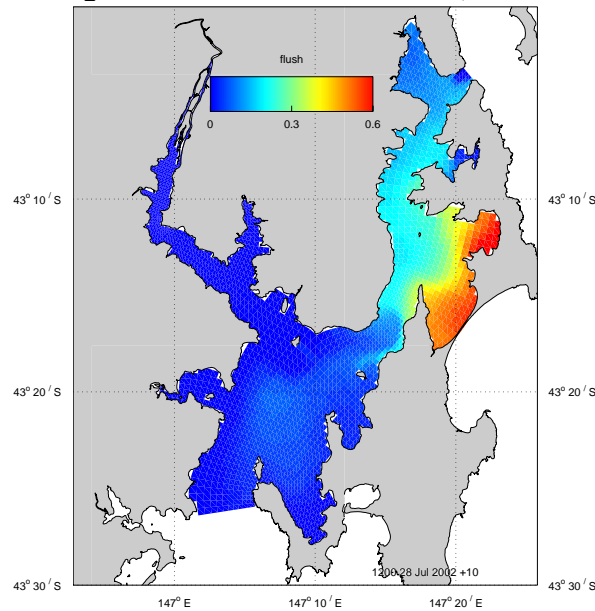


**Fig. 85(c). Isthmus + Great Bay flushing tracer distribution: Jul**

## 7.6 Residual Flow

Residual, or mean/net, flow is the long term circulation the system experiences, and contributes towards flushing the region and distributing tracers input from the open ocean throughout the system. In this case the seasonal residual was calculated by averaging the velocities from every time-step over a 90 day period. Surface and bottom mean flow for each season are displayed in Figs 86 to 89 and 90 to 93 respectively.

Surface residual currents are directed down-river in the Huon Estuary during all seasons, with maximum speeds of up to approximately  $0.2 \text{ ms}^{-1}$  in the winter and spring when rainfall (hence river flow) is greatest. This river flow enters the channel and flows predominantly up-channel towards the north. Some flow is observed down-channel to the southern boundary.

The bottom flow is strongly directed into the domain at the southern boundary and continues northward towards the Huon Estuary mouth. Here the flow splits with the majority of water continuing upstream into the Huon Estuary along the southern bank, a smaller secondary bottom flow continuing through the narrowest point of the channel past Gordon into Isthmus Bay and a smaller still recirculation heading south into Great Taylor Bay (Fig. 94). Further up the Huon Estuary bottom flow is directed down-river. At the northern end of the D'Entrecasteaux Channel bottom flow is directed down-channel and into North West Bay. Away from the southern boundary bottom velocities are generally quite weak throughout the domain, of the order of  $1 \text{ cms}^{-1}$ .

The conceptual model of residual flow for the D'Entrecasteaux – Huon Estuary system is as follows: flow enters the region in bottom water at the southern end of the channel and continues along the bottom and upstream into the Huon Estuary in the salt wedge, favouring the southern bank. Entrainment occurs from the salt wedge into the downstream freshwater flow, the majority of which then turns north upon entering the channel and exits into Storm Bay at the northern end of the channel. A smaller proportion of Huon flow exits the southern channel.

The momentum balance analysis of Section 7.4 concluded that the surface residual flow is predominantly the result of density gradient forces, wind and effects of rotation. Horizontal and vertical friction becomes important in the bottom waters. A schematic of the residual flow is presented in Fig. 95.

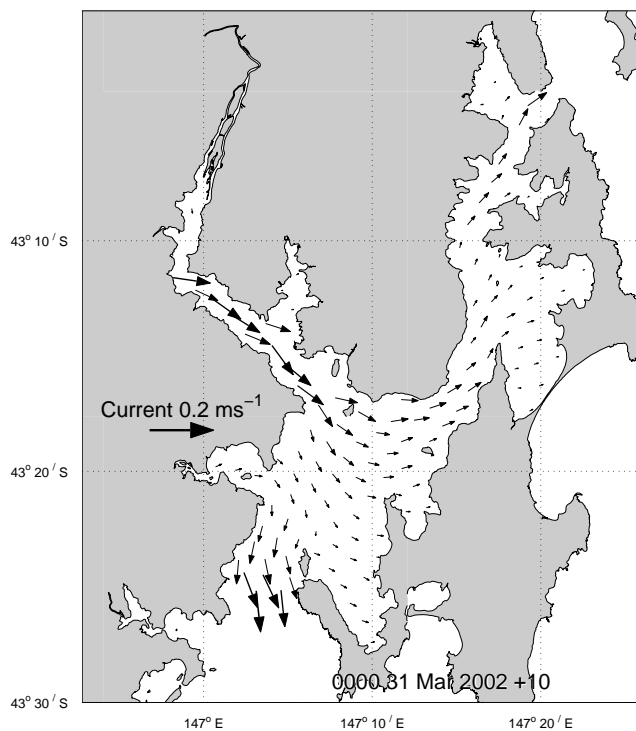


**Fig. 86: Surface mean flow, summer**

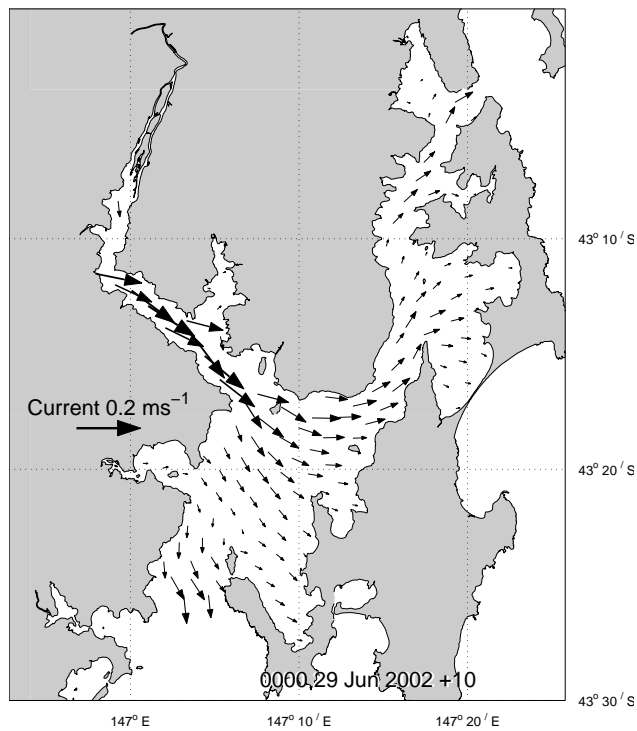


**Fig. 87: Surface mean flow, autumn**

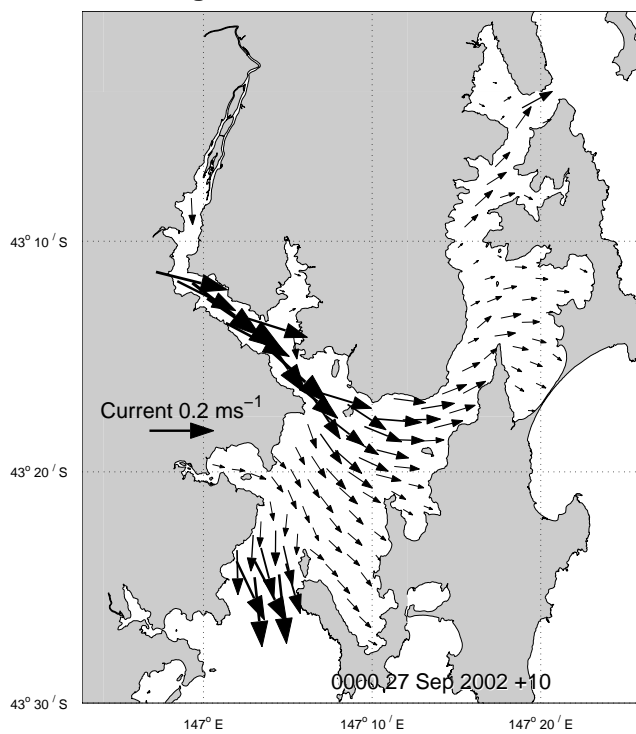


**Fig. 88: Surface mean flow, winter**

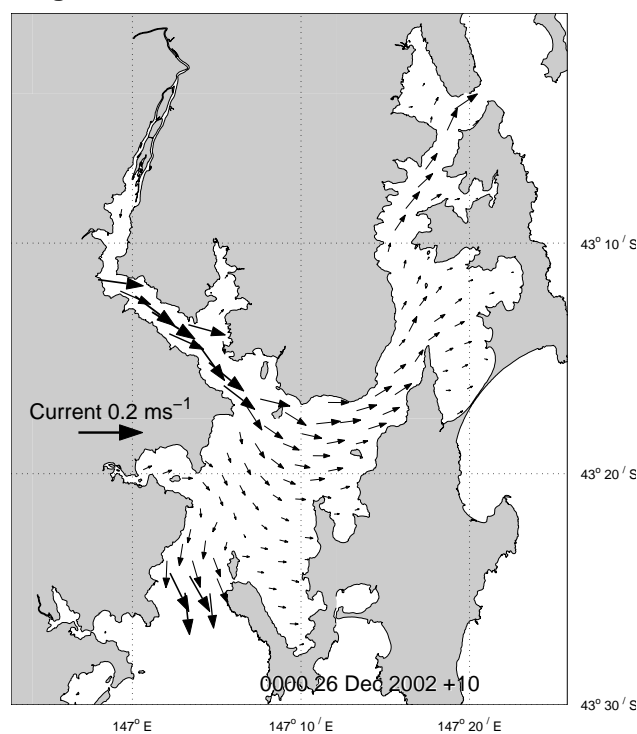


**Fig. 89 Surface mean flow, spring**

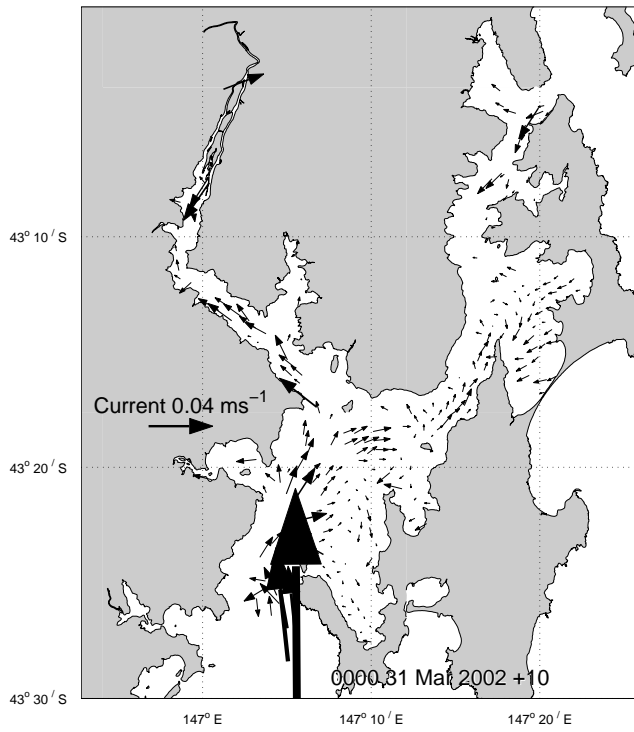


**Fig. 90: Bottom mean flow, summer**

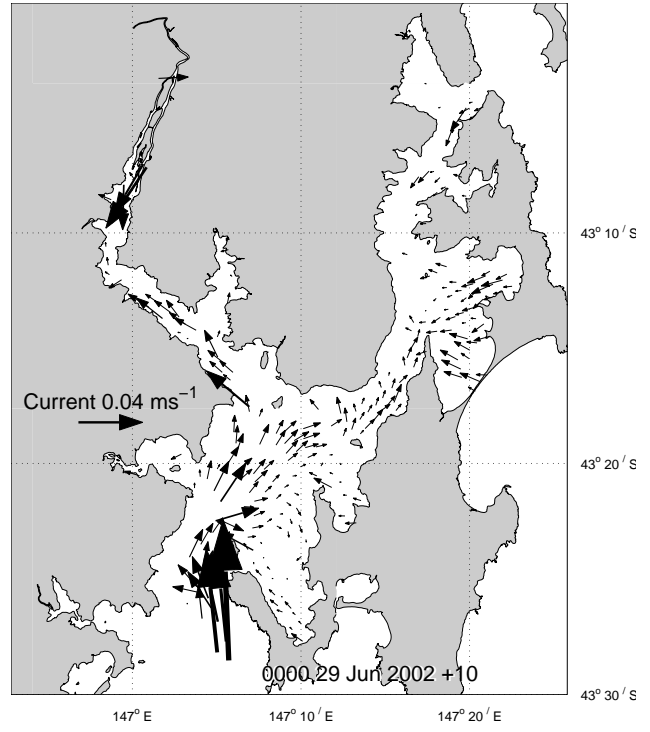


**Fig. 91: Bottom mean flow, autumn**

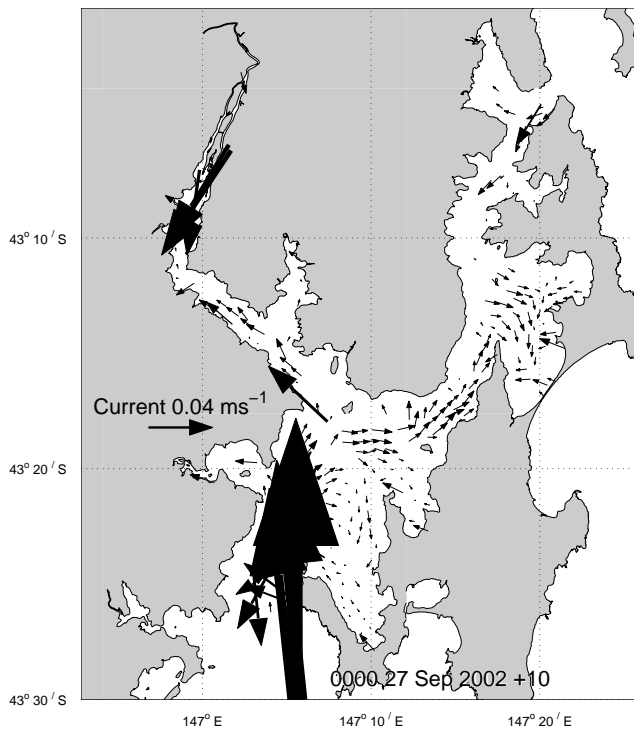


**Fig. 92: Bottom mean flow, winter**

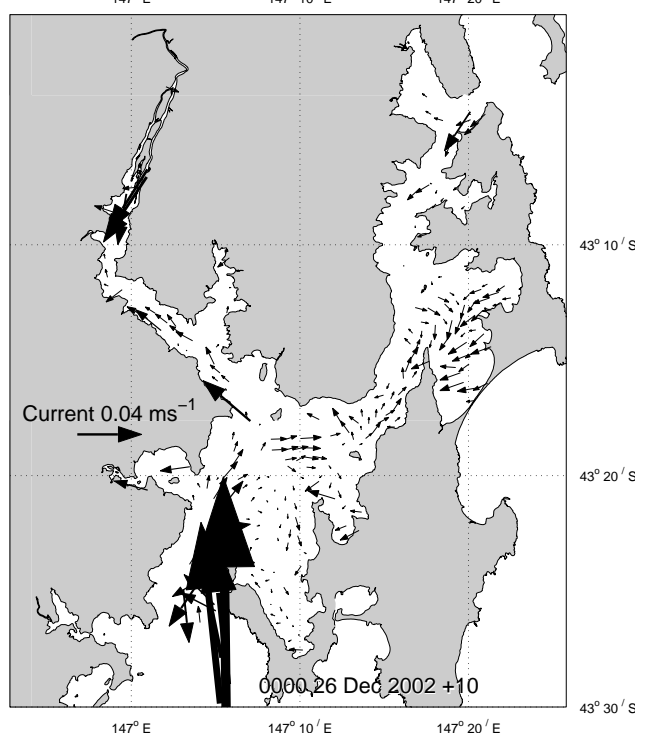


**Fig. 93: Bottom mean flow, spring**

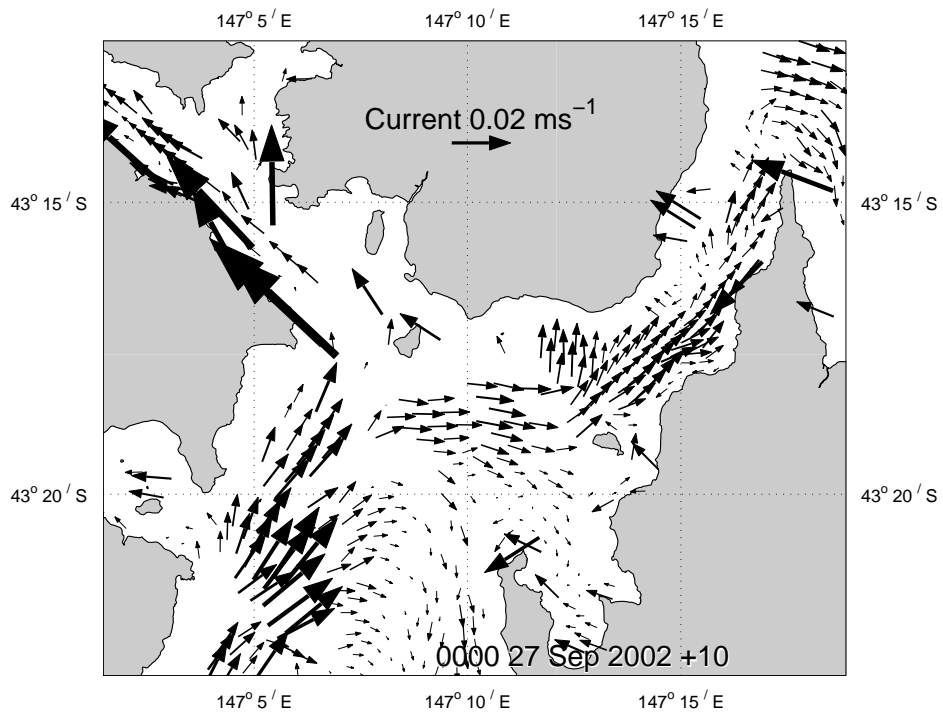


**Fig. 94. Bottom Flow near the Huon Mouth, Winter**

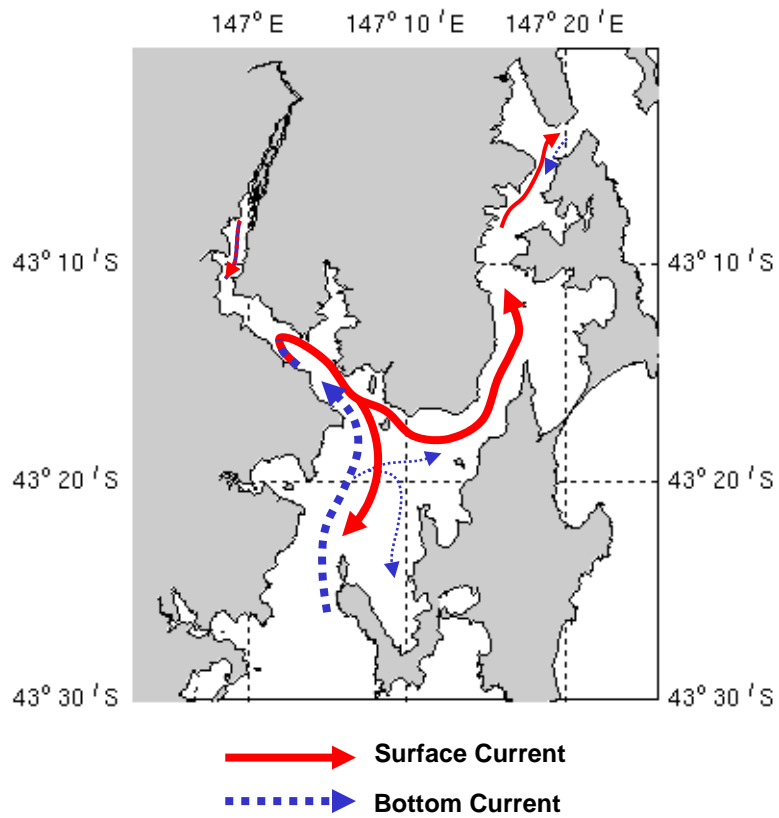


**Fig. 95. Residual Flow Schematic**

## 7.7 Point Source Releases

Point sources of tracers were continuously input into the water column at locations corresponding to a number of fish farm sites (Fig. 96 and Table 7) with unit loads (assumed to be  $1 \text{ gs}^{-1} \sim 31,500 \text{ kg/year}$ , giving output concentrations in units of  $\text{gm}^{-3}$ , or  $\text{mgL}^{-1}$ ) for the 12 month simulation period of 2002. Tracers were released over a depth range of 0 m to the shallower of 14 m depth (assumed to be the maximum depth of a farm cage) or the bottom. Surface tracer concentrations were output at 2 hour intervals and post-processed to compute the 5th, 50th (median) and 95th percentile distributions for the whole simulation, providing a statistical description of the distributions resulting from tracer transport over this period. Note that the response of the tracers to the interaction of the point source input with the system dynamics is linear, so that if the load were increased by some arbitrary factor then the corresponding concentrations can be scaled accordingly.

Results are displayed as Fig. 97 to 104. Results are interpreted thus: given that a continuous unit load is input at the Northwest farm site and its distribution throughout the domain allowed to reach quasi-steady state, at any given location in the domain one would expect to find the concentrations less than those shown in Fig. 97 (a) for 5% of the time, less than those in Fig. 97 (b) for 50% of the time and less than those in Fig. 97 (c) for 95% of the time. Note that the concentration scales in the Figures for the three percentiles differ from one another.

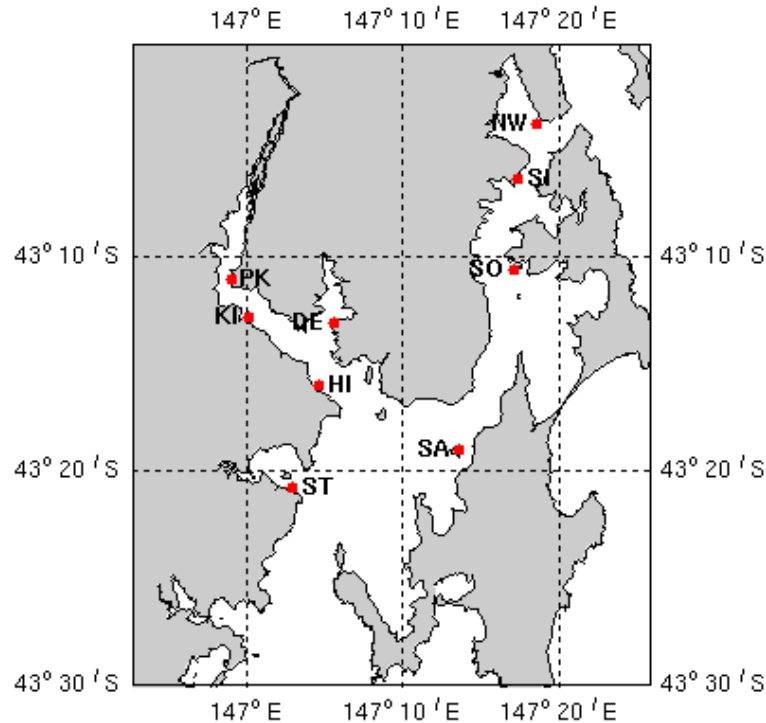


**Fig. 96. Fish Farm Locations**

**Table 7. Fish Farm Locations**

Name	Abbreviation	Latitude South	Longitude East	Release Depth (m)
NorthWest	NW	43.063020	147.309240	0 to 14
Simmonds	SI	43.105797	147.289587	0 to 10.9
Soldiers	SO	43.177225	147.285018	0 to 11.6
Satellite	SA	43.316706	147.226917	0 to 11.1
Stringers	ST	43.345850	147.049574	0 to 14
Hideaway	HI	43.267059	147.077482	0 to 14
Deep	DE	43.217831	147.093111	0 to 13.2
Killala	KI	43.213835	147.002434	0 to 9.6
Brabazon Park	PK	43.184632	146.983638	0 to 11

Release sites in the northern portion of the domain result in tracer distributions that are confined to the northern channel. Distributions from the Northwest release are mainly confined to the head of North West Bay, with median concentration of  $\sim 0.0005$  found down to Barnes Bay. Once the release moves outside of North West Bay into the channel, concentrations in the channel increase and relatively uniform distributions are observed in North West Bay. The concentrations near the Simmonds release mixing zone can reach  $\sim 0.003$ . Release at Soldiers again distributes tracer throughout the upper channel and North West Bay, although concentrations decrease slightly towards the head of North West Bay. Low concentrations are now encountered in Great Bay (median  $\sim 0.0004$ ).

Distributions resulting from release further south down the channel at Satellite exhibit a dramatic change. Tracer is now found throughout the channel, and a well defined mixing zone of several kilometers exists around the release point with median concentrations of  $\sim 0.001$ . Low concentrations are now observed in the Huon Estuary. The Stringers release site also results in tracers distributions throughout the domain, with relatively uniform distributions found outside the mixing zone region of Port Esperance. Again tracer is found within the Huon Estuary, having median concentrations of  $\sim 0.0005$  and maximums of  $\sim 0.001$ . The Hideaway release again shows relatively uniform distributions throughout the domain outside a reasonably well defined mixing zone. Median concentration in the northern channel due to release at this site are  $\sim 0.0007$ , surprisingly slightly more than median concentrations in the upper Huon of  $\sim 0.0005$ . This general distribution is repeated for the Deep release site, with the mixing zone confined to Port Cygnet and

quite uniform concentrations elsewhere, having a channel median of  $\sim 0.0007$  and 95 percentile of 0.001.

The Killala release site results in distributions that are larger in the Huon Estuary than the D'Entrecasteaux Channel. Median concentrations are 0.001 in the upper and lower Huon while channel concentrations are  $\sim 0.0007$ . Elevated concentrations are observed in the channel near the Huon mouth. Finally release at Brabazon Park results in highest concentrations in the upper Huon, which decrease down-river and into the channel. Median concentrations are  $\sim 0.006$  at Huonville and  $\sim 0.001$  throughout the channel.

The tracer distributions therefore exhibit significant variability depending on the release location. Generally those sites in the northern channel result in distributions confined to the northern D'Entrecasteaux. Releases in the channel below Gordon and in the lower Huon result in relatively uniform concentrations throughout the domain outside a well defined mixing zone having high concentration. For release sites further up the Huon Estuary, the largest concentrations are confined to the upper Huon and uniform concentrations of lower magnitude are found throughout the rest of the domain. Surprisingly, median concentrations in North West Bay resulting from the furthest upstream release site in the Huon Estuary, Brabazon Park, were the largest of all release sites in the lower channel and Huon Estuary, and comparable to that of the Simmonds release site. This is probably because the Brabazon Park site bears the full brunt of any Huon flow, while since the river favours the northern bank the Killala site is not exposed to as much advection and can establish a local mixing zone.

(a) 5 Percentile

(b) Median

(c) 95 Percentile

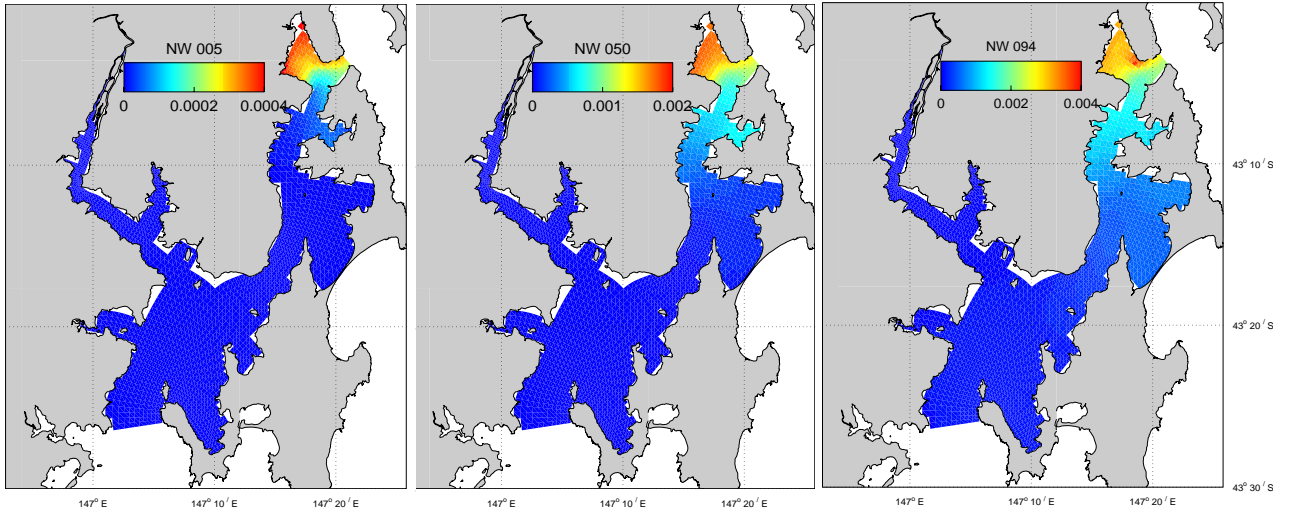


**Fig. 97. Norwest Surface Percentile Distributions**

(a) 5 Percentile

(b) Median

(c) 95 Percentile

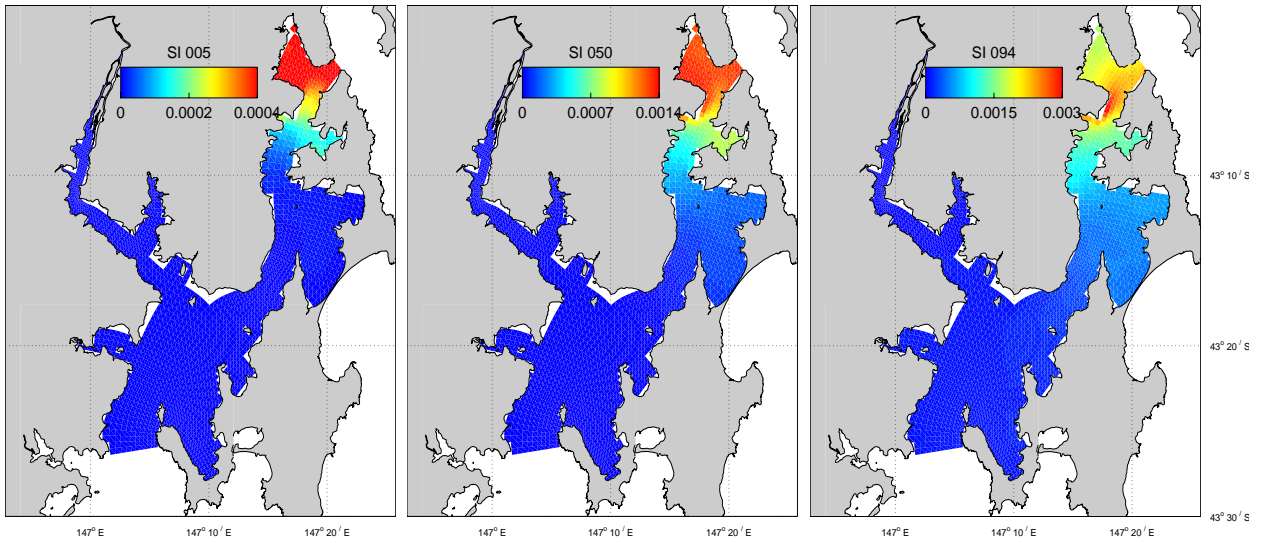


**Fig. 98. Simmonds Surface Percentile Distributions**

(a) 5 Percentile

(b) Median

(c) 95 Percentile

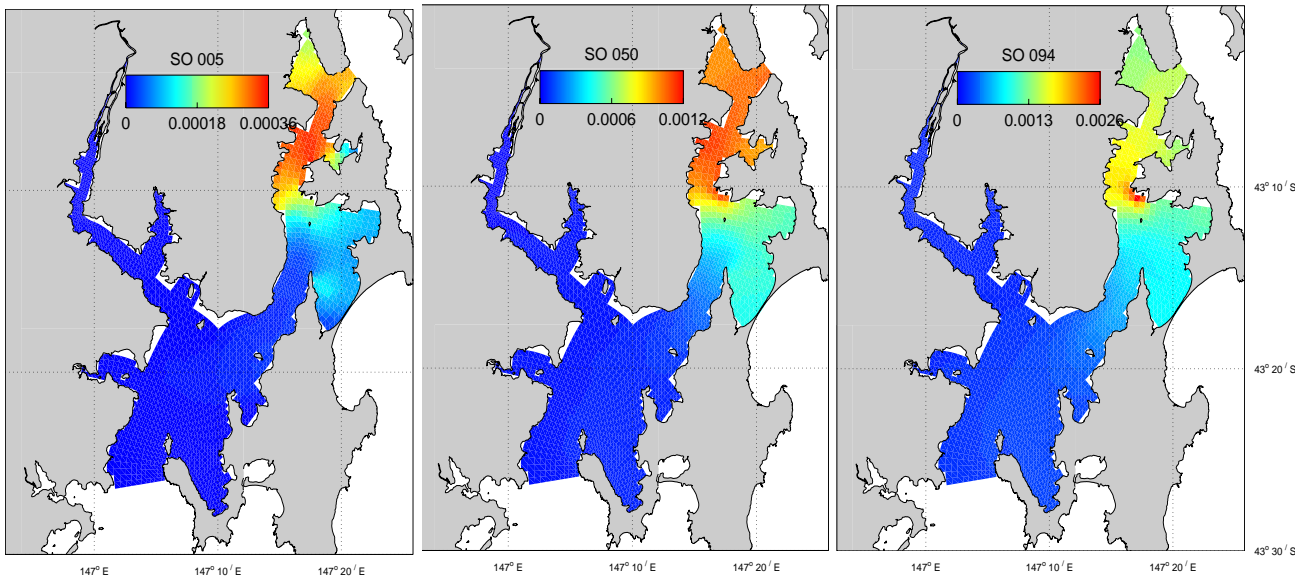


**Fig. 99. Soldiers Surface Percentile Distributions**

(a) 5 Percentile

(b) Median

(c) 95 Percentile

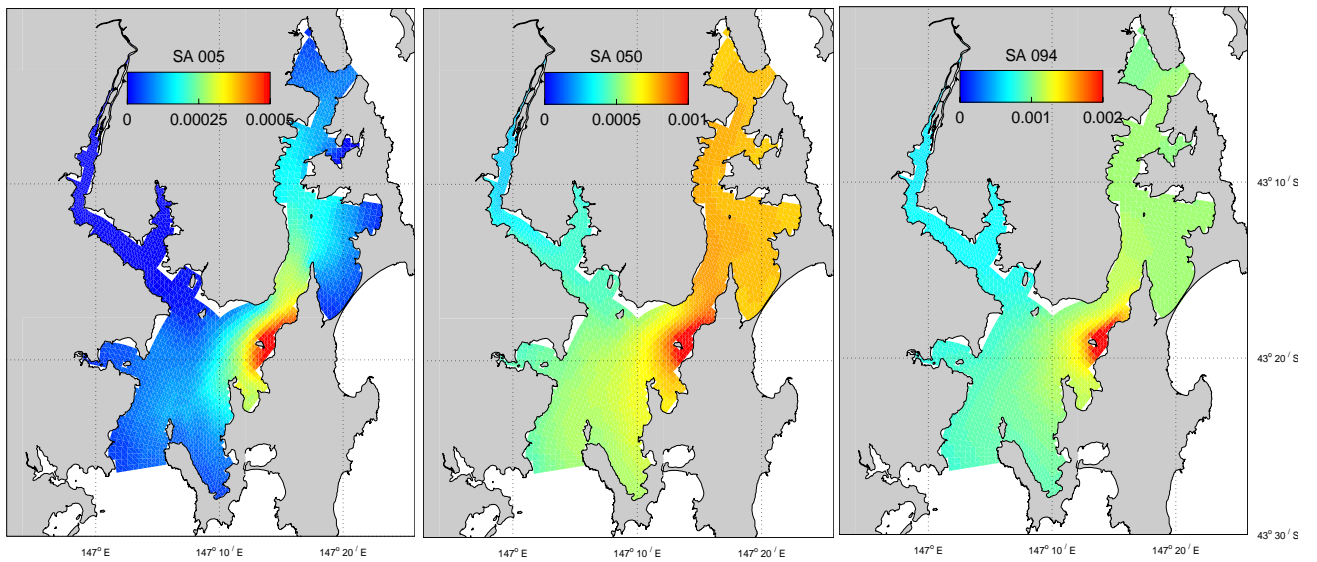


**Fig. 100. Satellite Surface Percentile Distributions**

(a) 5 Percentile

(b) Median

(c) 95 Percentile

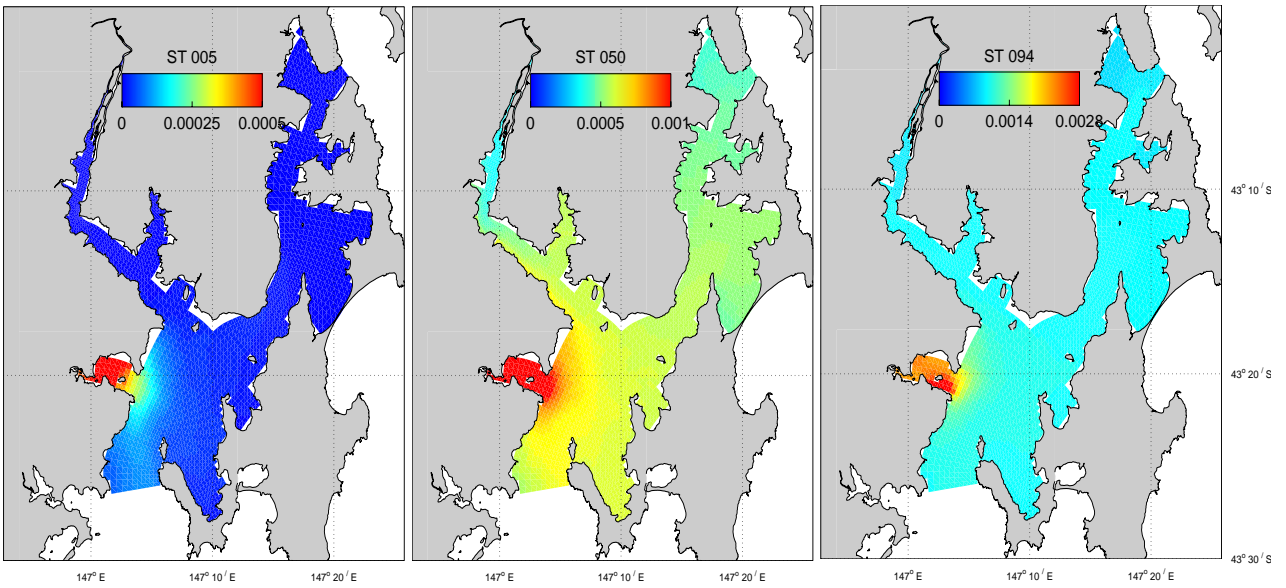


**Fig. 101. Stringers Surface Percentile Distributions**

(a) 5 Percentile

(b) Median

(c) 95 Percentile

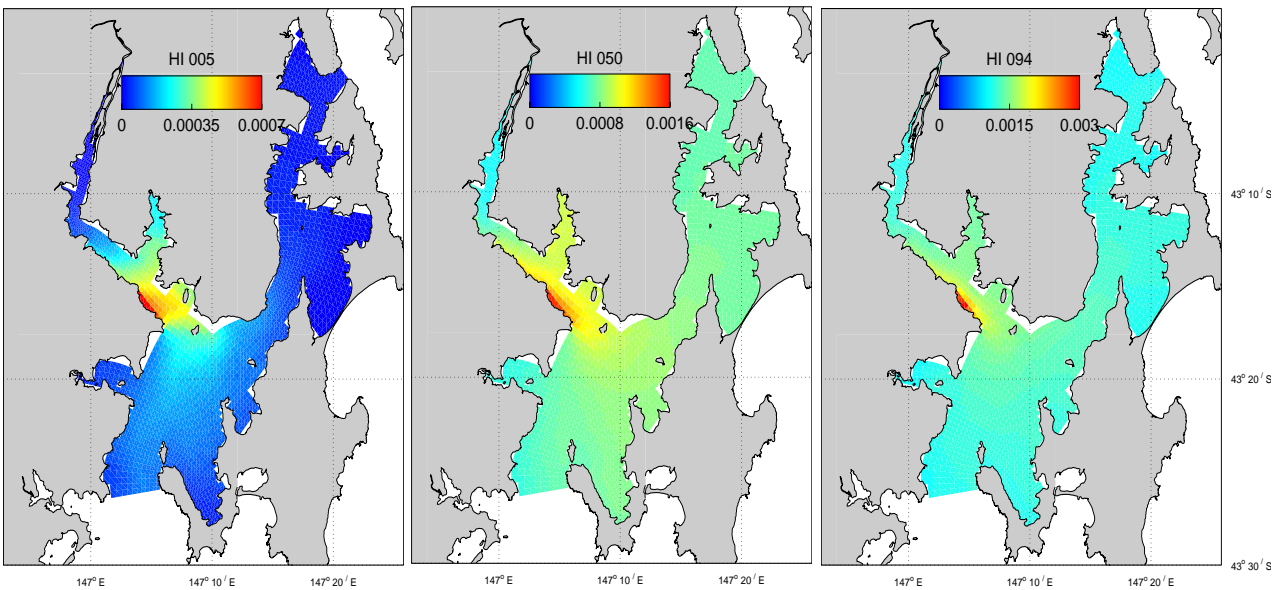


**Fig. 102. Hideaway Surface Percentile Distributions**

(a) 5 Percentile

(b) Median

(c) 95 Percentile

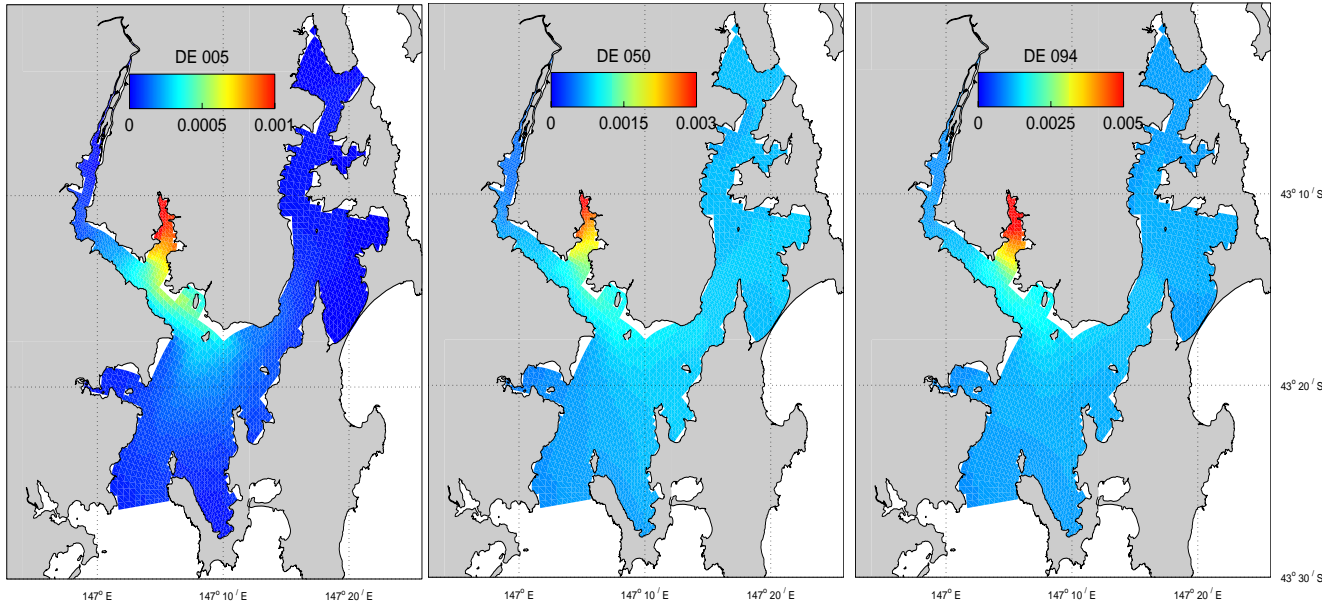


**Fig. 103. Deep Surface Percentile Distributions**

(a) 5 Percentile

(b) Median

(c) 95 Percentile

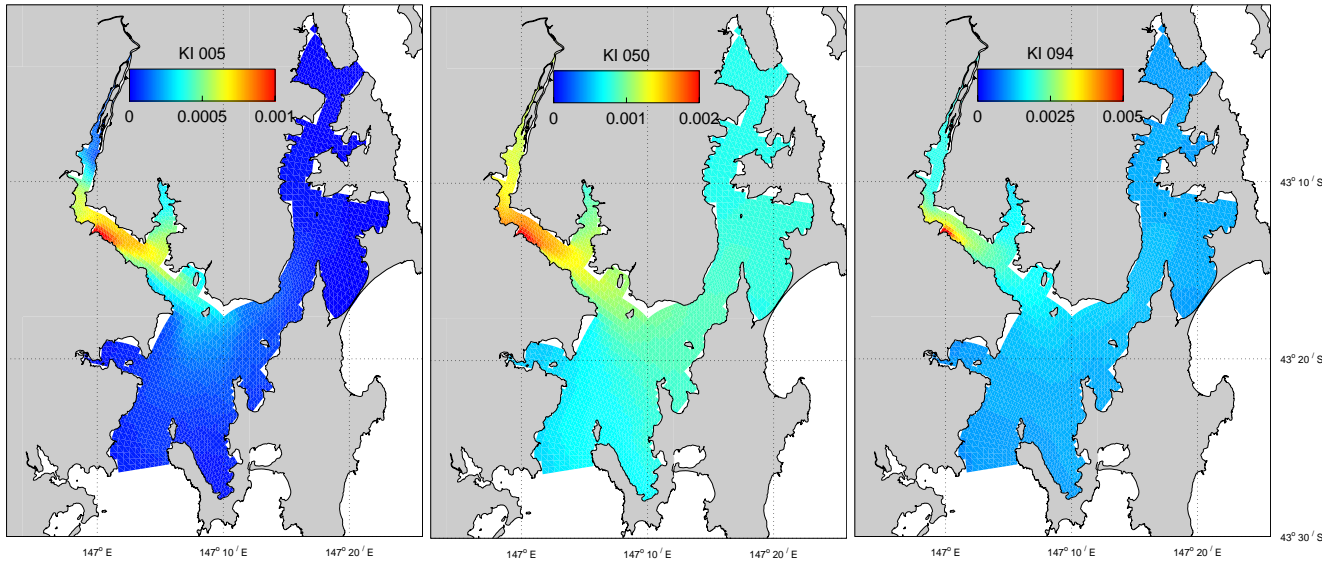
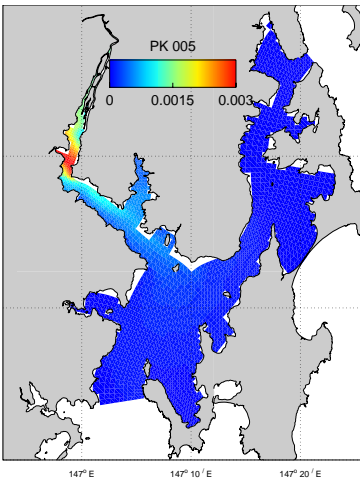
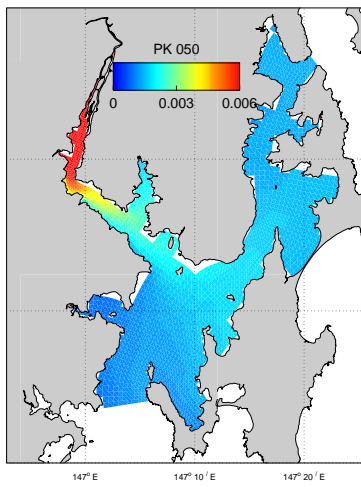


**Fig 104. Killarney Surface Percentile Distributions**

(a) 5 Percentile



(b) Median



(c) 95 Percentile

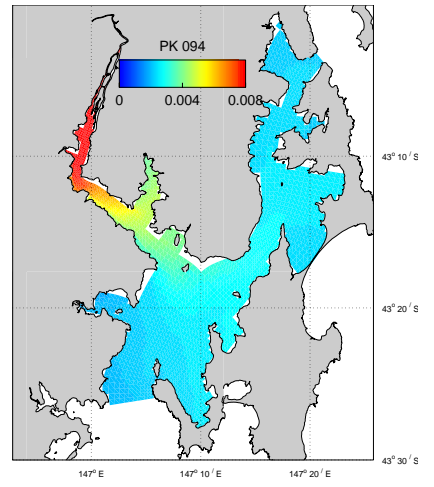


**Fig. 104b. Brabazon Park Surface Percentile Distributions**

## 7.8 Particle Tracking

The connectivity of the domain can be examined by observing the behaviour of neutrally buoyant particles released at the same locations as the point source releases in Section 7.6 and over the same depth range. The particles were released from random locations over the depth range at a rate of 2 particles/hour from an initial pool of 10,000 particles. These particles were subsequently advected with the circulation to provide insight into how various regions of the domain are connected. The particles are also subjected to random motion representing the effect of diffusion (i.e. sub-grid scale effects). Therefore, any two particles released from the same place at the same time are expected to undergo different trajectories due to this random motion. When a particle crosses the open boundaries at the northern and southern end of the model domain it is placed in the initial pool for subsequent re-release. The particle distributions after 6 months of simulation (corresponding to mid-winter) are displayed in Figs 105 to 113. This distribution is the projection of particles at all depths onto the surface. Particles are colour coded according to their age since being released over the range 0 – 20 days (i.e. blue particles are 0 days old, red particles are > 20 days old).

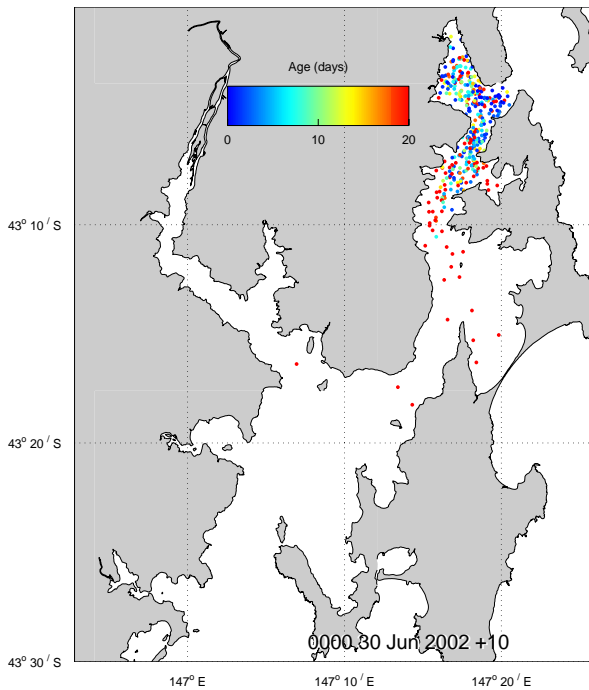


**Fig. 105. Northwest**

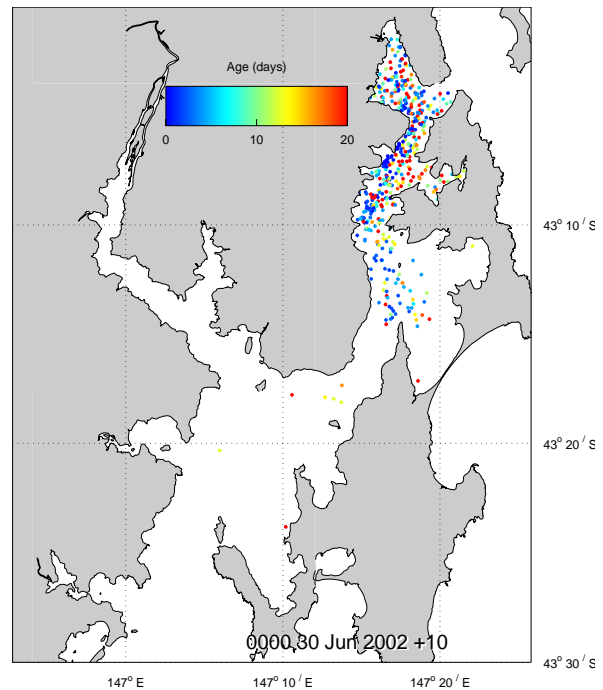


**Fig. 106. Simmonds**

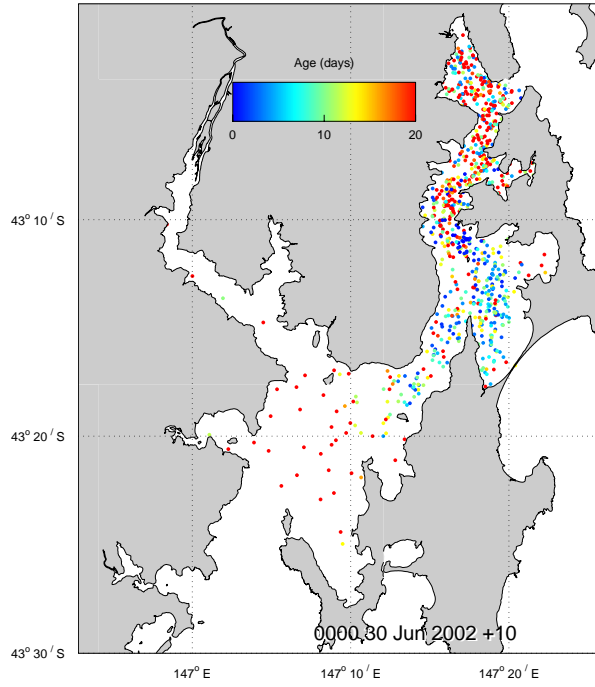


**Fig. 107. Soldiers**

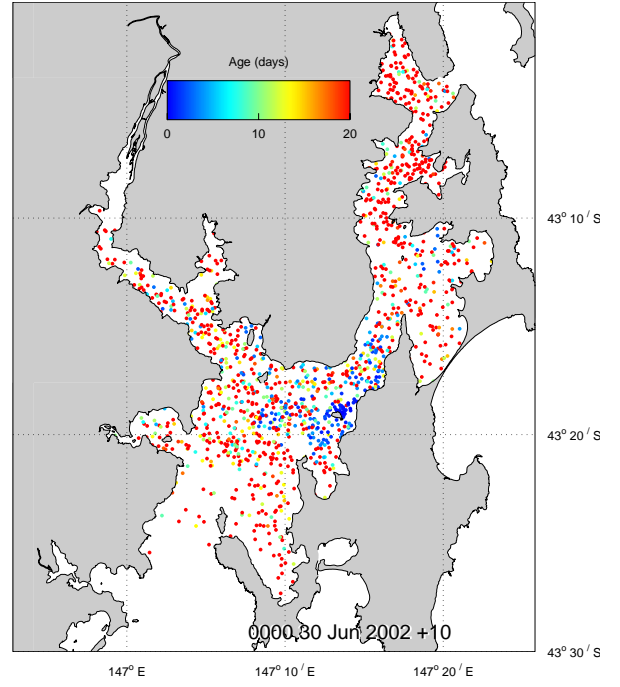


**Fig. 108. Satellite**

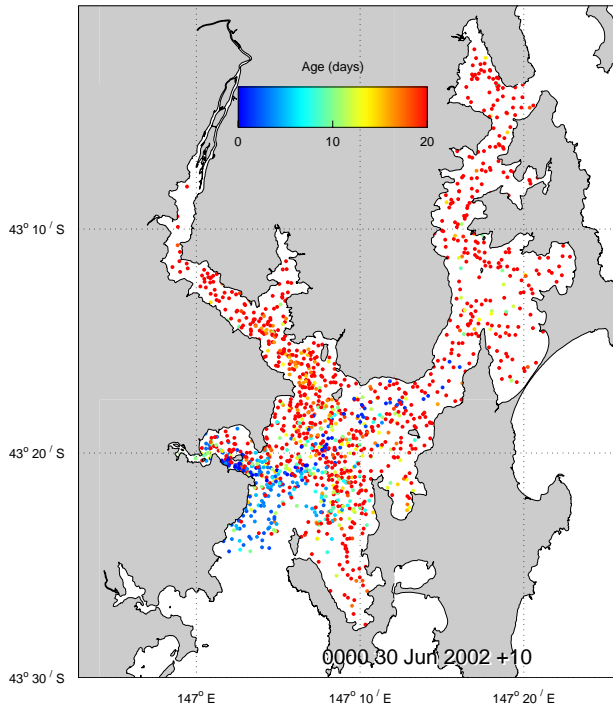


**Fig. 109. Stringers**

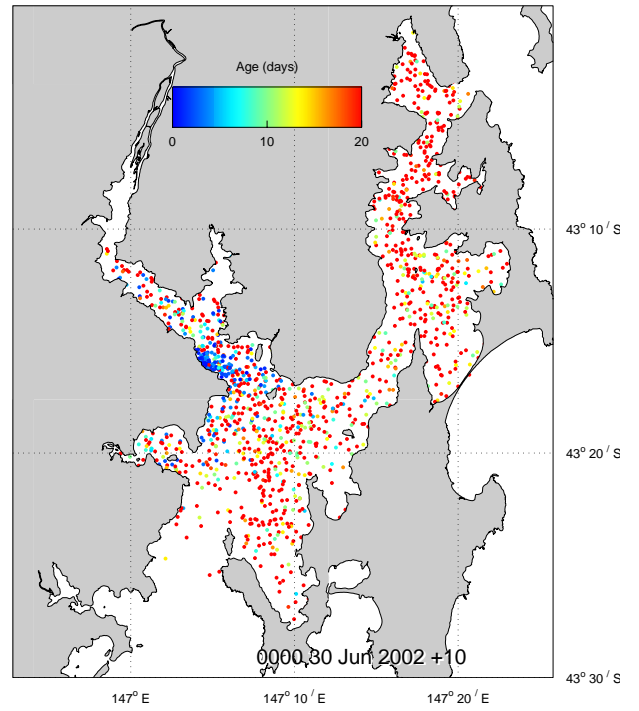


**Fig. 110. Hideaway**

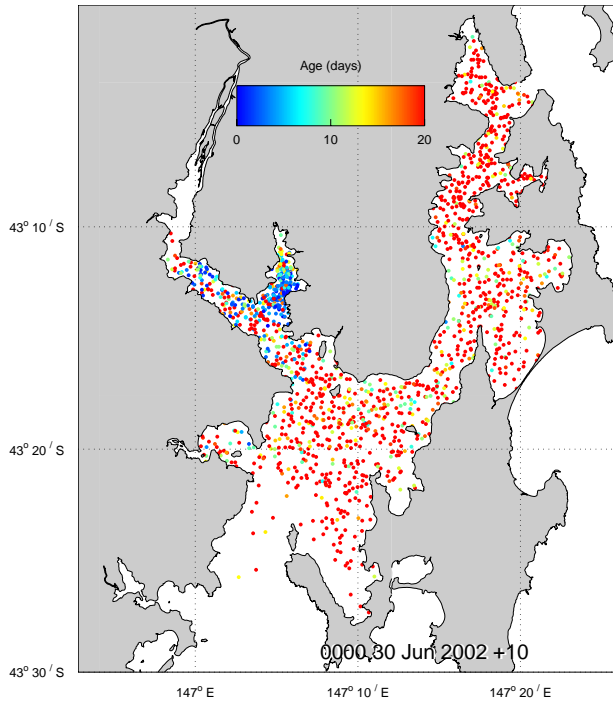


**Fig. 111. Deep**

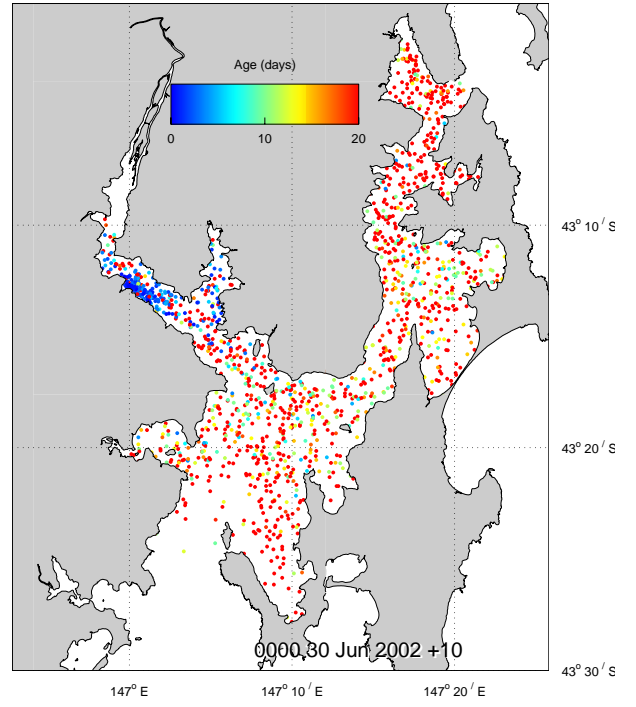


**Fig. 112. Killala**

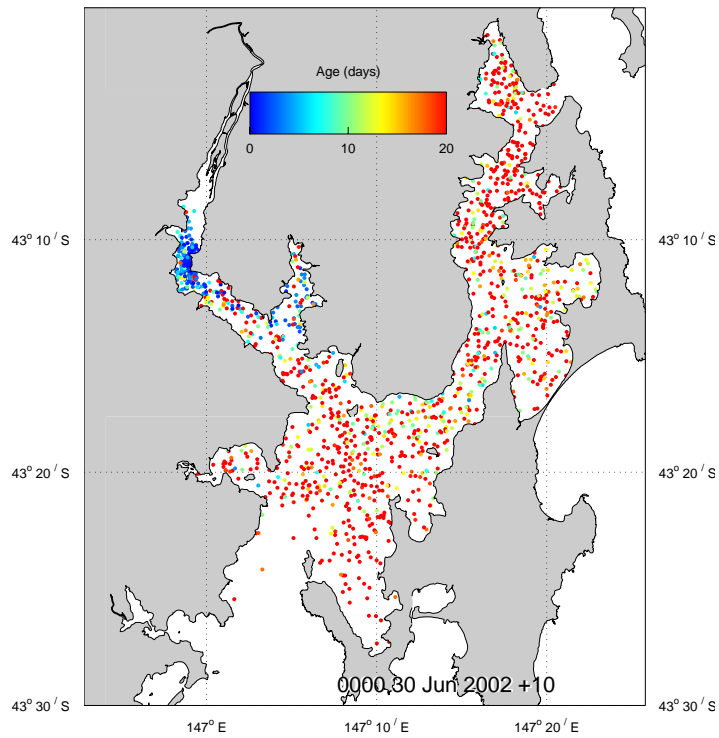


**Fig. 113. Brabazon Park**

These Figures show that particles released in the southern channel and Huon Estuary exhibit relatively uniform distribution throughout the whole domain whereas those released at sites in the northern channel result in distributions confined to the northern domain. Therefore the southern channel and Huon Estuary are well connected to the whole domain, whereas the northern channel has relatively poor connectivity with the southern channel. This is consistent with the residual flow analyses which suggest a net flow up-channel exiting through the northern boundary. In the long term particles are expected to follow trajectories corresponding to this mean flow. Also, it can be seen that many of the particles have ages greater than 20 days, suggesting the e-folding flushing time of the whole estuary estimated in Section 7.4 may actually be an underestimation of the time it takes neutrally buoyant particles to be transported out of the domain. Of particles released from all sites, there existed 47162 particles that were lost through the open boundaries, and the mean age of these particles was 26 days. Figs 111 - 113 also show that particles released in the Huon Estuary are capable of reaching the northern channel and North West Bay in around 10 days.

Due to the large number of particles in the domain, an animation of the particle trajectories best conveys the connectivity of the region, although observation of isolated particle trajectories does supply insight into the dynamics of the system. The trajectories of particles were traced during the flood and ebb of a spring tide during 17 – 20 May 2002 (Fig. 114) and displayed in Figs 115 and 116 respectively.

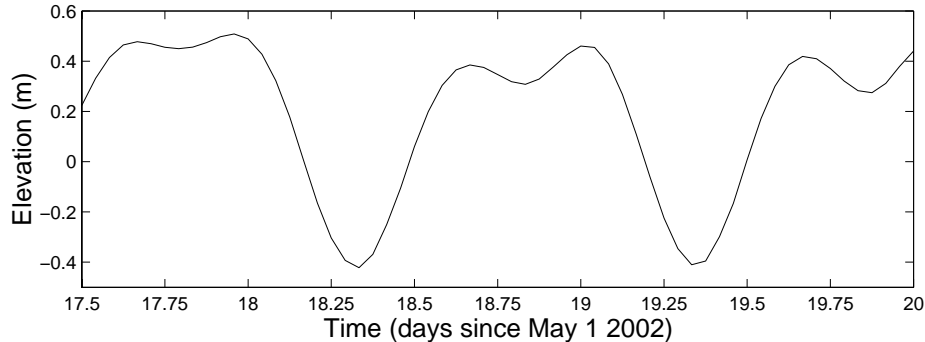


**Fig. 114. Spring tide during 17 – 20 May 2002**

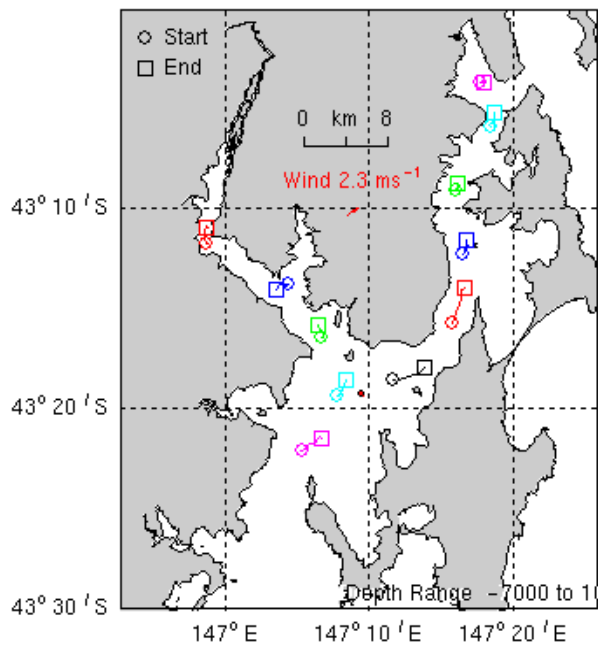


**Fig. 115. Flood Tide, 19 May 0800**

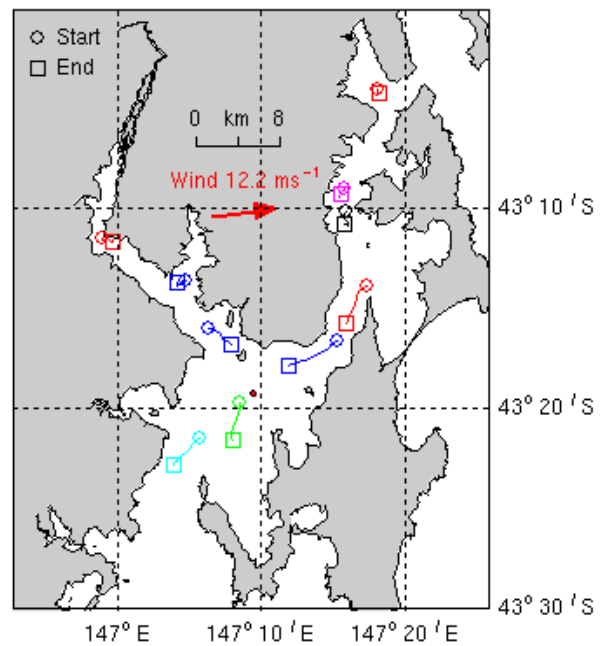


**Fig. 116. Ebb Tide, 18 May 0000**

The flood tide in this instance had a tidal range of 0.83 m and the ebb of 0.95 m. Low to moderate south-westerly winds of  $\sim 0.5 - 12 \text{ ms}^{-1}$  were in effect during this period. During the flood tide, particles are transported up-channel towards the north (and up-river in the Huon; north-west) and during the ebb transported down-channel towards the south (and down-river south-eastwards) as expected. Maximum tidal excursions are found mid-channel at the narrowest location near Gordon, where excursions are of the order of 4 km. Further south the excursion decreases and in the northern channel and Huon Estuary the excursions are less than 1 km.

A large flow event occurred on 15 August with a flow of close to  $1000 \text{ m}^3\text{s}^{-1}$  (day 227 Fig. 23) under the influence of moderate south-westerly winds ranging from  $\sim 5-10 \text{ ms}^{-1}$ . Tidal ranges were of the order 0.88 m. In this case the flood plume charged up-channel to as far as North West Bay (Fig. 117). Particle trajectories also reflect this up-channel motion (Fig. 118) where particles traced for 57 hours from 14 Aug 1200 to 17 Aug 2100 show displacement of greater than 24km, in some cases from near Cygnet to Barnes Bay (green trajectory).

Similar strength north-easterly winds occurred during a flood event centered on 15 June with a flow of  $\sim 700 \text{ m}^3\text{s}^{-1}$  (day 160 Fig. 23). These winds pushed the flood plume southwards into Great Taylor Bay and out of the southern boundary (Fig. 119). During this time the tide underwent a cycle with range 0.89 m. Corresponding trajectories for the 20 hour period from 0900 14 June to 0500 15 June are displayed in Fig. 120. Trajectories are oriented down-channel during this event with displacements up to  $\sim 16 \text{ km}$ . This

demonstrates the strong impact of north-easterly winds on the freshwater plume during flood events.

The up-channel direction for the freshwater plume transport is the preferred direction, since under the influence of cross-channel north-westerly winds the plume favours the up-channel direction (Fig. 121). Flow was  $\sim 550 \text{ m}^3\text{s}^{-1}$  with a tidal range of 0.64m. Particles were tracked for 38 hours from 30 Jun 0800 to 01 Jul 2200. The favoured up-channel motion is the result of Coriolis balancing the baroclinic pressure gradients, where the Coriolis force deflects the surface flow towards the left (i.e. up-channel) of the down-river pressure gradient.

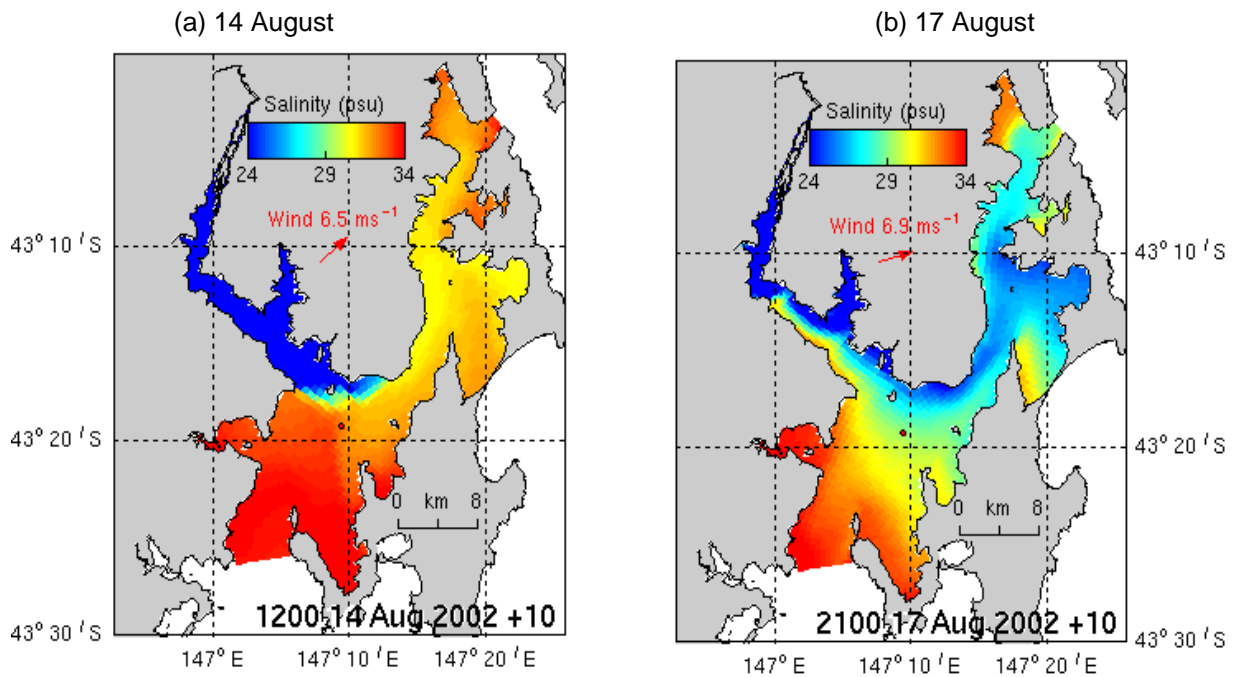


**Fig. 117: Surface salinity during 15 August flood event**

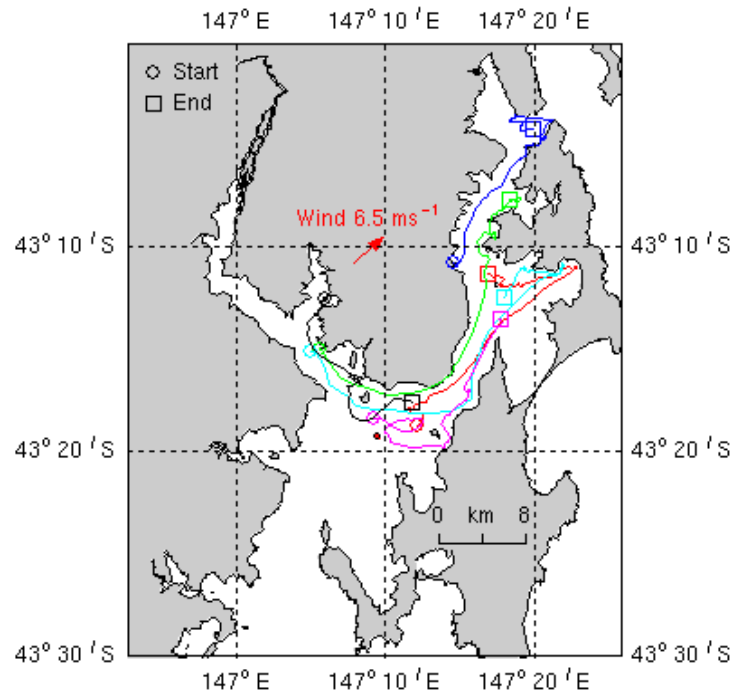


**Fig. 118. Trajectories during 15 August flood event**

(a) 14 June

(b) 15 June

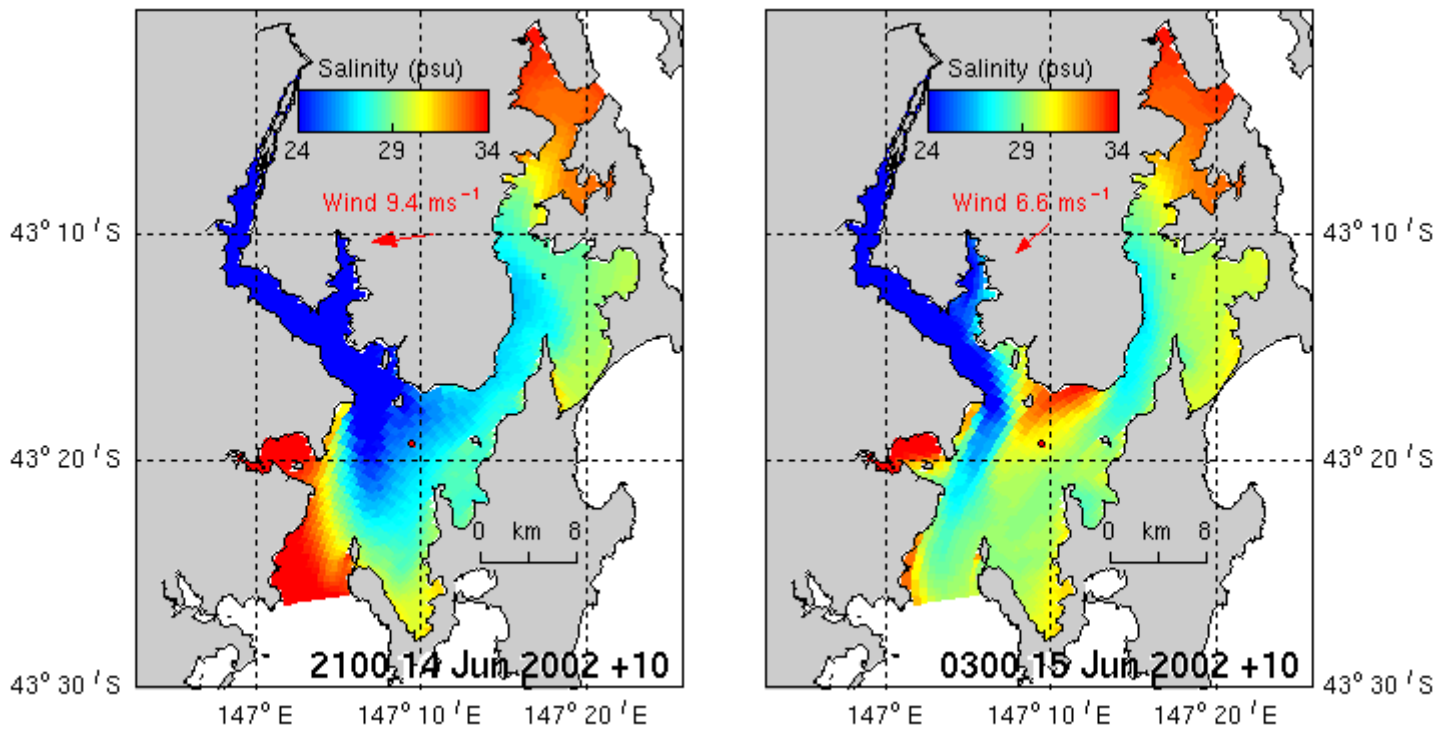


**Fig. 119. Surface salinity during 15 June flood event**

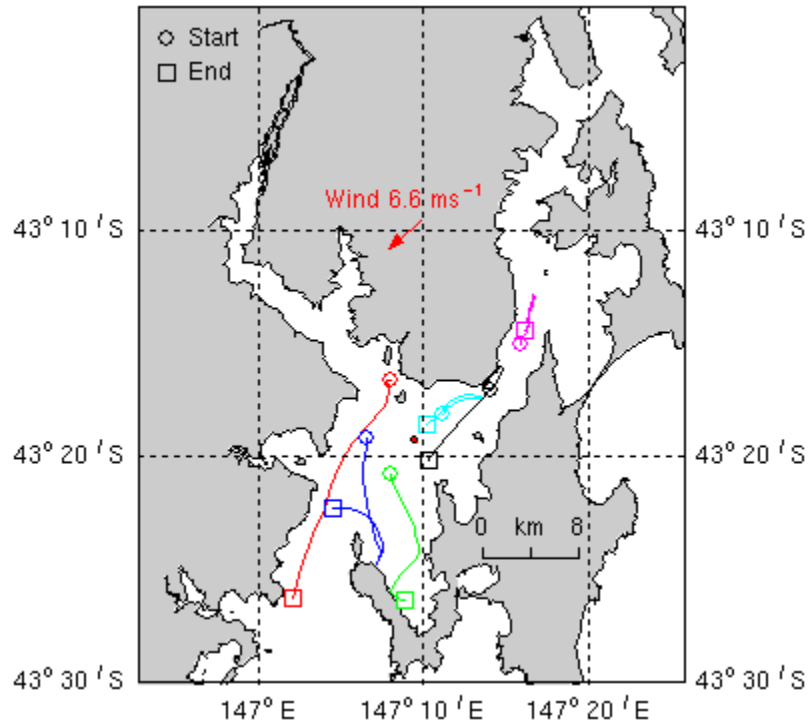


**Fig. 120. Trajectories during 15 June flood event**

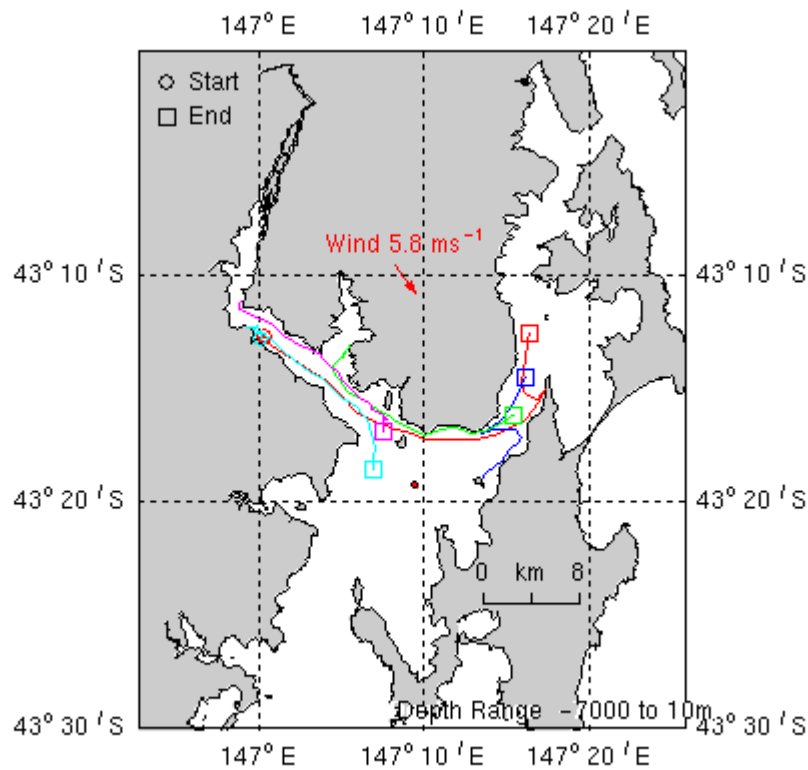


**Fig. 121. Trajectories during 1 July flood event**

## 7.9 Coarse Model

The model presented above proved unsuitable for coupling with ecology and sediment transport models since the high resolution of the model in conjunction with the large number of tracers required by the ecology and sediment models resulted in run-time ratios becoming unreasonably low. A model grid with reduced horizontal resolution was constructed to rectify this problem (coarse model). The coarse model grid is depicted in Fig. 122. Resolution ranged from ~350 m cross-river in the upper Huon to 1.3 km in the upper channel, lower Huon and near the southern boundary. This grid coupled to ecology and sediments resulted in acceptable run-time ratios of  $> 100:1$ . The calibration for this model is displayed in Fig. 123. It can be seen that the calibration is not as good as the high resolution model owing to the decrease in resolution, but is still nonetheless acceptable.

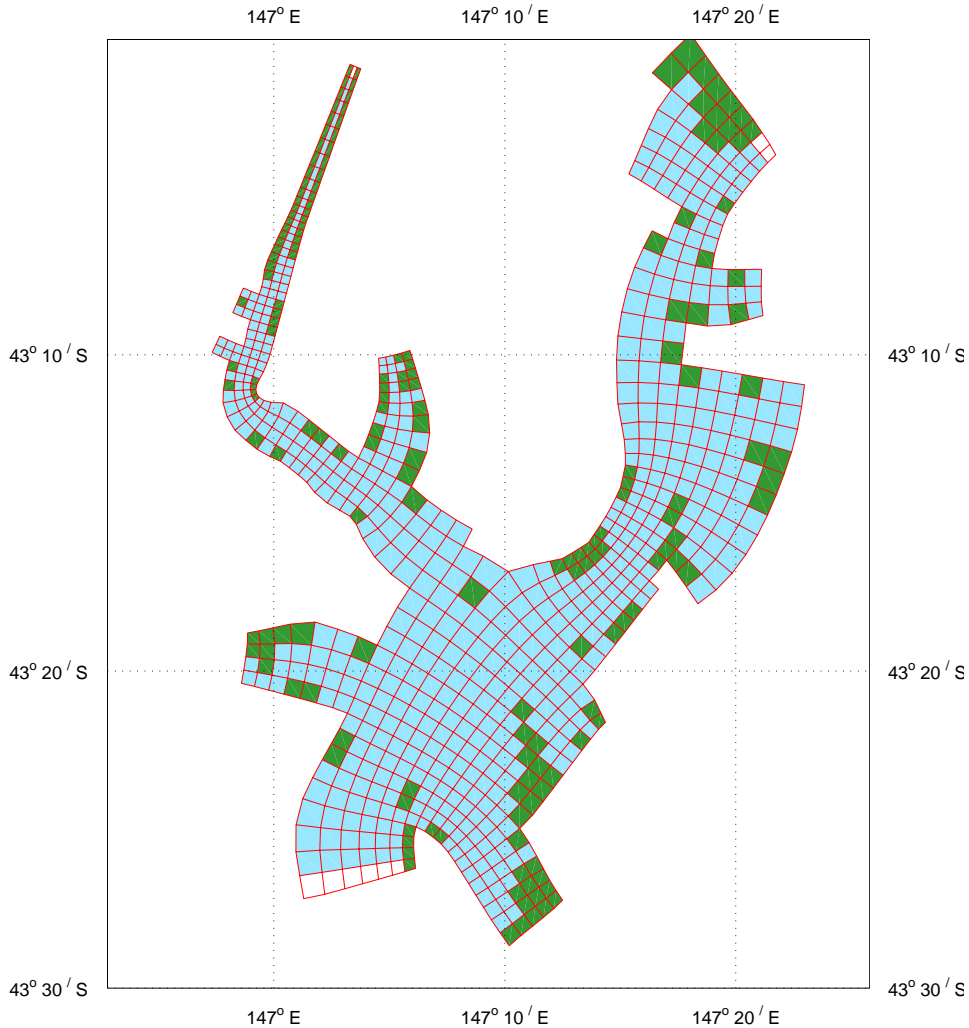


**Fig. 122. Coarse Model Domain**

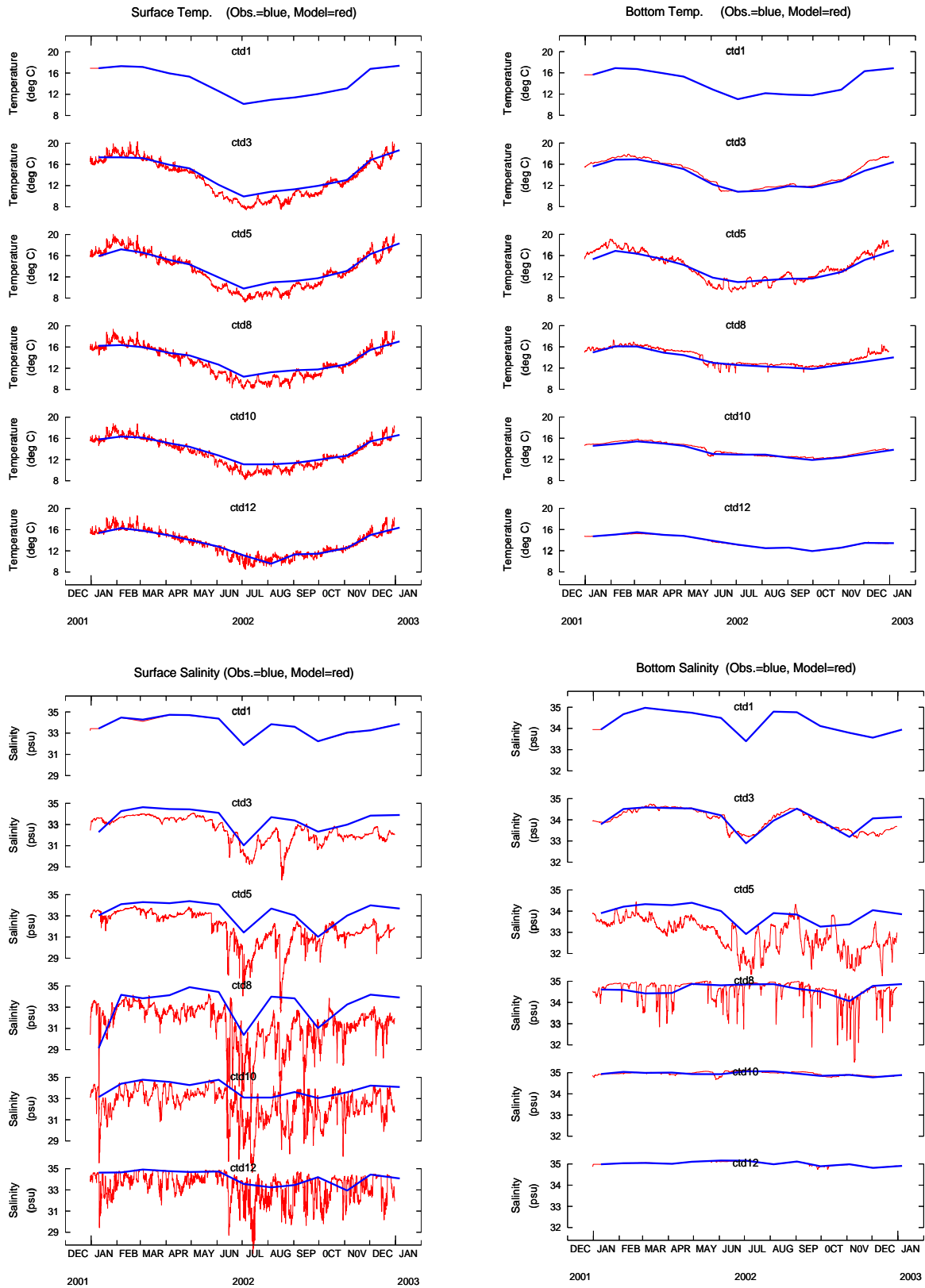


**Fig. 123. Coarse Model Calibration**

## 8 Conclusions

A 3D primitive equation model was applied to Huon Estuary/D'Entrecasteaux to examine the hydrodynamics of the region. Using a nesting process the region was represented with high resolution while incorporating forcing due to wind stress, tides, low frequency sea level oscillations and pressure gradients due to temperature and salinity distributions. Major forcing consists of river flow, which may be as large as  $1000 \text{ m}^3\text{s}^{-1}$ , wind which has an annual average speed of speed of  $4.3 \text{ ms}^{-1}$  from the south and tide which has a range of  $\sim 1\text{m}$  during the spring tide. The full year of 2002 was simulated and calibrated to data collected within the Broad Scale Monitoring Program.

Several physical processes proved important in obtaining an acceptable calibration. Surface heat fluxes play a crucial role in regulating temperature in the region. The model proved sensitive to the type of bulk formulation used for surface sensible and latent heat fluxes, and to a lesser extent the depth to which short wave radiation is allowed to penetrate. Differential heating is apparent in the side bays, both in measured data and in the model and this may contribute towards heating of the main channel.

Non-linear effects were important near the northern boundary of the domain. This prompted the construction of an intermediate scale model which better resolved velocity in this region and was suitable for nesting the local model in using boundary velocity forcing. The local model also proved sensitive to the background vertical diffusion coefficient, type of mixing scheme used and magnitude of the imposed Huon River flow.

Data collected within the Broad Scale Monitoring Program revealed that a temperature gradient (up to  $1^\circ\text{C}$ ) exists along the D'Entrecasteaux Channel during summer and autumn, with the northern end associated with higher temperature. The deeper waters at the southern end have the lowest temperature in the channel, presumably due to the sub-thermocline oceanic influence. Towards autumn the vertical temperature gradient at the southern end is less pronounced, as surface cooling decreases surface temperature heading into winter. In winter bottom waters become warmer than surface waters, but still several degrees cooler than the summer bottom temperature. This bottom temperature increase in winter is also observed at the northern end of the channel. Salinity is lower in the mid-channel region and attains the highest values in bottom waters at the ends of the channel throughout the year, thus density compensating the temperature distribution. Thin fresh water layers can be observed mid-channel during times of high Huon River flow.

The model results confirm these trends and validate that the Huon Estuary behaves as a salt wedge estuary with marine flow in bottom waters directed upstream in the estuary and a fresh water surface flow heading downstream. The head of the salt wedge is located near Huonville under low flow and is pushed downstream under high flow conditions. The downstream surface flow generally favours the northern bank of the river, heading northwards up-channel upon entering the D'Entrecasteaux. Under high flow conditions fresher water may be found as far north as North West Bay, and may be advected north as much as 24km in just over 2 days.

On diurnal timescales the tidal flow dominates the region, with flow directed up-river and up-channel during the flood tide, and vice versa during the ebb. Strongest currents exist in the narrowest point in the channel near Gordon, where they approach  $0.5 \text{ ms}^{-1}$ . The tide undergoes a neap-spring cycle of the order of 14 days, with maximum tidal ranges approaching 1m. The tide is predominantly of diurnal (daily) mixed character with a form factor  $F \sim 1.5$ . Maximum tidal excursions are of the order of 4km mid-channel. In the southern channel the excursion decreases and in the northern channel and Huon Estuary the excursions are less than 1km. The momentum balance of surface flow on these timescales is dominated by the tide and wind, opposed by the Coriolis force. In bottom water vertical and lateral friction becomes important.

The mean seasonal flow for the D'Entrecasteaux–Huon Estuary system consists of bottom water entering the region at the southern end of the channel and moving up into the Huon Estuary in the salt wedge, favouring the southern bank. Entrainment occurs from the salt wedge into the downstream freshwater flow, the majority of which then turns north upon entering the channel and exits into Storm Bay at the northern end of the channel. A smaller proportion of Huon flow exits the channel through the southern boundary. The momentum balance indicates that the mean surface flow in the Huon Estuary consists of a balance between density forcing and Coriolis, with wind contributing to down-river flow. In the northern channel density driven flow combines with rotation forces to produce seasonal up-channel residual flow. Cross channel forces balance in this area, with Coriolis opposing wind driven flow with some contribution of density effects to Coriolis. The southern channel exhibits both along and cross-channel mean flow. Coriolis forcing opposes density forces in the along-channel direction while the wind driven flow opposes density driven flow in the cross-channel direction. Coriolis forcing is directed up-channel throughout the channel, whereas density effects are directed up-channel in the northern channel and down-channel in the southern channel. Horizontal friction becomes more important in bottom waters.

The calculation of flushing times can be subjective depending on the method used to compute the flushing. Using an e-folding rate based on depletion of total mass in a region the flushing times varied from around 3 days for the lower Huon Estuary under high flow conditions to ~20 days for the whole domain in winter. A flushing estimate for the whole domain based on the average time for neutrally buoyant particles to exit the domain was computed as ~26 days.

Distributions of passive tracers resulting from release in the top 14m of the water column at locations corresponding to selected farm sites showed significant variability with release location. Generally those sites in the northern channel result in distributions confined to the northern D'Entrecasteaux. Release sites in the channel below Gordon and in the lower Huon Estuary resulted in relatively uniform concentrations throughout the domain outside a well defined mixing zone of high concentration. For release sites further up the Huon the largest concentrations are confined to the upper Huon and uniform concentrations of lower magnitude are found throughout the rest of the domain. These general distributions were also observed in results obtained via particle tracking of

neutrally buoyant particles released from the respective farm sites. The southern channel and Huon Estuary can be characterized as well connected to the whole domain, whereas the northern channel has relatively poor connectivity with the southern channel.

Particle tracking results also confirmed the diurnal dominance of tidal forcing, with particles exhibiting up-channel and up-river movement on the flood tide, and down-channel / river on the ebb. During flood events the favoured trajectory out of the Huon was up-channel. The freshwater plume also favoured the northern bank of the Huon due to the influence of Coriolis forces. The location of the freshwater plume was, however, sensitive to wind direction, with north-easterly winds pushing the freshwater plume southwards.

The hydrodynamic model has provided useful insight into the physics of the D'Entrecasteaux and Huon Estuary system. Due to computational pressures the model was unsuitable for coupling to ecological models, and a coarser resolution model was developed to fulfill this role.

## 9 References

- Blumberg, A.F., Kantha, L.H. (1985) Open boundary condition for circulation models, *J. Hydraulic Eng.*, 111, 237-255.
- Burchard, H., Peterson, K.O., Rippeth, T.P. (1998) Comparing the performance of the Mellor Yamada and the k- $\epsilon$  turbulence models. *J. Geophys. Res.*, 103, 10,543-10,554.
- Burchard, H., Bolding, K., Villarreal, M.R. (1999) GOTM, a general ocean turbulence model. Theory implementation and test cases. Technical Report EUR 18745EN, European Commission, 103 pp.
- Cartwright, D.E., Ray, R.D. (1990) Oceanic tides from Geosat altimetry. *J. Geophys. Res.*, 95 C3, 3069-3090.
- Kondo, J. (1975) Air-sea bulk transfer coefficients in diabatic conditions. *Boundary-Layer Meteorology*, 9, 91-112.
- Large, W.G., Pond, S. (1981) Open ocean momentum flux measurements in moderate to strong winds, *J. Phys. Oceanogr.*, 11, 324-336.
- Leonard, B.P. (1979) A stable and accurate convective modelling procedure based on quadratic upstream interpolation. *Comp. Meth. Appl. Mech. Eng.*, 19, 59-98.
- Leonard, B.P. (1991) The ULTIMATE conservative difference scheme applied to unsteady one-dimensional advection. *Comp. Meth. Appl. Mech. Eng.*, 19, 17-74.
- Marchesiello, P., McWilliams, J.C., Shchepetkin, A. (2001) Open boundary conditions for long term integration of regional oceanic models. *Ocean Modelling*, 3, 1-20.
- Mellor, G.L., Yamada, T. (1982) development of a turbulence closure model for geophysical fluid problems. *Rev. Geophys.*, 20, 851-875.
- Miller, M.J., Thorpe, A.J. (1981) Radiation conditions for the lateral boundaries of limited-area numerical models. *Q. J. R. Meteorol. Soc.*, 107, 615-628.

- Ridgway, K.R., Dunn, J.R., Wilkin, J.L. (2002) Ocean interpolation by four-dimensional least squares -Application to the waters around Australia, *J. Atmos. Ocean. Tech.*, 19, 1357-1375.
- Walker, S.J., Waring, J.R., (1998) A multiple grid, 3-dimensional, non-linear, variable-density hydrodynamic model with curvilinear horizontal coordinates and level ( $z$ ) vertical coordinates, CSIRO Marine Research, Report OMR-118/120.
- Zillman, J.W. (1972) A study of some aspects of the radiation and heat budgets of the southern hemisphere oceans. Bureau of Meteorology, Meteorological Study No. 26, Australian Govt. Pub. Service, Canberra.